BAUHAUS-UNIVERSITÄT WEIMAR

Nonlinear Numerical Modelling of Cable Elements in Bridges for Dynamic Analysis

Faculty of Civil Engineering
Institute of Structural Engineering

A thesis submitted in partial fulfillment for the
degree of Master of Science

by

Abdulmagid Sedig Khalafallah Bendalla

September 2019

Bauhaus-Universität Weimar
Fakultät Bauingenieurwesen
Institut für Konstruktiven Ingenieurbau
Professur Modellierung und Simulation - Konstruktion

Masterarbeit

Reg.-Nr.:	NHRE/2019/28
Bearbeiter:	Bendalla, Abdulmagid Sedig Khalafallah Matr.-Nr.: 118194
Thema:	"Nonlinear numerical modelling of cable elements in bridges for dynamic analysis"
Betreuer:	Prof. Dr. G. Morgenthal — Erstprüfer Dr. T. Abbas — Zweitprüfer
Ausgabetermin:	22. Mai 2019
Abgabetermin:	22. September 2019
Pflichtkonsultation:	nach Vereinbarung mit dem Betreuer

Weimar, 22. Mai 2019

Prof. Dr. G. Morgenthal
Vorsitzender des Prüfungsausschusses

Objectives

Cables are used as tension elements in various structures. In bridge engineering cables are applied as external post-tensioning tendons, suspension cables, hangers and as stay cables. More recently, extradosed bridges are used as cable-supported hybrid systems between beam and cable-stayed bridges. Different cable systems exist, most importantly locked-coil, parallel wire and multi-strand systems. These cables are anchored in different ways and some can be deviated at saddle-type devices.

Vibrations may lead to critical problems in the application of cables. Further, cable vibrations may be used to identify the tension force through linearized force-frequency relationships. The vibration behaviour of a tensioned cable will be dependent upon many different mechanical characteristics, and this thesis shall develop advanced numerical modelling techniques to accurately represent several of these. Firstly, the mechanical behaviour at the anchorage and deviation devices shall be modelled in a representative way. Secondly, the bending-stiffness effect of the different cable-systems shall be modelled in a way which is able to account for the interaction between different components of the cable cross section.

Main Tasks

The work shall be structured as follows.

(1) Literature survey of cable systems in bridges, cable types and vibration behaviour of cables.
(2) Literature survey of modelling techniques for the mechanical behaviour of cable elements, i.e. for static and dynamic behaviour.
(3) Discussion of the nonlinear effects in the static and dynamic cable behaviour and approaches to related numerical modelling.
(4) Development and implementation of parametrised numerical (FE) models for cable elements accounting for the interaction of wire and/or strand elements in cable cross sections. The models shall be implemented, tested and validated against theoretical, analytical and/or other numerical models, such as found in the literature.
(5) Development and implementation of parametrised numerical (FE) models for cable elements accounting for the geometrical and mechanical characteristics at anchorage and saddle regions, specifically (a) the deviation through transverse pressure along a tension-force-dependent length along the saddle, (b) stick/slip behaviour according to friction behaviour and (c) fixity in wedges.
(6) The above mentioned models may be refined local models not to be used in global models of the entire cable (system). It should be discussed/tested how the behaviour of the refined models can be represented by simplified models in the global model, specifically through (a) an effective bending stiffness and (b) spring elements e.g. representing an effective degree of fixity at the anchorage. The effect on the global vibration characteristics of the cable should be shown, alongside the ability of the parametrised model to account for different model properties (e.g. saddle radius). Suitable parametric studies should be performed.

The results of the thesis shall be visualized in a comprehensive manner in figures, tables and diagrams. All results (software code, input files and scripts) shall be comprehensively included in the thesis and its appendices. A softcopy (DVD) shall be included. A poster shall be prepared summarizing the thesis.

Declaration of Authorship

I, Abdulmagid Bendalla, declare that this thesis titled, 'Nonlinear Numerical Modelling of Extradosed Bridge Cable Elements' and the work presented in it are my own. I confirm that:

- This work was done wholly or mainly while in candidature for a research degree at this University.
- Where any part of this thesis has previously been submitted for a degree or any other qualification at this University or any other institution, this has been clearly stated.
- Where I have consulted the published work of others, this is always clearly attributed.
- Where I have quoted from the work of others, the source is always given. With the exception of such quotations, this thesis is entirely my own work.
- I have acknowledged all main sources of help.

Signed: 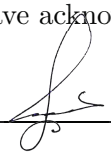

Date: 10.09.2019

Acknowledgements

Throughout the writing of this thesis I have received a great deal of support and assistance.

I would first like to express my deep gratitude to my thesis supervisor *Prof. Guido Morgenthal* for his patience, motivation, and immense knowledge. His office door was always open whenever I ran into trouble or had a question about my research or writing. He consistently allowed this document to be my own work, but steered me in the right direction whenever he thought I needed it.

I would also like to thank *Dr. Tajammal Abbas* for providing me with a SOFiSTiK script that helped in obtaining the outcome of this thesis.

Thanks goes also to my colleagues *Melad Haweyou*, *Mostafa Gad*, *Brit Engelen* and *Guy Chayeb* for their generous guidance and feedback. They were the key instrument in editing the lingual, and at few times, the technical content of this research.

BAUHAUS-UNIVERSITÄT WEIMAR

Abstract

Faculty of Civil Engineering
Institute of Structural Engineering

Master of Science

by Abdulmagid Sedig Khalafallah Bendalla

Identifying cable force with vibration-based methods has become widely used in engineering practice due to simplicity of application. The string taut theory provides a simple definition of the relationship between natural frequencies and the tension force of a cable. However, this theory assumes a perfectly flexible non-sagging cable pinned at its ends. These assumptions do not reflect all cases, especially when the cable is short, under low tension forces or the supports are partially flexible. Extradosed bridges, which are distinguished from cable-stayed bridges by their low pylon height, have shorter cables. Therefore the application of the conventional string taut theory to identify cable forces on extradosed bridge cables might be inadequate to identify cable forces.

In this work, numerical modelling of an extradosed bridge cable saddled on a circular deviator at pylon is conducted. The model is validated with the catenary analytical solution and its static and dynamic behaviours are studied. The effect of a saddle support is found to positively affect the cable stiffness by geometric means; longer saddle radius increases the cable stiffness by suppressing the deformations near the saddle. Further, accounting the effects of bending stiffness in the numerical model by using beam elements show considerable deviation from models with truss elements (i.e. zero bending stiffness). This deviation is manifested when comparing the static and dynamic properties. This motivates a more thorough study of bending stiffness effects on short cables.

Bending stiffness effects are studied using two rods connected with several springs along their length. Under bending moments, the springs resist the rods' relative axial displacement by the springs' transverse component. This concept is used to identify bending stiffness values by utilizing the parallel axis theorem to quantify ratios of the second moment of area. These ratios are calculated based on the setup of the springs (e.g. number of springs per unit length, transverse stiffness, etc...). The numerical model based on this concept agrees well with the theoretical values computed using upper and lower bounds of the parallel axis theorem.

The proposed concept of quantifying ratios of the second moment of area using springs as connection between cable rods is applied on an actual extradosed bridge geometry. The model is examined by comparison to the previously validated global numerical model. The two models showed good correlation under various changing parameters. This allowed further study of the effects of stick/slip behaviour between cable rods on an actual bridge geometry.

Keywords: Extradosed bridge, nonlinear cable analysis, bending stiffness of cables.

Contents

List of Figures

List of Tables

Dedicated to my family and my wounded country...

Chapter 1

Introduction

General

The choice of an appropriate bridge to span an obstacle depends on balancing several parameters such as: the high cost of such a structure, the span length to be covered, aesthetic requirements and material to be used. Figure 1.1 illustrates common types of spanning structural systems.

Continuous beam systems covering spans between 30 and 100m are characterized by prestressed box girder bridges. Covering spans over 100m with such system require deep and heavy deck cross sections. Moreover, conventional cable-stayed bridges appear to be uneconomical for spans less than 200m [1, 7].

The extradosed bridge may be considered as the optimum structural system for spans between 100 to 200m. Extradosed bridges are characterized by shorter pylons than cable-stayed bridges and a much shallower deck/girder structure than used on prestressed box girder bridges (figure 1.2). The system is considered therefore more cost effective for the aforementioned span lengths. Stay cables of extradosed bridges carry 60-80% of the total dead load by the vertical component of the cable, while the horizontal component prestresses the girder [8]. Vertical and horizontal components are governed by the inclination angle of the cable, which in turn is governed by the cable configuration and the height of the pylon. It is, however, noted that a form finding method for the extradosed bridges is yet to be established [8].

Motivation

The growing use of cables as structural elements has put a strong demand on the development of techniques to assess their behaviour both during construction and at several stages during the structure's lifetime [9]. Due to the simplicity of application and to the high accuracy reached in many cases, the identification of cable forces based on their vibrations has been widely used in engineering practice [10]. Such methods apply highly mobile vibration measurement devices (e.g. smartphones) to identify cable forces [11]. The use of the vibrating chord theory, poses no particular problem except for the range of applicability. The theory is based on the assumption of a non-sagged cable pinned at both ends. Despite the application easiness of the formula relating natural frequency and installed force, some questions are frequently raised concerning the extension of application of this or of derived

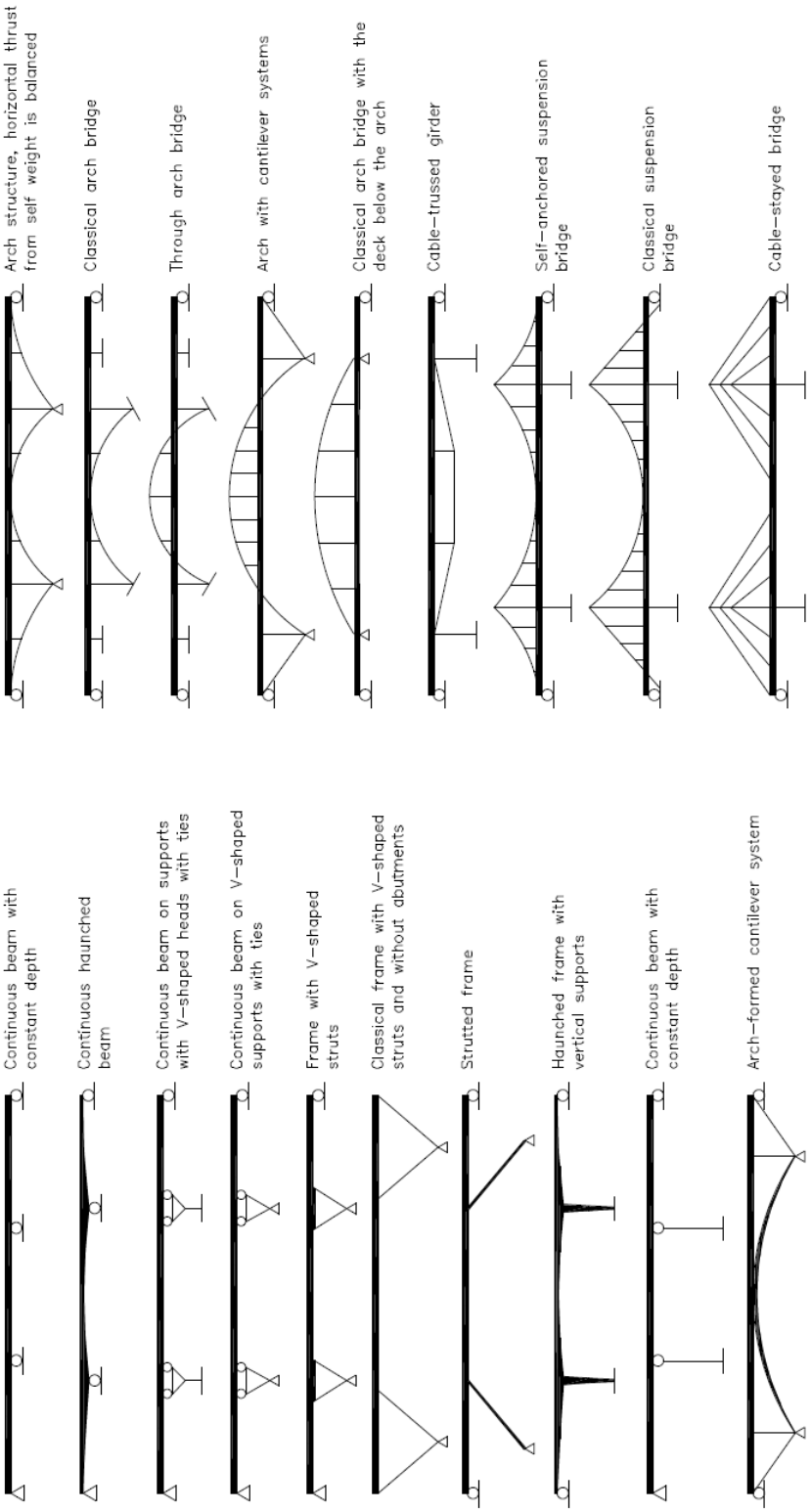

Figure 1.1: Some common structural systems of bridges [1, 2]

Figure 1.2: Shin-Meisei extradosed bridge, Japan. Main span = 124m.

Courtesy of [wikiwand. com/ en/ Extradosed_ bridge]

formulae to very long or very short cables and to low tensioned cables with known/unknown support characteristics [12, 10].

Extradosed bridge cables are deviated from one end at the substructure (i.e. the deck) to the other by the pylon using saddle deviators. The configuration of the saddle at the pylon can trigger the aforementioned uncertainty regarding the support flexibility. In addition, the cables for extradosed bridges are shorter than cables of cable-stayed bridges, this allows higher influence of bending stiffness on the vibration behaviour as it is known to affect higher mode vibrations [12, 10]. Bending stiffness values of cables are not fully understood between well-known upper and lower bounds. This uncertainty is deemed a resultant of unidentified frictional effects between cable wires. Conventional contact algorithms describing the frictional behaviour are computationally inefficient and might not converge [13]. Other methods of refined numerical modelling can be applied to clarify these uncertainties in local models and the findings of those refined models can be developed for application on global models.

The aforementioned uncertainties have motivated the research presented in this thesis.

Organization of the Thesis

This thesis contains six chapters organized as such:

- Chapter 1 introduces the topic and what motivates this research.
- Chapter 2 presents the current stay cable technology and explains the theoretical bases of their static and dynamic properties. Further, it includes a description of the numerical principles used in this thesis.

- Numerical modelling of an extradosed bridge cable with a proposed geometry configuration is introduced in chapter 3 including the validation of the numerical model with the catenary analytic solution. The effect of a saddle configuration on the overall deformations of the cable is investigated in addition to the static and dynamic characteristics of the numerical model.
- Bending stiffness of cables is investigated in chapter 4 and chapter 5. In the former chapter, a numerical method is proposed to define the friction between cable rods using the transverse component of springs distributed along the rods' length. The method is applied in the latter chapter on an extradosed bridge geometry and the stick/slip between rods is outlined.
- Chapter 6 summarizes the work done in this thesis and outlines further aspects that could be studied.

Chapter 2

An Overview on Stay Cables

2.1 Introduction

This chapter deals with different types of cables namely; Locked Coil ropes, parallel wire cables, parallel strand cables and parallel bar cables. Their static and dynamic behaviour under loading is a central concern to their installation and usage. The static behaviour follows the the catenary function of an idealized cable (i.e. no bending stiffness as in a prestressed chain) while there are other more explicit solutions that provide simplified equations to determine certain parameters. The dynamic behaviour deals with studying the dynamic characteristics of a vibrating cable such as the vibrating chord theory and its modified version that includes the effects of bending stiffness. This chapter also covers the numerical principles used in this thesis such as types of elements used for modelling as well as types of analysis.

2.2 Types of Stay Cables

Stay cables are generally categorized into locked coil ropes, parallel wire cables, parallel strand cables and the hardly anymore used parallel bar cables. Table 2.1 describes the usual parameters of the main cables used nowadays. An overview of stay cable systems is briefly described in this section with an emphasis on the cross-section arrangement, typical dimensions of components, corrosion protection and other general remarks.

Table 2.1: General parameters of stay cable systems [3]

Characteristics	Locked coil ropes	Parallel wire cables	Parallel strand cables
E [GPa]	170	205	195
f_u [MPa]	1470	1670	1870
$\Delta\sigma$ [MPa]	150	200	200

2.2.1 Locked Coil Ropes

Locked coil ropes consist of internal round wires with a diameter of 5mm and outer layers of Z-shaped wires with a depth of 6-7mm. Each layer of wires rotate in the opposite direction from the adjacent one to achieve twist free ropes as depicted in figure 2.1. When stressing the cables, the Z-shaped outer wires are pressed against one another by lateral contraction, which 'locks' the rope surface against the intrusion of water. An advantage of a locked coil rope is good corrosion protection; achieved by galvanizing of wires or filling the interstices between the wires with polyurethane (PU) filler and zinc and aluminium dust. Another advantage would be relatively simple maintenance with either visual inspection, which could also be achieved by self-propelled video cameras, or by magnetic induction inspection, which detects wire breaks and their location within the rope cross-section. Disadvantages are known to be: reduced stiffness, subjection to creep and reduced tensile and fatigue strength especially near the anchorage, as the cable is usually anchored by hot casting. [3].

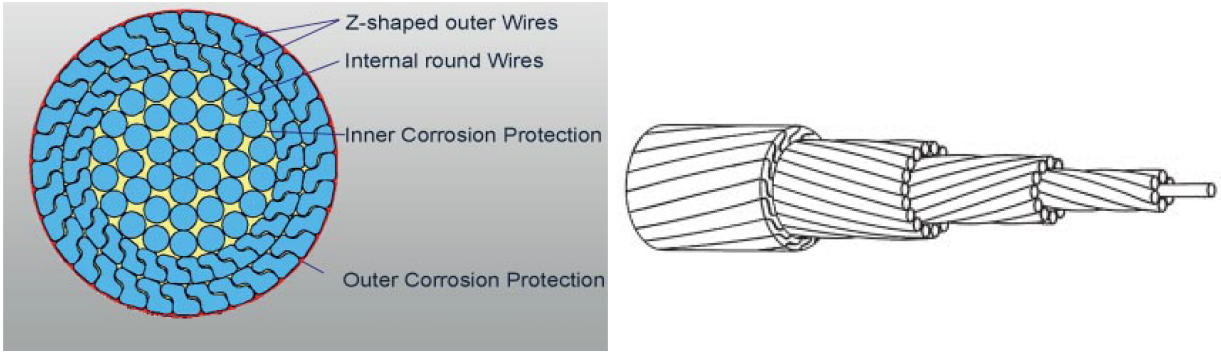

(a) Cross-section of locked coil rope

(b) Opposite rotation of adjacent layers

Figure 2.1: Locked coil ropes. *As obtained from [3]*

2.2.2 Parallel Wire Cables

Parallel wire cables comprise a bundle of straight wires with 7mm diameter high-strength, drawn steel and are placed in metal or polyethylene ducts. The ducts are generally injected with cement grout to achieve corrosion protection. The fatigue strength near the anchorage (a known concern in cable anchoring) is a major advantage of this type of cable, particularly because of the avoidance of hot casting by means of a special type of anchorage, which in turn uses a combination of mechanical and chemical adhesion mechanism that does little or no harm to the micro-structure of the wire material.

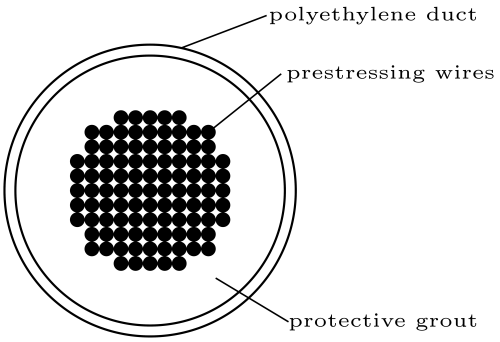

Figure 2.2: Parallel wire cables

As taken from [2]

2.2.3 Parallel Strand Cables

Parallel strand cables comprise several 7-wire strands kept apart using spacers. The major advantage of using smaller wire diameter for this type of cable is that smaller wire of 5mm in diameter have an increased tensile strength of around 1870 MPa when compared with 6.4mm diameter wires with a tensile strength of around 1670 MPa, referring to the cold-drawn nature of manufacturing this type of wires. Parallel strand cables are more economical as they are assembled strand by strand on site and don't require any grouting. This allows future exchanges of individual damaged strands as well as reducing the cost of transportation on site.

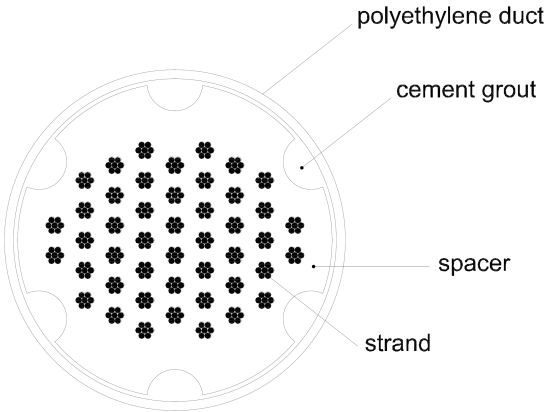

Figure 2.4: Parallel strand cables

As taken from [2]

Figure 2.6: Parallel strand cables

courtesy of [www.dsiamerica.com]

2.2.4 Parallel Bar cables

This cable system comprises stress threaded bars of 16mm in diameter. The steel bars are fixed in place by spacers and installed in a thick walled steel tube. After installation the steel tube is grouted and permanently protected against corrosion. Nowadays this type of cables has virtually disappeared from the market for economic reasons [3].

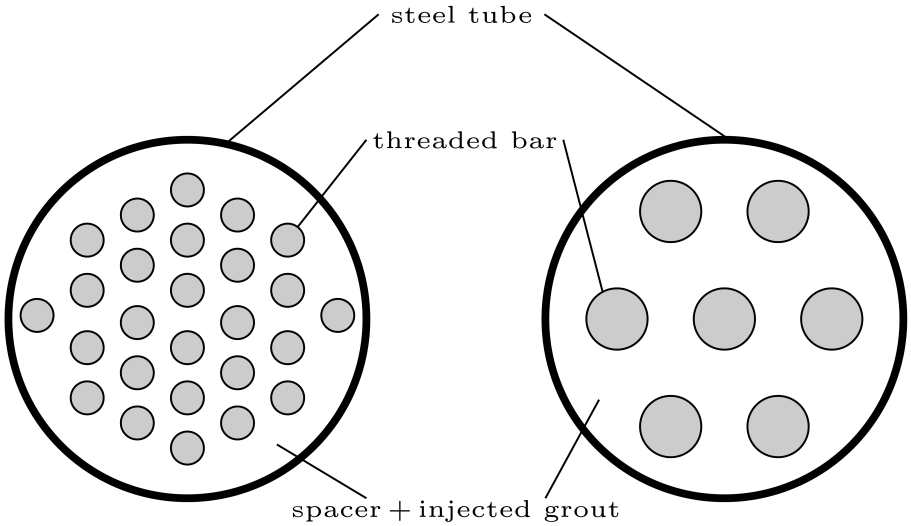

Figure 2.8: Parallel bar cables

As taken from [2]

2.3 Static Behaviour

A straight cable can be idealized as a prestressed chain where the stiffness arises almost entirely from the longitudinal prestress [3]. The analytic models for a sagged cable with zero bending stiffness

adhere to the catenary solution with geometry discussed in section 2.3.1

2.3.1 The Catenary

The catenary problem is as old as 1691 in which Gottfried Leibniz, Christiaan Huygens, and Johann Bernoulli derived the equation in response to a challenge by Jakob Bernoulli. The derivation is well explained by [6] using the vertical and horizontal equilibrium of an infinitesimal element and is further developed to fit a prestressing cable configuration by [14] (refer to the appendix for details). The analytical solution for the catenary is as follows:

$$y(x) = \frac{H}{g}\cosh(\frac{g}{H}x + K_1) + K_2 \tag{2.1}$$

$$K_1 = \sinh^{-1}(\frac{gl_v}{2H\sinh\frac{gL_c}{2H}}) - \frac{gL_c}{2H} \tag{2.2}$$

$$K_2 = -\frac{H}{g}\cosh(K_1) \tag{2.3}$$

With $y(x)$ being the vertical coordinate of the catenary for x, H being the horizontal component of the tension for T, g being the self-weight per unit length of the cable, l_v and l_h being the vertical and horizontal projections of the chord length L_c as shown in figure 2.10. The vertical sag $fm(x)$ at point x would be the vertical coordinate of the chord at that point minus the outcome of equation (2.1) $y(x)$. Other explicit analytical solutions are covered in section 2.3.2

2.3.2 Ernst Analytical Models

The sagged length of a cable is calculated by Ernst [15] as:

$$L^2 = 4\frac{H^2}{g^2}\sinh^2(\frac{l_h g}{2H}) + l_v^2 \tag{2.4}$$

The maximum vertical sag at $l_h/2$ is then calculated as such:

$$fm = \frac{L}{2}\coth\left(\frac{l_h g}{2H}\right) - \frac{H}{g}\cosh\left[\tanh^{-1}\left(\frac{l_v}{L}\right)\right] \tag{2.5}$$

The effective modulus of elasticity E_i for a stress value σ and a cross-sectional area A defines the longitudinal stiffness E_iA as such:

$$E_iA = \frac{E_e}{1 + \frac{(\gamma l_h)^2}{12\sigma^3}E_e}A \tag{2.6}$$

where γ being the unit weight of the cable material. Figure 2.11 depicts equation (2.6) for different cable lengths.

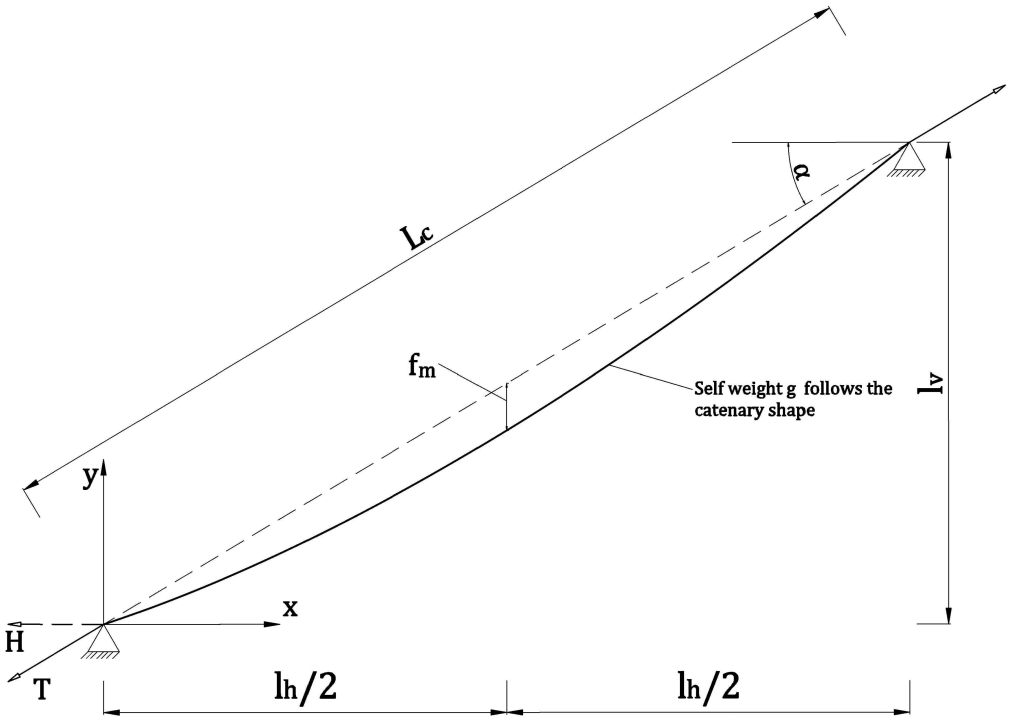

Figure 2.10: Schematic showing a perfectly flexible prestressed wire sagging under its self-weight

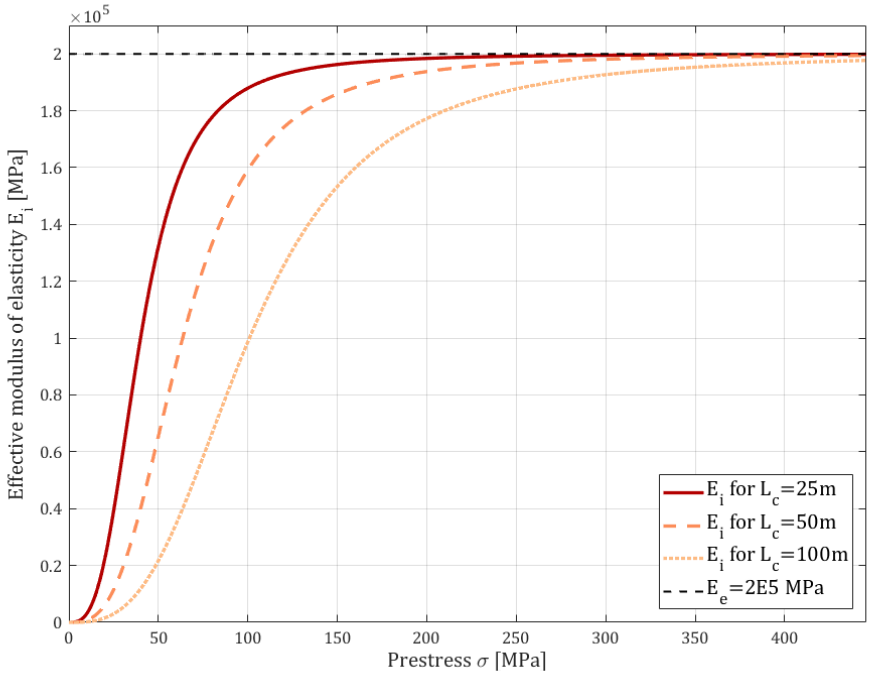

Figure 2.11: Relationship between Effective modulus of elasticity and prestressing.

$L_c = 25m$, $50m$ and $100m$.

2.4 Dynamic Behaviour

Understanding the dynamic nature of cables analytically allows the estimation of important parameters (e.g. tension forces) that directly relates to the durability and proper functionality of stay cables. The particularity of the equation of motion for a cable includes the tension force, the sag extensibility and the bending stiffness [12]:

$$E_i I \frac{\partial^4 w}{\partial x^4} - T \frac{\partial^2 w}{\partial x^2} + m \frac{\partial^2 w}{\partial t^2} - h(t) \frac{\partial^2 y(x)}{\partial x^2} = 0 \tag{2.7}$$

Different analytical solutions are proposed relating to the natural frequency f_n for each vibrating mode n, the tension force T, the cable mass per unit length m, the bending stiffness $E_i I$, the vertical deflection w and the dynamic tension $h(t)$, where $y(x)$ is the geometric shape of the cable. Other analytical models take into consideration the flexibility of the anchorages [12].

2.4.1 Vibrating Chord Theory

This theory traces back to the french polymath Marin Mersenne in the 17th century who managed to propose a model based on observations describing the vibrating nature of musical strings [16]. His work was extended by Irvine and Caughey [17] and was introduced as a descriptive linear model describing the nature of cable vibrations based on three assumptions: (1) The cable is pinned on ends; (2) The sag to span ratio (f_m/L_c) does not exceed 1/8; and (3) The cable deforms elastically [11]. In addition, the vibrating chord theory assumes zero bending stiffness string i.e. as a prestressed chain. The relationship is given in equation (2.8) where L_c is the chord length of the cable .

$$\left(\frac{f_n}{n}\right)^2 = \frac{T}{4mL_c^2} \tag{2.8}$$

This equation provides simplicity in application and is even applied using highly mobile vibration measurement devices e.g. smartphones, as presented in [11]. Moreover, the equation is verified according to [10] for a wide range of situations related with stays of cable-stayed bridges. However, some improvements are required to account for more complex cases, involving for example: Low tensioned cables, short tendons, flexible anchorages and long sagged cables.

2.4.2 Bending Stiffness Effects on Natural Frequencies

For cases where accounting for the bending stiffness is necessary, such as short stiff tendons or low tensioned cables, equation (2.9) is a development of equation (2.8) to account for the bending stiffness effects such that:

$$\left(\frac{f_n}{n}\right)^2 = \frac{T}{4mL_c^2} + \frac{n^2\pi^2}{4mL_c^4} E_i I \tag{2.9}$$

In general cases, the tension force governs the early modes of vibrations (i.e. from first to the fifth mode) since the bending stiffness effects can be deemed negligible. Bending stiffness effects on the natural frequencies will have most effects in higher mode numbers as can be seen in figure 2.13.

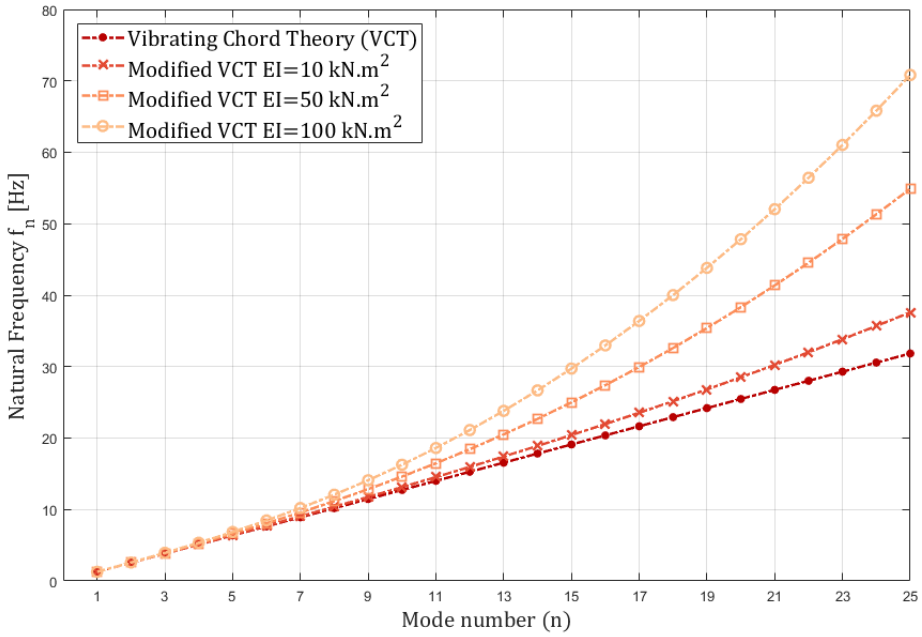

Figure 2.13: Comparison between the vibrating chord theory and its modified version.

$T = 250kN$, $L_c = 25$m, $m = 61.654$kg/m.

2.5 Principles of Numerical Analysis for Stay Cables

This section describes the numerical features that are used in the numerical modelling of this thesis. The numerical solver used is the software SOFiSTiK and this section covers the numerical attributes provided by it.

2.5.1 Types of Elements used

Truss Element

The truss element is a two-node member which transmits axial force only and, in general, has three global translation components at each node. The stiffness of the truss element in a linear elastic analysis depends merely on the axial stiffness in the longitudinal direction and transmits no moments. Stay cables in practice are generally modeled with truss elements for their less computational demands than say, beam elements.

Cable Element

The cable element behaves like truss element receiving axial forces only during a linear elastic analysis. In a nonlinear analysis, however, the cable element does not sustain any compression forces.

Beam Element

The beam element is defined by two nodes and a cross-sectional description (i.e. second moment of area, cross-sectional area, etc...). The stiffness of the beam element in a linear elastic analysis depends on the bending stiffness around local y ($E_i I_y$) and z ($E_i I_z$) axes (x-axis being the perpendicular to the cross-section) in addition to the axial stiffness $E_i A$. The type of beam elements used in this thesis is the slender Euler-Bernoulli beams.

Spring Element

A spring element is connected to one or two nodes on the numerical model. It can provide axial, lateral and/or rotational stiffness [5]. For a linear analysis, the spring in the principle direction will deflect a distance u depending on the axial force applied on the spring F_P and the spring stiffness K_P (P stands for principle direction) as $F_P = K_P \cdot u$. For the lateral direction, a spring will provide a transverse resistance to the force F_T. This resistance is utilized by stiffness constant K_T and the corresponding lateral displacement v is calculated as such $F_T = K_T \cdot \mathrm{v}$ as seen in figure 2.15.

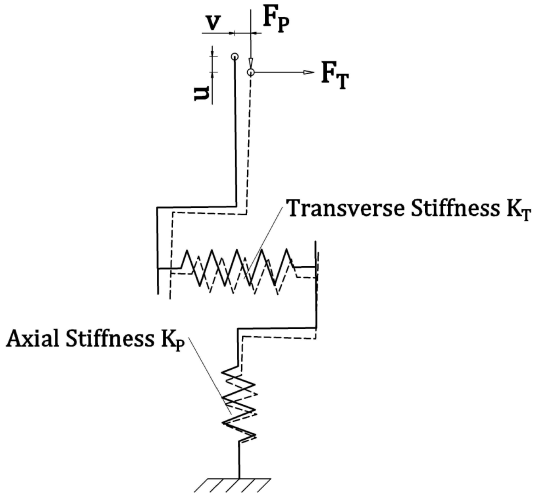

Figure 2.15: Sketch depicting the behaviour of the axial and transverse component of a spring element

2.5.2 Nonlinear Analysis

Nonlinear analysis accounts for material nonlinearity and geometric nonlinearity. The material nonlinearity required in this thesis would manifest itself in nonlinear springs. Material nonlinearity correspond to the nonlinear relationship between stress and strain, while geometric nonlinearity corresponds to the nonlinear relationship between displacement and strain or rotation and curvature. It exists in systems undergoing large deformations or deflections. [18].

Second and third order theory

Figure 2.16 and figure 2.17 clarify SOFiSTiK's essential characteristics of second and third order theory analysis. In the column example of figure 2.16 the effect of second order analysis (TH2) reduces the material stiffness due to secondary moments caused by the compression force P_z. This creates an additional deflection in x-direction with no change in z-direction, causing the virtual elongation of the beam. This increase in length of the beam adds to the secondary bending moment as the displacement dux is increased by the elongation. This type of analysis is often referred to as P-Δ analysis. However, in the complete geometric nonlinear analysis (TH3), the same type of analysis conducted in TH2 is performed in addition to accurate geometry updates, thus causing no virtual elongation. The column head follows the physical path and equilibrium is reached iteratively on the 'real' deformed shape.

In figure 2.17 a horizontally pinned beam is loaded. In TH2 the beam deflects without an increase in normal force N. In the TH3 analysis, however, the vertical displacement causes a lengthening of the beam which in turn creates a tension force N that carries a part of the load and reduces the vertical deformation.

TH3 is used to describe the geometric sytem modifications such as snap through, length modification for big deformations and behaviour after buckling [4].

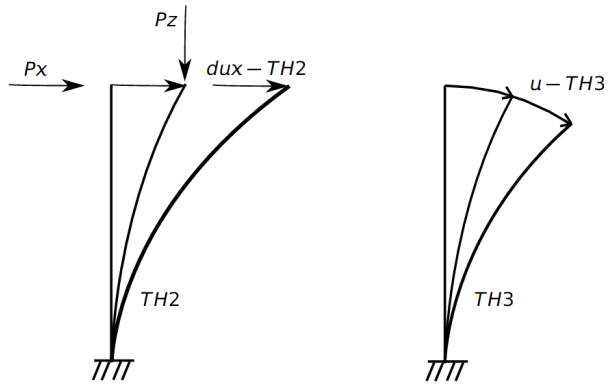

Figure 2.16: Illustration of second and third order nonlinear analysis on a column [4]

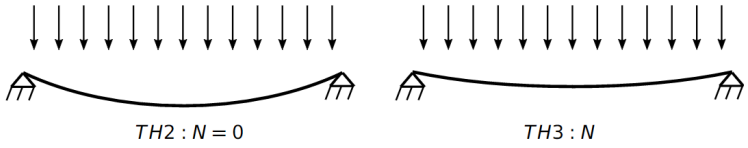

Figure 2.17: Illustration of second and third order nonlinear analysis on a beam [4]

Nonlinear springs

SOFiSTiK identifies nonlinear springs with characterized parameters. The following list (illustrated in figure 2.18) describes the used nonlinear behaviour of SoFiSTiK springs used in this thesis.

- Gap: The spring transmits forces along its axis only after its deformation has exceeded the gap.
- Failure load: Upon reaching the failure load CRA, the spring fails in both the axial and the lateral direction.
- Yield load: Upon reaching the yield load YIEL, the deformation component of the spring increases in its direction without a corresponding increase of the spring force.
- Friction coefficient: If a friction coefficient and/or a cohesion are input, the lateral spring can not sustain forces greater than $\mu \cdot F_{CP} + C$ where μ is the frictional coefficient, F_{CP} is the compression force in the principle direction and C being the cohesion or additional force.

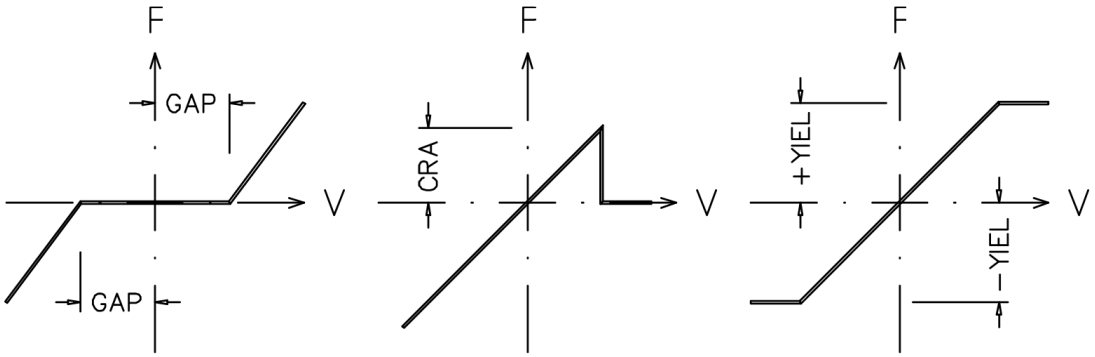

Figure 2.18: Nonlinear springs as described by SoFiSTiK [5]

Chapter 3

Stay-cable Analysis of Extradosed Bridges

3.1 General

Extradosed bridges are considered the most suitable structural system for spans between 100 and 200m and can be defined as a quasi-hybrid structural system between prestressed box girder bridges, which require deep and heavy profiles for spans longer than 100m, and cable-stayed bridges,which are deemed uneconomical for spans less than 200m [7]. Stays of extradosed bridges serve as external prestressing tendons protruding outside the deck and deviate over the pier by a short pylon. They carry 60 to 80% from the dead weight of the deck, which allows higher prestressing as the stay cables are under less live load cycles than cables of cable-stayed bridges, hence less fatigue strength demands and higher prestressing allowance [19]. The remaining dead load and live load are carried by the girder.

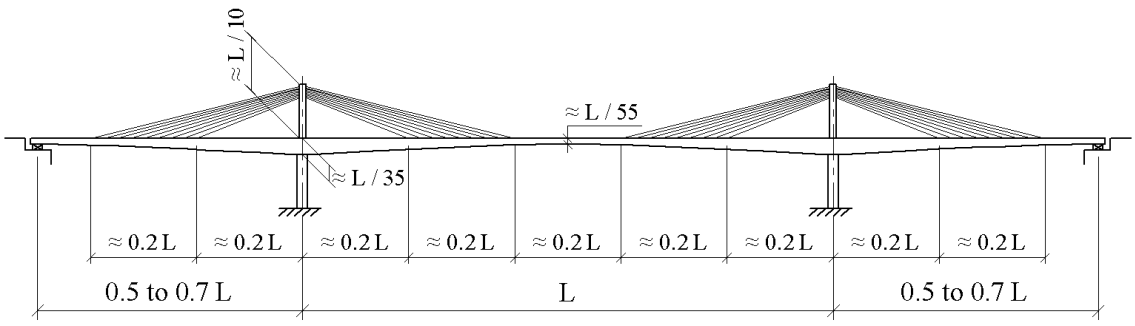

Figure 3.1: Common configuration of extradosed bridges, main span L around 100-200m.

As taken from [7]

Figure 3.3: Ganter Bridge, Switzerland 1980, Main span 174 m.

Courtesy of [wikipedia. org]

3.1.1 The Saddle Support

Cables of extradosed bridges are usually deviated from one span to the other using a saddle anchorage deviator (figure 3.5). Usage of saddles as deviators helps to save the anchorages at the pylon, simplify the design and construction of the pylon and helps to achieve a slender pylon head as the saddle normally does not occupy large space [7]. For the case of this thesis, the saddle geometry is fairly assumed to be that of a circle even though it can also be that of an oval shape or a parabola. Figure 3.7 show an achoring technique of cables to the saddle deviator using grout.

Figure 3.5: Prefabricated cable saddle.

Courtesy of [crrte. cn]

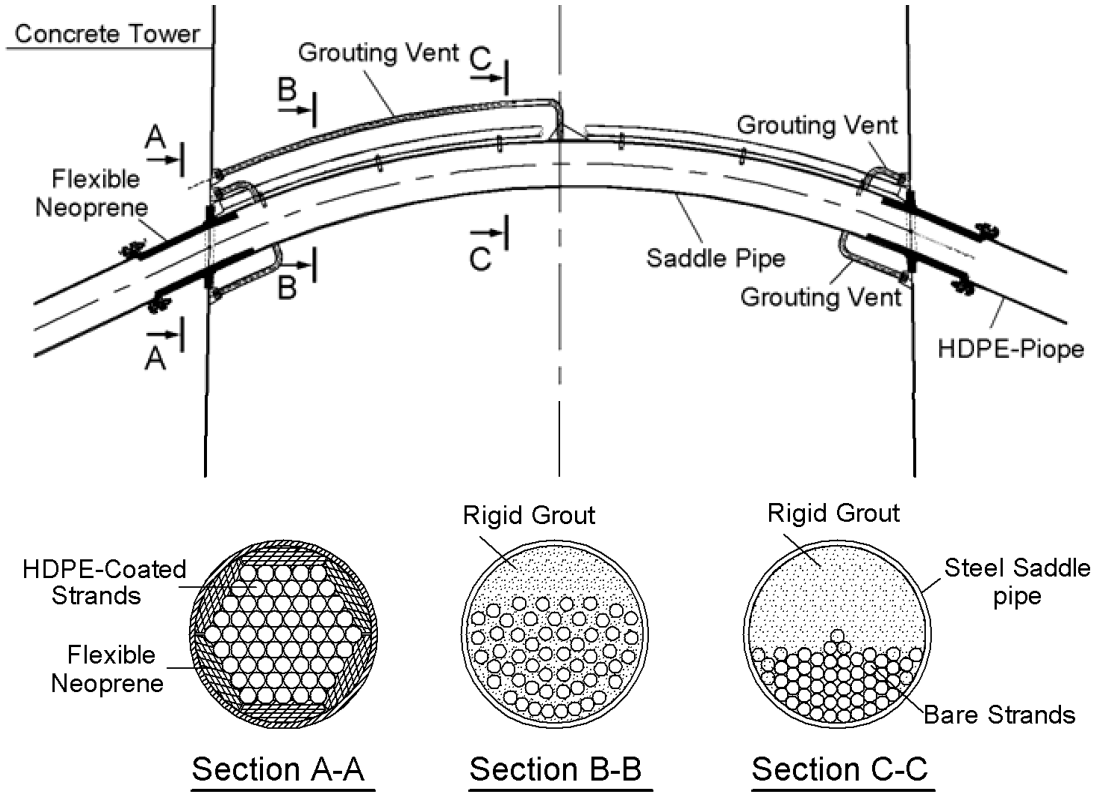

Figure 3.7: Steel saddle anchorage at pylon head using a steel saddle and cement grout.

As taken from [7]

3.2 Numerical modelling of Extradosed Bridge Stay Cable

The geometry of the cable is based on a number of parameters that represent a given case. These parameters are exploited to build the geometry of the cable. Table 3.1 shows these required parameters and their used symbols in this thesis.

Table 3.1: Used parameters for the numerical modelling

Characteristics	Symbols used
Cable inclination angle	α
Saddle radius	R
Pylon peak height	H
Chord length of cable (used in section 3.3 and 3.4)	L_c
Cable diameter	D
Modulus of elasticity	E_e
Prestressing force	T
Elements required as saddle	n_{sad}
Elements required as free cable	n_{fc}

3.2.1 Saddle Modelling

Initially, the proposed layout is assumed to be symmetrical around the vertical axis that passes through the saddle peak, therefore the global axes are chosen to be on the bottom anchorage level under the peak of the saddle e.g. the first node is located at the saddle top (X component is zero and Z component equals the pylon height H). Based on the number of elements required at the saddle region n_{sad}, equation (3.1) and equation (3.2) are used to calculate each nodal coordinate i starting from $i = 0, 1...n_{sad}$. The total number of nodes is therefore $1 + n_{sad}$.

$$x_i = R \sin\left(\frac{\alpha}{n_{sad}} \cdot i\right) \tag{3.1}$$

$$z_i = H - R + R \cos\left(\frac{\alpha}{n_{sad}} \cdot i\right) \tag{3.2}$$

After the saddle nodes have been determined, the free cable geometry, inclined with α, is determined based on the inclination angle in global X and Z axes of the straight cable as follows

$$x_{fci} = R \sin\alpha + \frac{L_{fc}}{n_{fc}} \cdot i \cdot \cos\alpha \tag{3.3}$$

$$z_{fci} = H - R\,(1 - \cos\alpha) - \frac{L_{fc}}{n_{fc}} \cdot i \cdot \sin\alpha \tag{3.4}$$

where $i = 1, 2...., +(n_{fc} + 1)$. The free length of the cable L_{fc} is defined geometrically by

$$L_{fc} = \frac{H - R \cdot (1 - \cos\alpha)}{\sin\alpha} \tag{3.5}$$

Figure 3.9 depicts the trigonometric relations used in the setup of the proposed cable around a circular saddle deviator.

It is worth mentioning that the first node defining the free cable is the same as the last node calculated in the saddle geometry ('Geometry defined contact point' in figure 3.9) since tangent at that point is the same (same inclination angle α). Each two consecutive nodes are then connected to form the finite elements.

3.2.2 Support Conditions

The saddle is modeled as 'very stiff' or 'semi-rigid' inclined spring elements ($K_P > 10^9$ kN/m) acting longitudinally on each saddle node. They are set as compression-only springs and are perpendicular to the circular perimeter of the saddle. The inclination of each spring element depends on the number of elements selected at the saddle n_{sad} and the cable's inclination angle α. Equation (3.6) describes how each spring inclination from global X and Z axes is calculated and figure 3.11 demonstrates the used concept of 'radial' springs.

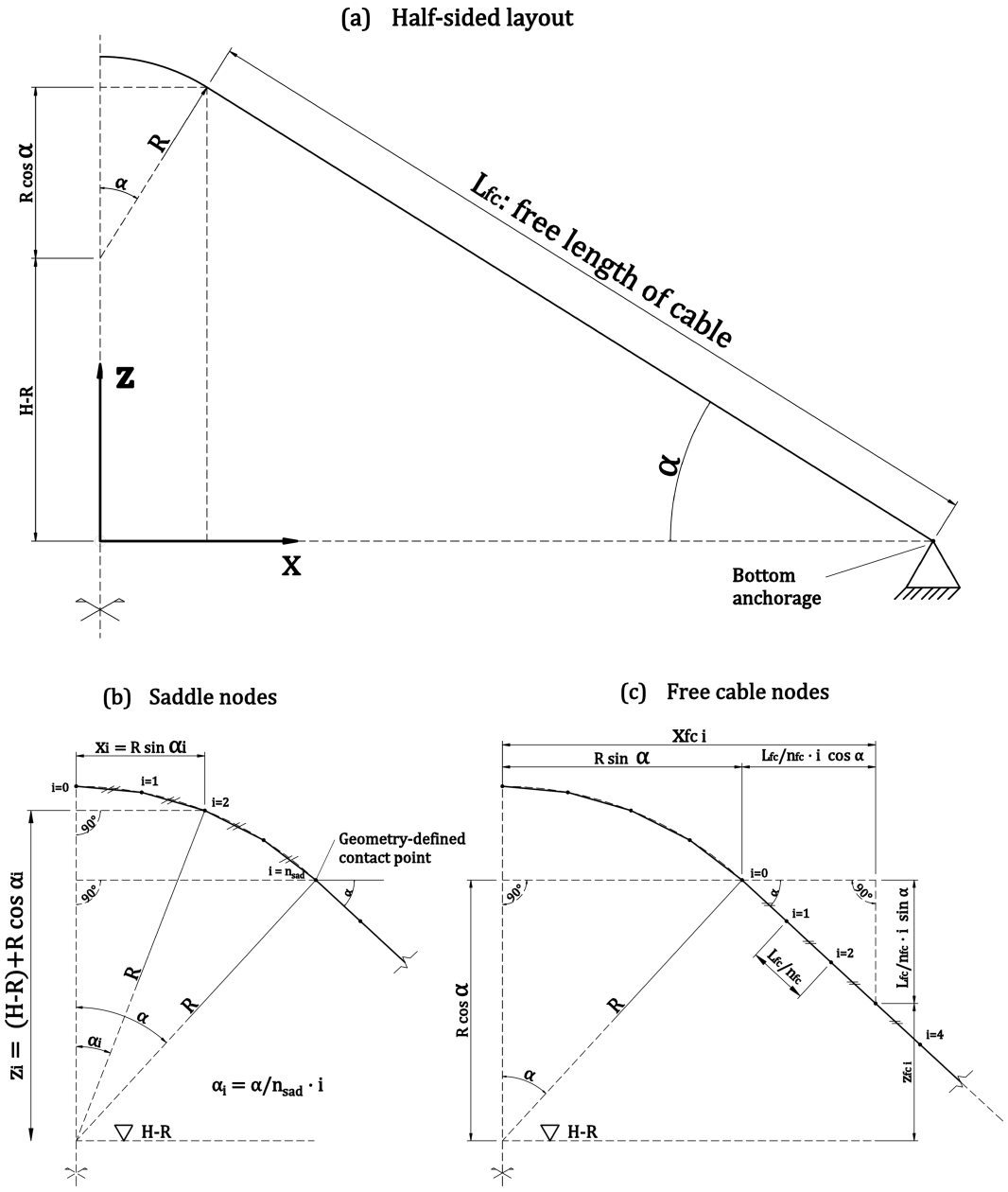

Figure 3.9: Proposed geometry setup for an extradosed bridge cable setup.

$$dX_i = \sin(\alpha_i) \quad \text{and} \quad dZ_i = \cos(\alpha_i) \tag{3.6}$$

where: $\alpha_i = \left(\frac{\alpha}{n_{sad}} \cdot i\right)$ and $i = 0, 1...n_{sad}$

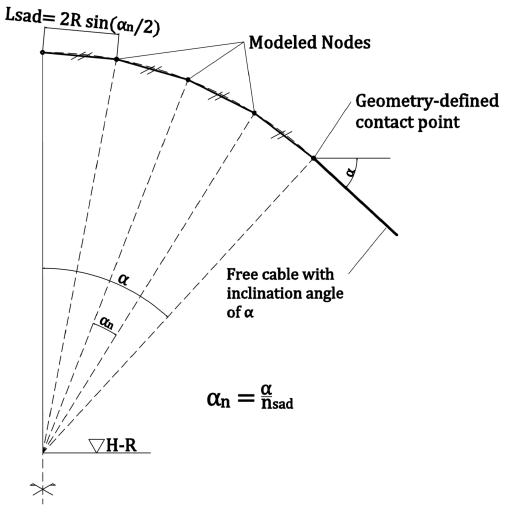

Figure 3.10: Length of each saddle element connecting two consecutive nodes as modeled. L_{sad} is determined based on the chord length equation of a circle

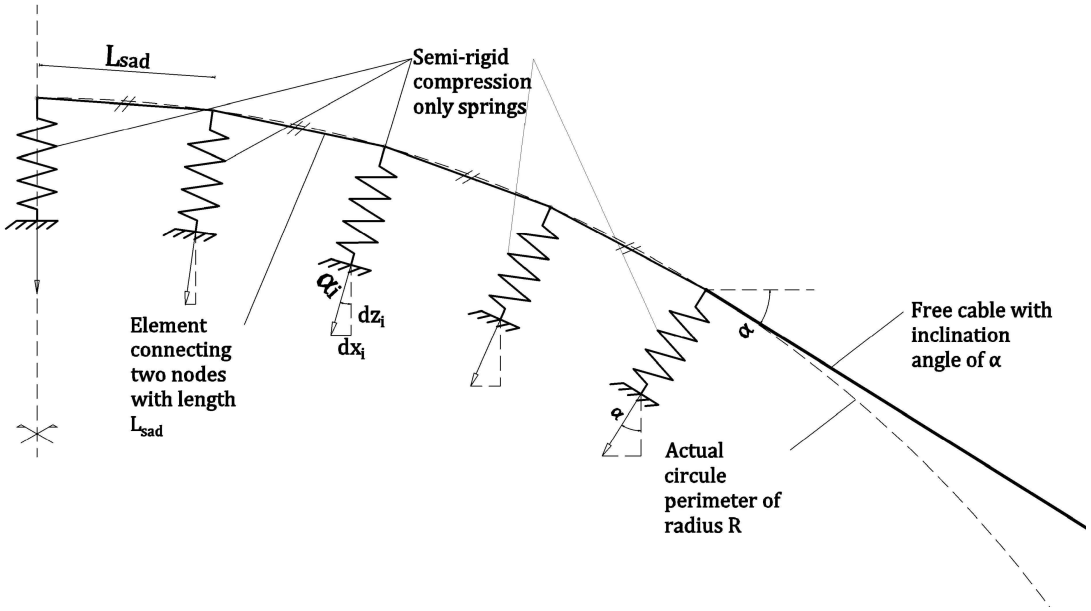

Figure 3.11: Saddle attributes as numerically modeled.

Arrows under springs represent local axial axes of the springs which are perpendicular on the saddle.

3.3 Validation of the Numerical Model

3.3.1 General

To validate the numerical model, the cable is modeled in a horizontal configuration using a third order nonlinear analysis. Lifting one end of the cable upwards by an inclination angle α allows

differentiation of support forces between the upper support (saddle) and the bottom support (bottom anchorage). This differentiation occurs due to self weight and results in the upper support carrying larger loads. By modelling the cable horizontally, support reactions would not differ since the self weight is carried equally and the prestressing force at mid-span of the cable would equal the support horizontal component H as described in figure 3.13. With that considered, a numerical model is setup using truss elements (zero flexural stiffness) to be compared with the catenary solution for various prestressing forces as well as with a saddle configuration. The parameters used in both the numerical model and in the catenary solution are shown in table 3.2.

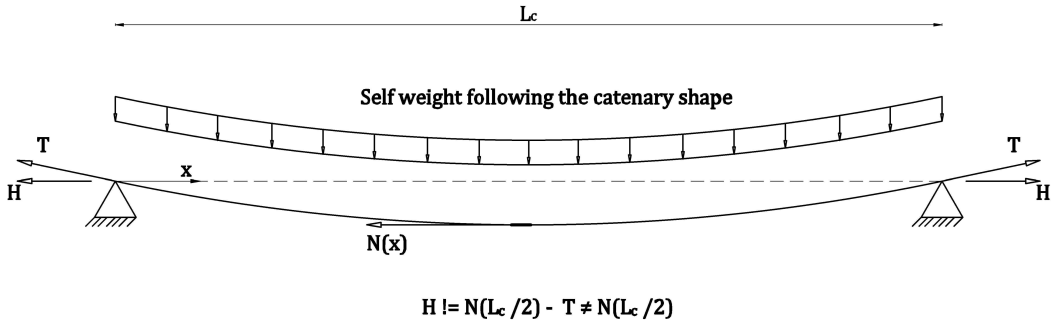

Figure 3.13: Schematic showing the case upon which the numerical model will be compared to the catenary solution

Table 3.2: Parameters used in the numerical model and the catenary solution

D [mm]	L_c [m]	m [kg/m]	E_e [MPa]
100	25	61.654	2E5

3.3.2 Effect of Prestressing Force

For various prestressing values, especially low amounts, the length of the sagged cable would exponentially increase as the prestressing force becomes lower and lower as equation (2.4) demonstrates in figure 3.14a. The sagged length is then used to update the mass per unit length of the cable m by multiplication with sagged length L to chord length L_c ratio. An inversely similar behaviour with the effective modulus of elasticity E_i is noted as the modulus of elasticity converges to the E_e in a concave shape the higher the prestressing forces as explained in equation (2.6) in section 2.3 and depicted in figure 3.14b. The effective modulus of elasticity E_i is assigned to the numerical model based on the prestressing value. Both behaviours are depicted in figure 3.14.

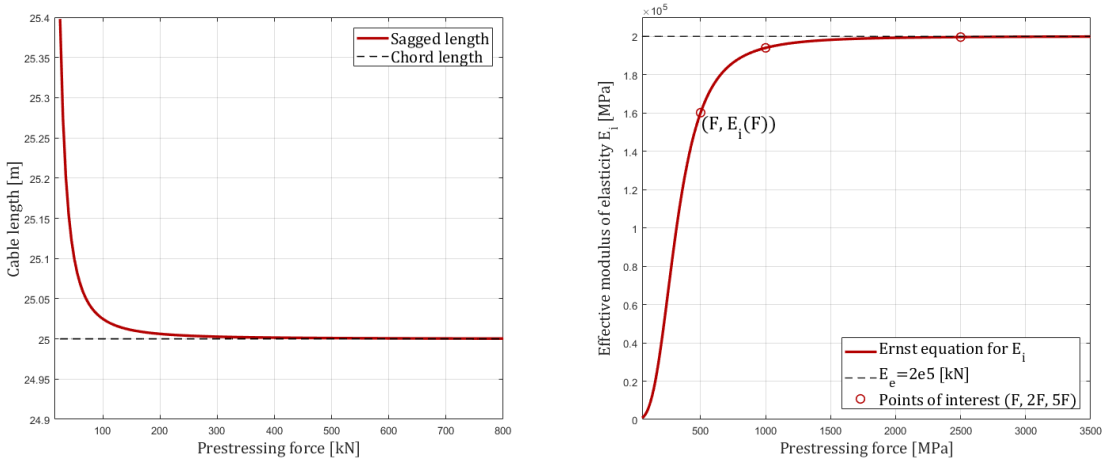

(a) Total length of sagged cable L

(b) Effective modulus of elasticity E_i

Figure 3.14: Effect of prestressing forces on cable length L and modulus of elasticity E_i. $F = 500\text{kN}$

Figure 3.15a compares between the numerical model and the catenary analytical solution - which is served as a cornerstone for this validation - for different prestressing values. Figure 3.15b depicts the residual deformation between the numerical model and the catenary solution for each chosen prestressing value. As aforementioned, the effective modulus of elasticity E_i is a function of the prestressing force T, therefore E_i is assigned to the numerical model according to the chosen prestressing forces as described in table 3.3.

Table 3.3: Effective modulus of elasticity E_i for multiple prestressing forces

T [kN]	Effective modulus of elasticity E_i [$\cdot 10^5$MPa]
500	1.6016
1000	1.93797
2500	1.996

The two solutions correlate well with highest of error values being 0.23%. This therefore validates the numerical model and demonstrates the advantage of conducting a third order analysis. The force $F = 500\text{kN}$ will be the choice for studying the effect of a saddle support instead of a regular pinned end configuration since it provides a larger sag.

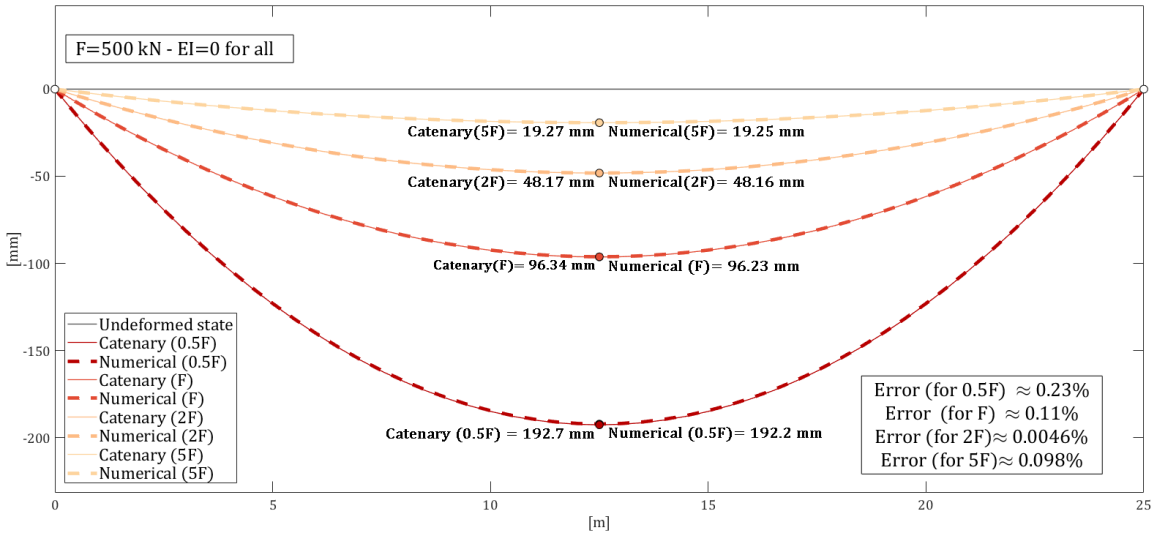

(a) Total deformations

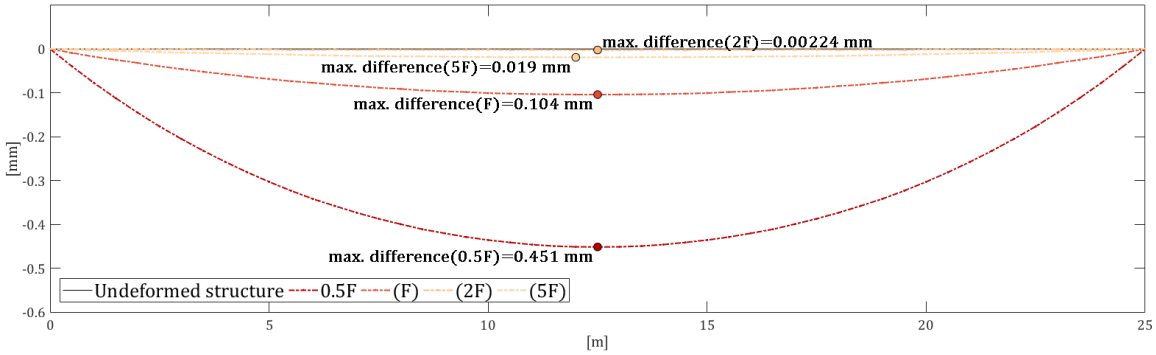

(b) Differential deformations

Figure 3.15: Comparison between the numerical model and the catenary solution for different pre-stressing forces with $F = 500$ kN.

Catenary solution plot overlaps with the numerical solution in Total deformations plot making it hardly visible.

3.4 The Effect of a Circular Saddle Support on Elements with and without Bending stiffness

3.4.1 Effect of a Saddle Support on Members with Zero Bending Stiffness

A similar study is made to the effect of saddle supports on the overall deformation for the same cable parameters of table 3.2. The cables are pinned at their ends and the saddle support is modeled numerically by using semi-rigid longitudinal springs inclined perpendicularly to the saddle perimeter with a **gap**. The gap corresponds to the distance between the saddle perimeter and the undeformed state of the cable as depicted in figure 3.17 and is calculated by utilizing the trigonometry of the right-angled triangle as $gap = \frac{R}{cos\beta_i} - R$ as illustrated in figure 3.17a. The cable would deform under its self weight vertically to activate the inclined springs according to the deformation value. Not all springs should be activated, thus studying the distance of the free sagging cable is a point of interest for a saddle configuration. The free sagging distance is the distance between the last activated spring

from each end and would be less than the chord length of the cable L_c. The last activated spring is named the 'contact point' hinting at the last nodal contact between the cable and an activated spring.

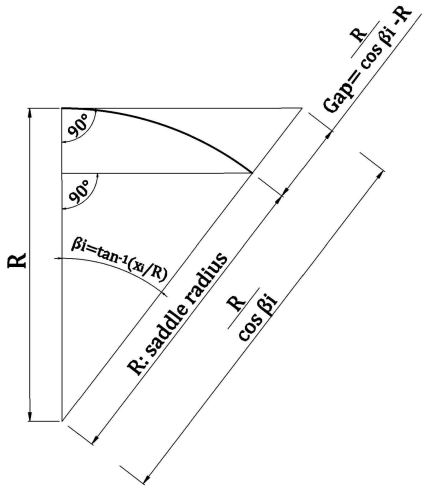

(a) Calculation of spring gap

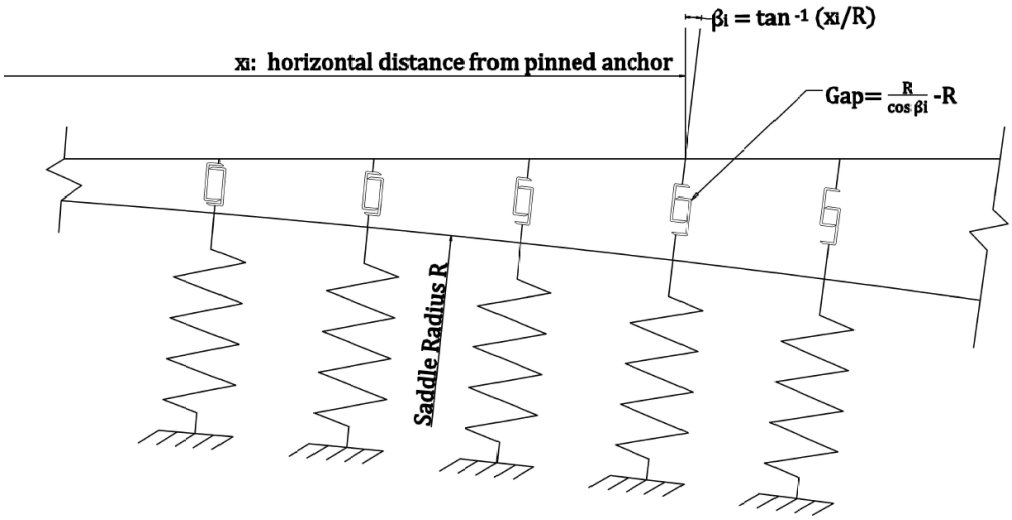

(b) Assigned gaps to radially inclined springs.

Gap shape inspired by [2]

Figure 3.17: A proposed circular saddle support characterized to numerically investigate the behaviour of cables near the anchorage.

As explained, the distance between the contact points (i.e. the free sagging length) is shorter than the distance between the pinned ends. This requires iteration steps to update the effective modulus of elasticity E_i (since it also depends on the free sagging length) in a rightful manner. The ieteration

steps are:

1. Detect the initial contact points and the corresponding distance between them (free sagging distance). The effective modulus of elasticity E_i here is calculated based on the chord length ($l_h = L_c$ in equation (2.6)).
2. Update the E_i according to the distance between the contact points.
3. Iterate from the step 1 again to correct the positioning of the contact points after updating E_i until converging to a constant value.

This iteration is done three times for the case of figure 3.18 and is repeated for as many times as required for each case for the remainder of this chapter. Whereas the biggest rotations of the pinned end cable are at the ends as seen in figure 3.18, the rotations for the saddle support setup are the same value as the tangent of the saddle until reaching the contact point. The cable deflects according to the gap distance until resting on the saddle. This implies that the rotations are confined by geometrical means until reaching the contact point, which also implies that the saddle is positively affecting the cable stiffness and this effect is of geometrical origin (function of the saddle radius R), resulting in a lower cable sag as seen in figure 3.18.

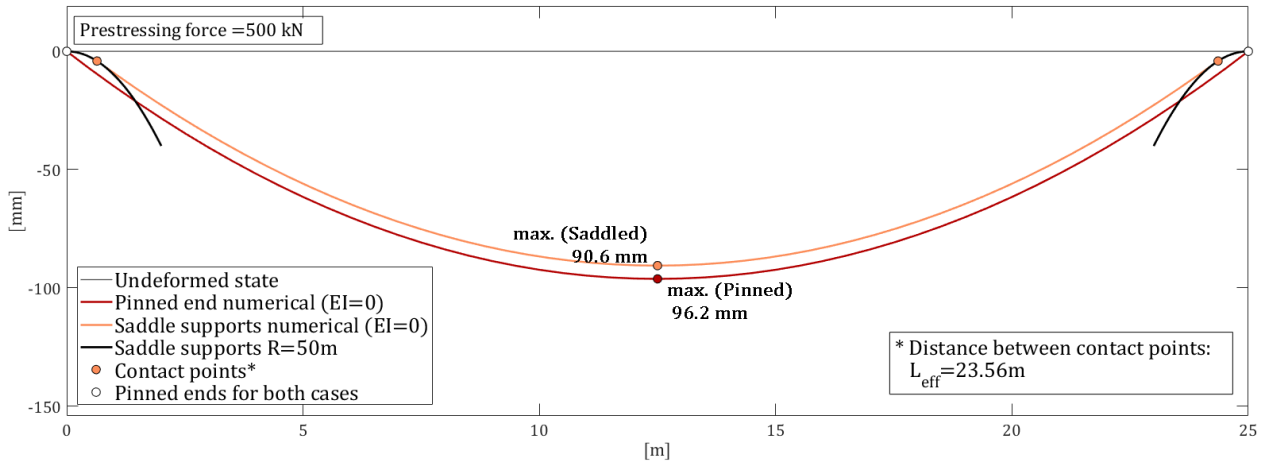

Figure 3.18: Comparison between a saddle supports configuration and a pinned end for the same prestressing value with a zero bending stiffness cable.

Decreasing the cable sag requires a lower gap distance of figure 3.17, and a lower gap distance means a bigger saddle radius. Therefore, a central finding of this analysis would indicate that the bigger a circular saddle radius is, the lower the sagging of cables, suggesting an increase in cable stiffness as a result of a defined geometry.

3.4.2 Effect of a Saddle Support on Members with Bending Stiffness

Members with bending stiffness tend to have a longer free length on a saddle setup (i.e. the closer the contact points to the anchors the higher the bending stiffness). This occurs mainly because members

activate the bending stiffness in the gap distance between the undeformed state and the saddle support, allowing the members to resist the sag at a shorter distance from the end than that required by a zero bending stiffness member. Figure 3.19a shows the overall sag of members with different bending stiffness values while figure 3.19b is a close up on the left end of figure 3.19a. The free length distances are quantified in table 3.4 for each assigned bending stiffness value.

Table 3.4: Distances between contact points from saddle supports for different members (L_c= 25m - $EI = 100$ kN.m^2).

Bending stiffness assigned to numerical model	Distance between contact points [m]
$EI = 0$	23.56
EI	24.44
$2EI$	24.87
$3EI$	24.96

relating to figure 3.19a

Commentary on the Effect of Saddle Support

The discussion of the previous sections emphasizes the role of a saddle support configuration. To model such effects, a saddle radius is chosen to result in gap distances short enough to reflect on the rotations and deformations. Higher saddle radius would probably result in more explicit interpretation of effects, the same applies for a longer cable as the sag is then higher thus allowing higher rotations at pinned ends, which would then be suppressed by a saddle configuration.

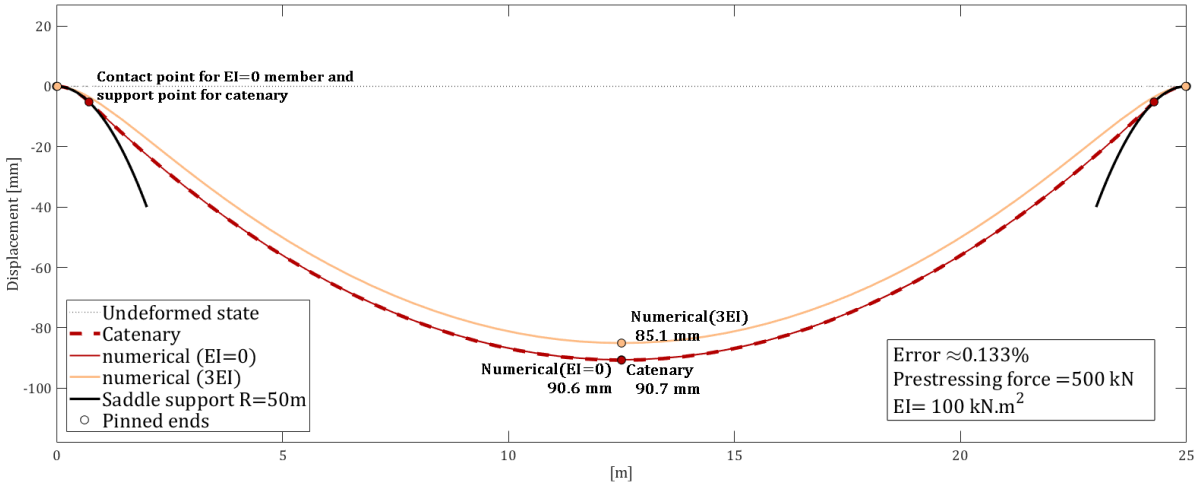

(a) Overall deflected shape

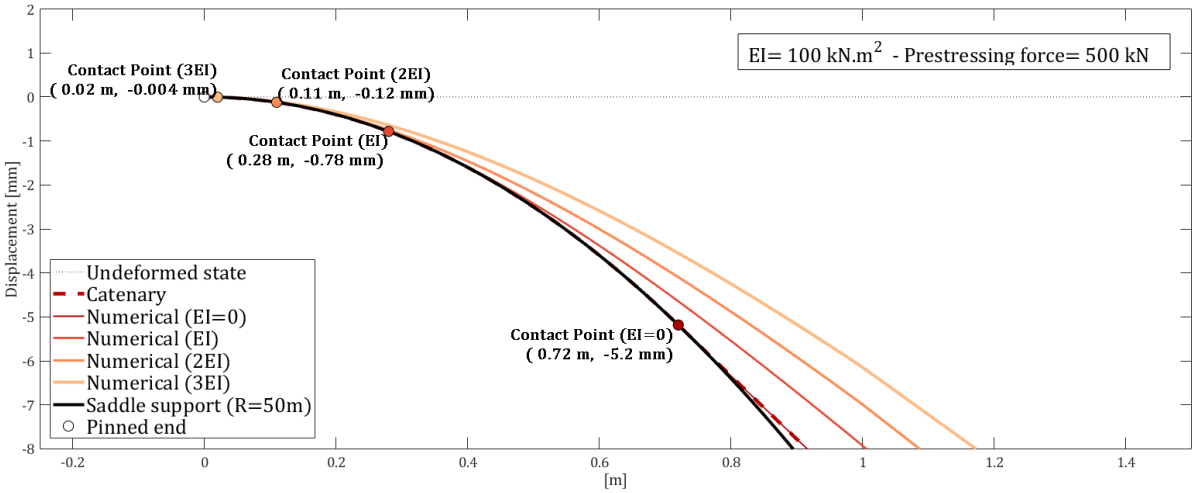

(b) Closeup of left end of figure 3.19a a saddle supports configuration such that of figure 3.17

Figure 3.19: Members with various bending stiffness on a saddle supports configuration.

3.5 Stay cable analysis on an extradosed bridge geometry

Describing the static and dynamic behaviour of the setup of **??** in an explicit way requires an example to sufficiently adapt to the case of extradosed bridge. The proposed example is shown in figure 3.20. of the cable was done using truss elements (zero bending stiffness) as mentioned in section 2.5 and the analysis was conducted using a third order nonlinear analysis to account for the geometric nonlinearity.

3.5.1 Static Behaviour

Since the saddle geometry is assumed to be that of a circle, the pressure per unit width's amplitude u at the saddle surface should be equal to the prestressing force T divided by the saddle radius R (as it gives the analytic radial pressure acting through the radius inwards to the center). The pressure from the numerical model could be obtained by summing up the spring reactions $\sum F_{P_i}$ of figure 3.21a

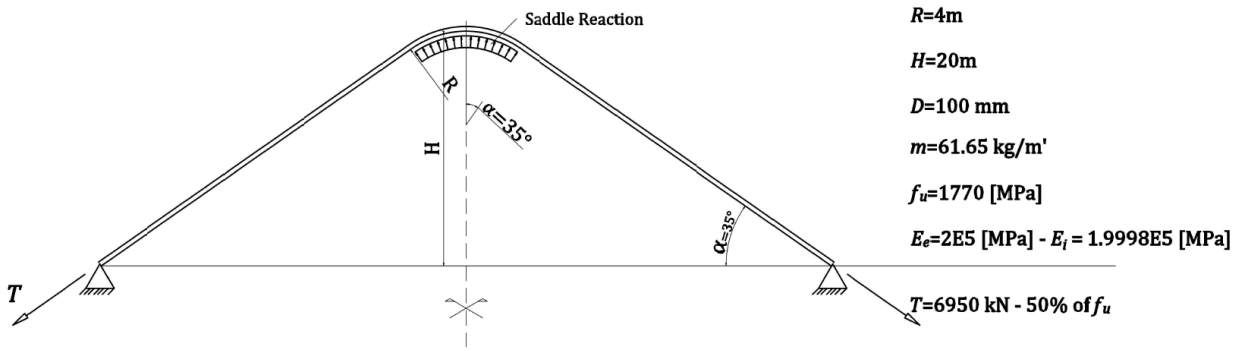

Figure 3.20: Description of parameters used in the example.

and dividing them by the equivalent saddle perimeter, which is the sum of the lengths of all elements used to model the saddle $\sum L_{sad}$. The results should lay within a small margin of radial pressure. Equation (3.7) describes the comparison.

$$\frac{\sum F_{P_i}}{\sum L_{sad_i}} \stackrel{!}{=} \frac{T}{R} \tag{3.7}$$

In this example, the saddle is divided into 25×2 elements ($\times 2$ indicates utilization of the symmetry mentioned in section 3.2.1). This gives a L_{sad} value of $\approx 0.098m$. Since the spring reactions in figure 3.21a are more or less the same, equation (3.7) could be simplified into:

$$\frac{F_{P_i}}{L_{sad}} = \frac{170.5kN}{0.098m} = 1740.8kN/m \quad \text{and} \quad \frac{T}{R} = \frac{6950kN}{4m} = 1737.75kN/m$$

The vertical component of the the springs reaction forces shown in figure 3.21b are calculated by multiplying each spring reaction by its vertical component (dZ_i in figure 3.11), then with division by the element length L_{sad} (computed as in figure 3.10), this gives the equivalent vertical pressure per unit width, which varies depending on the tangential angle (α_i of figure 3.11) along the saddle at any given point i. Since the spring reactions are validated, the maximum vertical pressure (u_{max}) and the minimum vertical pressure (u_{min}) on the saddle are located at the peak of the saddle and at the contact point of figure 3.10 respectively and are calculated as:

$$u_{max} = \frac{T}{R} \cdot \cos 0 \rightarrow 1737.75kN/m \quad \text{and}$$

$$u_{min} = \frac{T}{R} \cdot \cos \alpha \rightarrow 1737.75 \times \cos 35^\circ = 1423.48kN/m$$

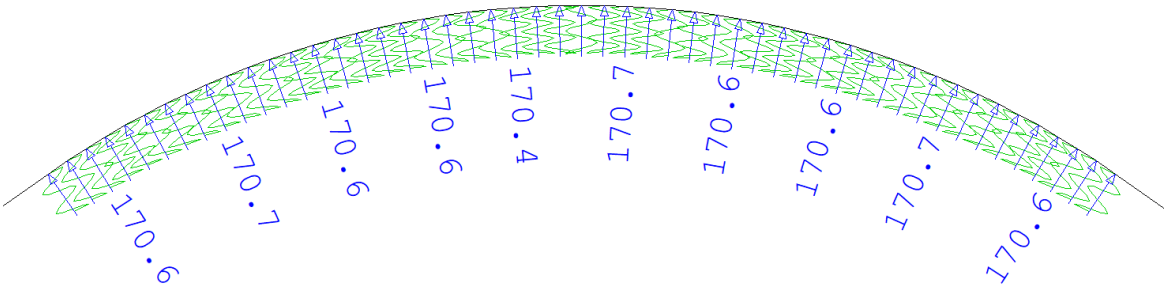

(a) Radial spring reactions [kN]

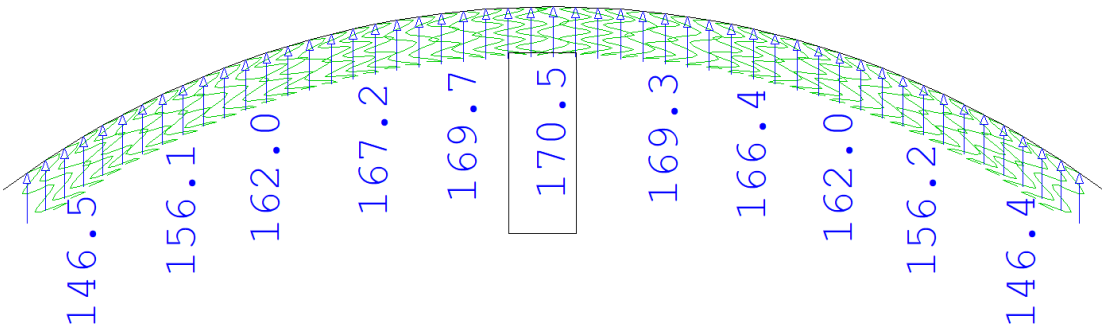

(b) Vertical component of reactions [kN] Box indicates the maximum value

Figure 3.21: Saddle force reactions represented by inclined semi-rigid axial springs

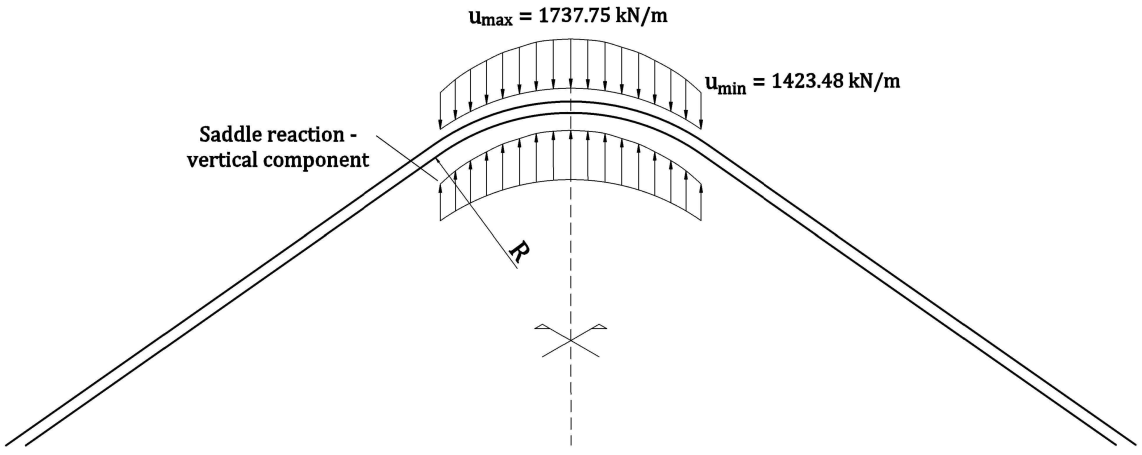

Figure 3.22: Minimum and maximum vertical pressure on the saddle.

Minimum and maximum pressure at the saddle are computed numerically. The results are given in table 3.5 and the overall distribution of the vertical pressure along the saddle is given in figure 3.23.

Table 3.5: Saddle pressure comparison between numerical and analytical solution for the given example.

Pressure per unit width	Numerical Model [kN/m]	Analytical Solution [kN/m]	Error [%]
u_{max}	1740.8	1737.75	-0.1755
u_{min}	1425.73	1423.48	-0.16

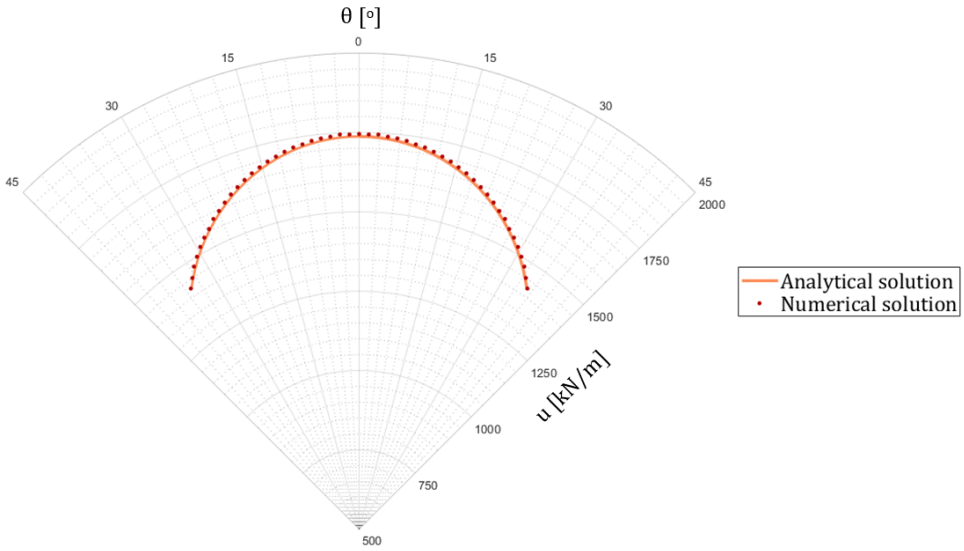

Figure 3.23: Distribution of the stresses along the saddle R axis: vertical pressure u, θ axis: cable inclination along the saddle.

The low error value ($\approx 0.17\%$) concludes that the vertical pressure per unit width u_i on the saddle is given by:

$$u_i = \frac{T}{R}\cos\alpha_i \tag{3.8}$$

And the horizontal pressure:

$$u_{h_i} = \frac{T}{R}\sin\alpha_i \tag{3.9}$$

where $\alpha_i = \sin^{-1}\left(\frac{x_i}{R}\right)$ and x_i being the horizontal component of any point i on the saddle from the symmetry axis.

To determine the vertical force applied on the pylon by the vertical pressure u_i, the area enclosed by the infinitesimal element shown in figure 3.24 is given as:

$$Area = \frac{T}{R}\cos\theta \cdot R \cdot d\theta \rightarrow Area = T\cos\theta \cdot d\theta$$

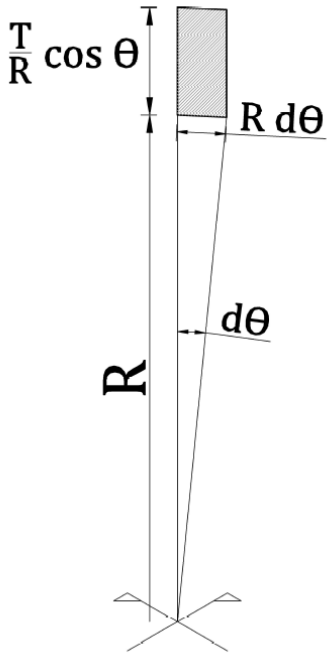

Figure 3.24: Enclosed area (shaded) of an infinitesimal element representing the vertical pressure acting on a saddle distance of $R \cdot d\theta$.

Integration of the area from 0 to α gives the total vertical force applied on the saddle F, which agrees with the vertical component of prestressing force T depicted in figure 3.25.

$$F = \int_0^{\alpha} T \cos\theta \cdot d\theta \quad = T \sin\alpha \quad \xrightarrow{\text{from symmetry}} \quad F_{total} = 2T \sin\alpha \tag{3.10}$$

The total vertical force obtained from the numerical model (sum of forces of figure 3.21b) and the forces obtained analytically are shown in table 3.6.

Table 3.6: Saddle pressure comparison between numerical and analytical solution for the given example.

Vertical Force	Numerical Model [kN]	Equation (3.10) [kN]	Error [%]
F_{total}	8046.3	7973.86	-0.91

Similarly, the horizontal stresses could be calculated, which would cancel each other for non differential prestress force T. Figure 3.25 summarizes the loading applied on a circularly-saddled pylon from a prestressed cable.

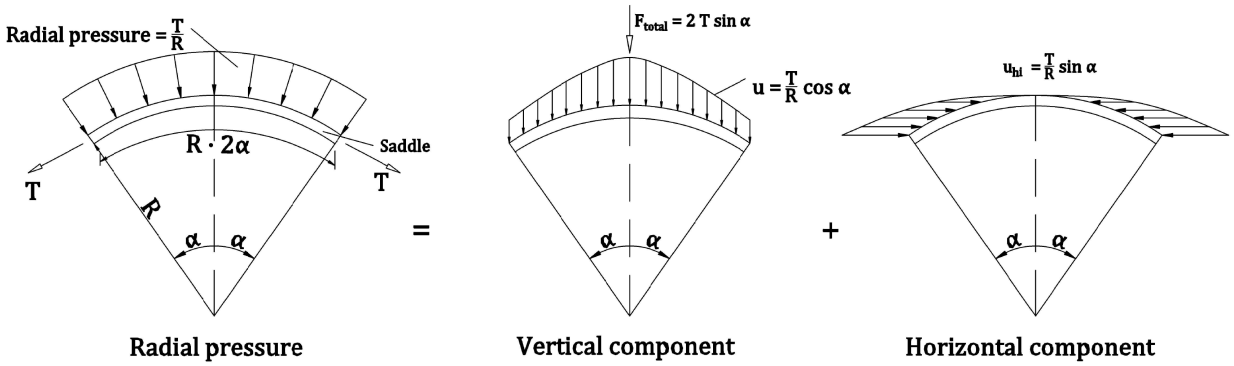

Figure 3.25: Prestressing loads applied on the saddle.

[1]

3.5.2 Modal Analysis

Due to the short height of the saddle pylon and consequently short length of the cable (free cable length in this example is $L_{fc} \approx 33.6m$) and high prestressing values, the natural frequencies are noticeably higher than those of say, cable-stayed bridges. This creates less risk of conventional wind vibration phenomena since the cables are stiffer. 'However, understanding the vibration phenomena of short and stiff cables is of a major importance since the usually neglected bending stiffness effects has a clear effect on such cable case. Therefore nonlinear modal analysis for this example is conducted on three numerical models. The first model is modeled with truss elements accounting for zero bending stiffness, the second model is modeled with beam elements with bending stiffness value $E_iI = 1000\text{kN.m}^2$. This E_iI value is chosen to represent modelling of a cable element that has a solid bar cross section with diameter $D = 100\text{mm}$. The third model represents beam elements with bending stiffness value $E_iI = 2200\text{kN.m}^2$. The value of bending stiffness here is chosen to represent that of a bundle with a certain cross-sectional configuration but with the same axial stiffness E_iA as other models (Area is the same as others). This highlights the effect of cable cross-section arrangement on the overall stiffness. The nonlinear modal analysis accounts for the geometric nonlinearity mentioned earlier in section 2.5.2. The natural frequencies for each model are shown in table 3.7 and a comparison between the results is depicted in figure 3.27.

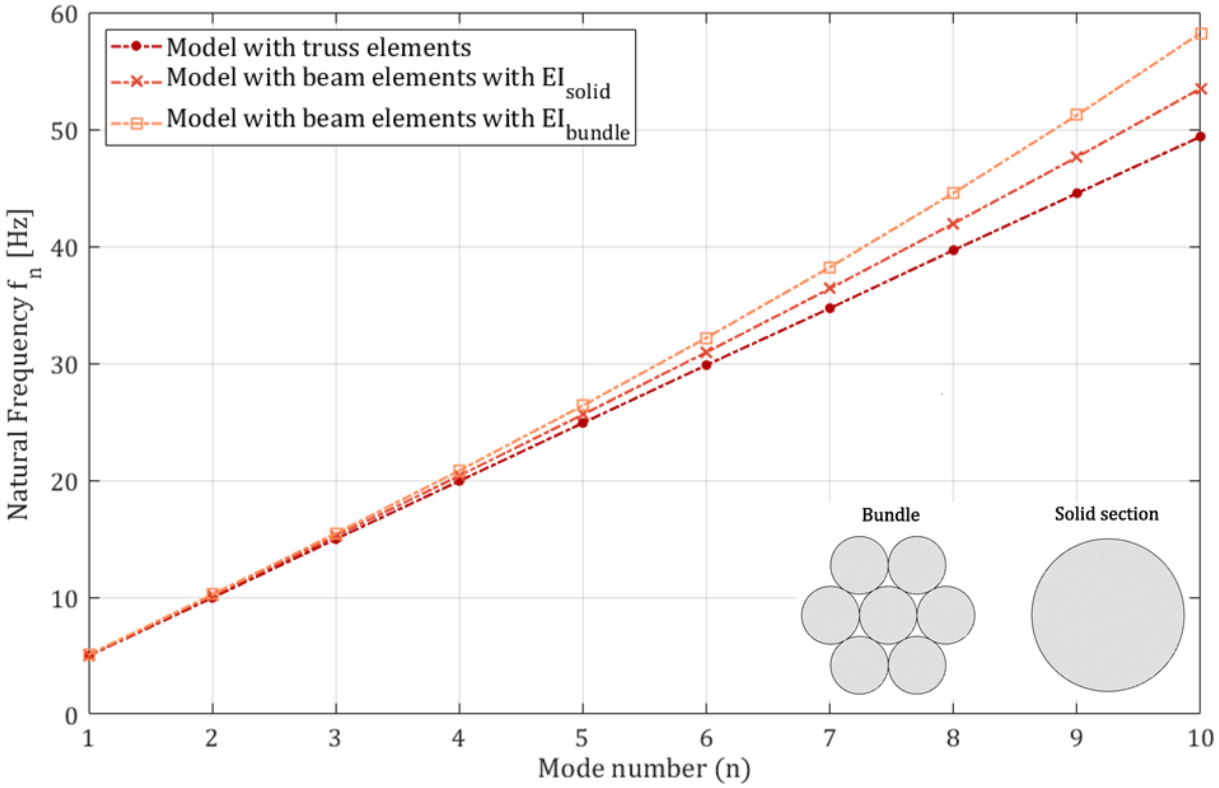

Figure 3.27: Modal analysis comparison between modelling with truss elements and modelling with beam elements.

Table 3.7: Modal analysis results of example depicted in figure 3.20

Mode Number	Natural frequency (EI=0) [Hz]	Natural frequency (EI≈ 1000kN.m^2) [Hz]	Natural frequency (EI≈ 2200kN.m^2)
1	4.98	5.05	5.09
2	9.95	10.12	10.23
3	14.97	15.23	15.46
4	19.94	20.39	20.83
5	24.90	25.62	26.39
6	29.85	30.95	32.18
7	34.71	36.39	38.22
8	39.67	41.95	44.56
9	44.54	47.64	51.22
10	49.38	53.5	58.24

All models have the same cross-sectional area.

The modal analysis results between models with truss element and models with beam elements have shown considerable differences. All models have the same cross-sectional area and differ only in their bending stiffness values. With higher bending stiffness value the natural frequencies tend to increase

in a convex shape with higher modes. This asserts the effect of bending stiffness on dynamic properties especially in cases with short cables. The methods of identification of cable force based on vibrations must account for bending stiffness effects to identify the nonlinearity of natural frequencies. Therefore, bending stiffness of cables is numerically investigated in the next chapter.

Chapter 4

Numerical Characterization of Bending Stiffness through the Transverse Component of Spring Elements

4.1 Introduction

Bending stiffness is the resistance of members against bending deformation. In the case of cables, bending stiffness effects are usually neglected and cables are assumed to be perfectly flexible [3]. The notion of perfectly flexible string is an idealization and may deviate from reality in case of short and stiff cables or external prestressing tendons. Actual strands do offer at least some resistance to bending and thus any realistic model must take this into account [20]. Section 2.4 highlighted the effect of bending stiffness on the natural frequencies. [21] reports that the bending stiffness of the cable contributes to a considerable effect on the natural frequencies of the overall suspension bridge system and affects vertical vibration modes more significantly than torsional ones. This serves as the motivation for investigating the bending stiffness behaviour of cables.

4.1.1 Steiner's Parallel Axis Theorem

The parallel axis theorem, also known as Steiner's theorem, is used to determine the second moment of area I of a rigid body about any axis, given the body's second moment of area about a parallel axis through the object's center of gravity I_i and the perpendicular distance between the axes z_i [22]. The thesis uses this theory to determine the second moment of area for a bundle of rods about the bundle's neutral axis. The term rod is used here to denote a slender three dimensional body that has a bending stiffness EI_i instead of the perfectly flexible wire. Figure 4.1 depicts a bundle of rods and highlights the parameters used to calculate the second moment of area I of the bundle as a whole, which is calculated as such:

$$I = \sum I_i + \sum A_i \cdot z_i^2 \tag{4.1}$$

where each rod has a second moment of area around its own axis I_i denoted by $I_i = \frac{\pi D^4}{64}$ with D being the rod diameter, distance to the neutral axis of the bundle z_i and an area A_i.

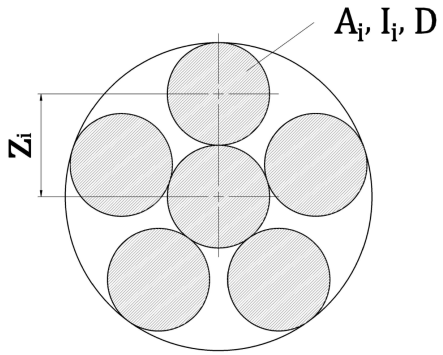

Figure 4.1: Parameters used to calculate the second moment of area I.

Equation (4.1) is valid for application on cables when the rods are in perfect contact or bonded i.e. no relative slippage, which is a reasonable assumption e.g. for Locked coil ropes (section 2.2.1). However, if the rods are in friction-less contact (rods' surfaces are 'perfectly smooth' or in no contact), the second moment of area is the sum of all individual second moments of area about the rods own neutral axis as such:

$$I = \sum I_i \tag{4.2}$$

4.1.2 Frictional Behaviour

Taking parallel wire cables as an example, the bundle in the span region connects the wires using separators, other cable technologies inject the bundle with grout waxing material [3]. This implies that the strands of such case are in frictional contact between one another, and in the context of the second moment of area, their I value is between that of a friction-less contact and that of a bonded case (equation (4.2) and equation (4.1)). This thesis hypothesizes that the second moment of area, which is a geometric property, can be exploited to include a frictional concept based on the contact behaviour of the rods.
The frictional effect is the result of the enormous complexity of the interactions between the surfaces of two solids [23]. This makes the calculation of friction impractical and necessitates the use of empirical methods for analysis. Computational aspects for modelling the interactions between many wires are very complex. Moreover, numerical modelling of frictional behaviour based on traditional contact algorithms is unfeasible as it requires extensive computational time and may not converge at all [13]. Therefore, a new approach is required to provide a practically simple yet effective modelling method to approximate key required frictional criteria that affects the bending stiffness behaviour.

A further generalization of Steiner's equation (4.1) presented by the author would be:

$$I = \sum I_i + c \sum A_i \cdot z_i^2 \tag{4.3}$$

c here refers to the contribution of the rods bundle as a whole. If $c = 1$ then the bundle of figure 4.1 is in perfect bond contact and I equals equation (4.1) which would be the upper bound value of the second moment of area, often referred to in the literature as I_{max} (the same abbreviation will be used in this thesis). If $c = 0$ then there would be friction-less contact (or no contact) and the second moment of area I would equal to equation (4.2). This value is the lower bound value of I and is referred to as I_{min}. The aim of this chapter is to derive a numerically-based method that can determine the value of c in an interval $[0, 1]$. This method is based on a numerical analysis that approximates frictional behaviour between wires by using the transverse component of springs (also referred to as shear springs). The method of using springs to approximate frictional behaviour is well-acknowledged among the literature. For example, [13] used elastic-perfectly plastic springs to model random wire breaks of parallel steel wires and the resulting nonlinear redistribution of stresses in the vicinity of the break as well as load transfer between wires due to friction.

4.2 Concept of Bending Stiffness Identification using Shear Springs

4.2.1 Bending stiffness Identification using Deformed Member Geometry

The loading of a cantilever beam under a constant bending moment M on the free end leads to a constant curvature κ as seen in figure 4.2. κ is related to the bending stiffness EI by the following equation:

$$\kappa = \frac{M}{EI} \tag{4.4}$$

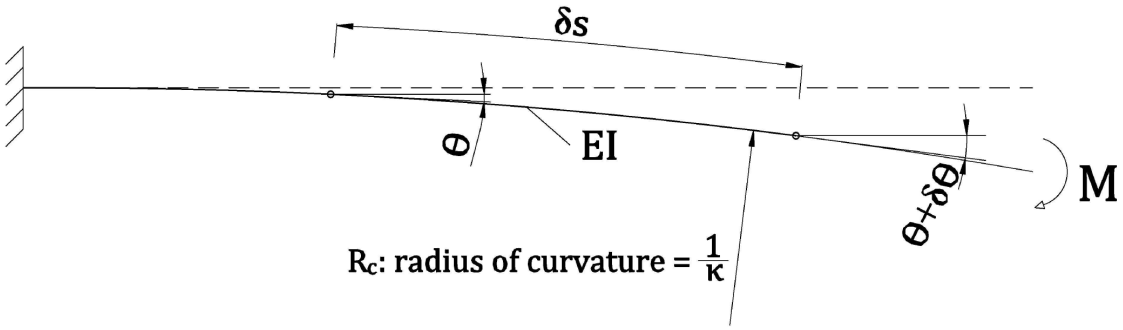

Figure 4.2: Schematic showing a cantilever beam under a constant bending moment M resulting in a constant curvature κ

Since the bending moment M is constant over the whole beam, the deformed shape of the cantilever follows a circular path (the curvature is constant). The rotations θ at any two nodes on the cantilever could be exploited to calculate the radius of curvature $R_c = \frac{1}{\kappa}$ by using the arc length equation as such:

$$R_c = \frac{1}{\kappa} = \frac{\delta s}{\delta \theta} \rightarrow \kappa = \frac{\delta \theta}{\delta s} \tag{4.5}$$

where δs equals the arc length between any two nodes and $\delta\theta$ equals the difference of the rotations at those two nodes. It is worthy of mentioning that the center of circular deformed shape lays on the same vertical axis of the fixed support since the rotation at that point is zero. By using equation (4.4) and equation (4.5) the bending stiffness could be calculated as follows:

$$EI = \frac{M}{\kappa} \tag{4.6}$$

The target here is identifying the second moment of area I_{idn}, and since no material nonlinearity is considered (E is constant), the final equation to be considered would be:

$$I_{idn} = \frac{M}{E \cdot \kappa} \tag{4.7}$$

4.2.2 Proposed Numerical Model to Identify the Second Moment of Area

Based on the aforementioned concept, a numerical model is set up to meet the case of a cantilever beam under a constant moment M as shown in figure 4.3. The model is described as two parallel beam elements with a diameter D and a length L_{spr} separated by a distance z_i. The bottom element is a fixed cantilever and the upper one is fixed rotationally and vertically and released horizontally. A bending moment M is applied at the center of a rigid element which connects the other end of the members. Each two facing rod nodes are connected along the span with a number of shear springs n_{spr} that have a stiffness K_T.

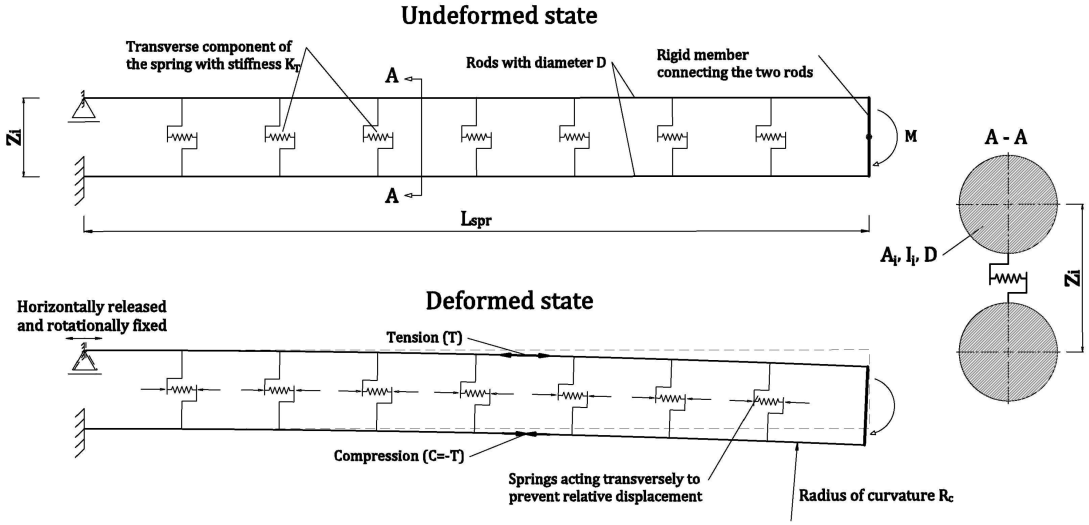

Figure 4.3: Proposed numerical model used to identify the bending stiffness.

In pure bending of, say a rectangular section, the axial force generated by the bending moment at the uppermost fiber evens out with its bottom counterpart. The main purpose of this model is to achieve this similarity as such: the shear springs would transmit the axial force in the upper rod to even out

with the bottom one and since only the upper rod is released horizontally but fixed rotationally, the bending would result in an even distribution of the moment M between the two rods (each taking $M/2$) as well as a relative displacement between the rods (only the upper rod translates horizontally). This relative displacement activates the shear springs, making it dependent on the number of springs n_{spr} and the spring stiffness K_T as seen in figure 4.4 thereby achieving the dependency of the curvature κ on shear springs. By increasing the springs stiffness K_T and their number n_{spr} the curvature would decrease which would result in identifying a larger bending stiffness and thus allowing the calculation for the corresponding second moment of inertia as described in equation (4.7). The following sections establish an example and discuss the findings based on values of the aforementioned parameters as shown in table 4.1.

Table 4.1: Used parameters for the numerical modelling to identify second moment of area.

Model parameters	Symbols used	Value assigned [unit]
Span length	L_{spr}	1 [m]
Distance between rods	z_i	5 [cm]
Rod diameter	D	2.5 [cm]
Identified second moment of area	I_{idn}	*to be identified* [cm^4]
Bending moment	M	2 [kN.m]
Modulus of elasticity	E	200 [GPa]
Number of shear springs	n_{spr}	*varying* [-]
Shear springs stiffness of	K_T	*varying* [kN/m]

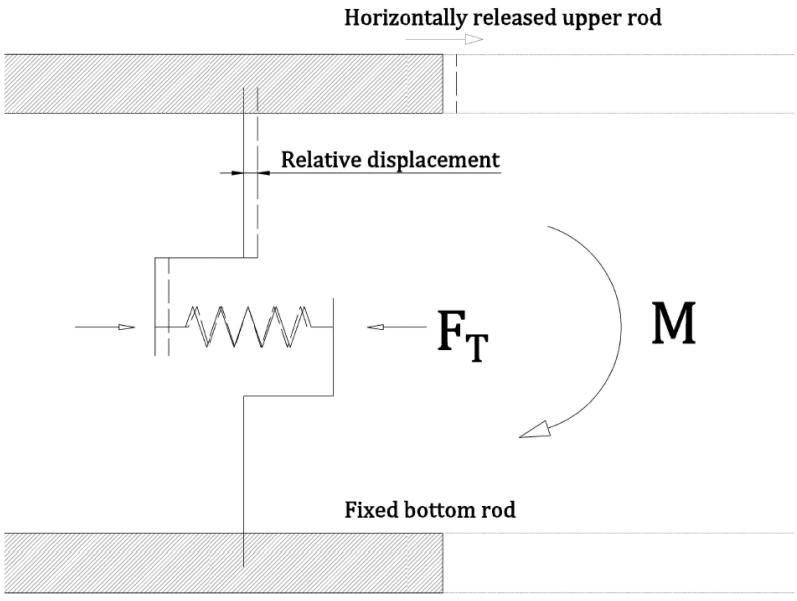

Figure 4.4: Schematic showing the activation of shear springs mechanism.

F_T is the spring force that resulted from the relative displacement

4.3 Numerical Utilization of Shear Springs to Identify Bending Stiffness

The proposed concept in section 4.2.2 is modeled to back-calculate the bending stiffness EI and henceforth the second moment of area I_{idn} under varying cases:

1. A number of elastic shear springs with varying stiffness K_T.
2. Varying number of elastic shear springs per unit length n_{spr}.
3. Elastic-perfectly plastic springs with varying yield force F_{Ti}.

In elastic-perfectly plastic shear springs case, the spring allows relative displacement or 'slippage' based on its stiffness until it reaches a certain force F_{T_i} and then would perfectly yield with zero stiffness K_T under that force to account for the slip behavior as illustrated in figure 4.6.

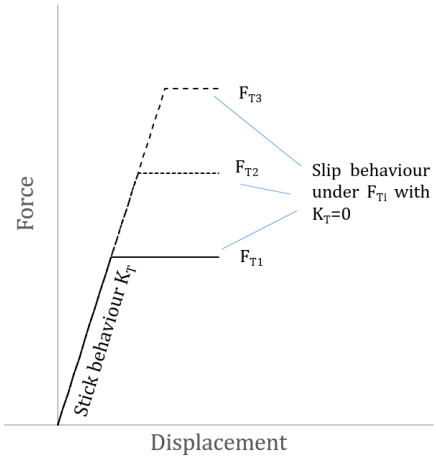

Figure 4.6: Stick/Slip behaviour as a function of nonlinear springs.

But before going through these cases, the model shall be validated. The validation is based on equation (4.1) and equation (4.2) as upper and lower bound values I_{max} and I_{min}. Fully bonded rods would achieve zero relative displacement and adhere to equation (4.1), which could be achieved by fixing the horizontal release of the upper rod in figure 4.3 and applying the bending moment M. This allows the back-calculation of the corresponding bending stiffness (or second moment of area I_{idn} as in equation (4.7)). Contact-less (or friction-less) rods would result in I_{min} value of equation (4.2), which could be achieved by releasing the horizontal component of the upper rod and bringing the shear springs' stiffness to null. The resulting I_{idn} shall be consistent with adding up each rod's individual I_i table 4.2.

Table 4.2: Comparison between identified second moment of area of the numerical model and Steiner's theorem.

	Theoretical I $[cm^4]$	Identified I_{idn} $[cm^4]$
Lower bound	$I_{min} = 3.834$	3.834
Upper bound	$I_{max} = 65.194$	65.395

Since the numerical analysis adheres to the upper and lower bound I_{max} and I_{min}, it would be most suitable now to study the effects of shear springs on the overall bending stiffness.

4.3.1 Elastic Shear Springs with Varying Stiffness K_T

Initially, an arbitrary number of springs is chosen to study the effect of varying shear springs stiffness K_T on the identified second moment of area I_{idn}. The number of springs chosen is $n_{spr} = 100$ distributed over a length of $L_{spr} = 1$m. Henceforth the number of springs n_{spr} will represent the number of springs distributed over a unit length. It can also be interpreted as 'spring density' as it refers to the number of springs per unit length of a member. As seen in figure 4.8a, increasing the shear springs stiffness K_T increases the identified second moment of area I_{idn} in a nonlinear path until surging at $K_T \approx 10^7$kN.m, which is referred to as a semi-rigid shear spring as springs provide very high stiffness. It is also noticeable that the maximum identified value of I_{idn} is noticeably less than I_{max} from equation (4.1). This requires studying higher and lower values of n_{spr} to underline the behaviour of elastic shear springs.

4.3.2 Varying Number of Elastic Shear Springs

By varying the number of springs n_{spr} a pattern arises (depicted in figure 4.9). For any number of springs, the identified second moment of area I_{spr} increases until surging at a certain value. This value is reached upon increasing the spring stiffness K_T until reaching 10^7kN/m and is directly dependent on the number of springs connecting the two rods laterally. This finding can be interpreted as such; increasing the number of springs increases the number of contact points between the two rods, i.e. it could be conceived as increasing the area in which the rods have contact with each other. Since the springs are linearly elastic, increasing the value of their stiffness K_T would decrease the relative displacement between the rods, this observation has a notable similarity with the behaviour of dry friction (the higher the surface roughness the less the relative displacement or the higher the sticking between the rods). This behaviour is depicted in figure 4.11.

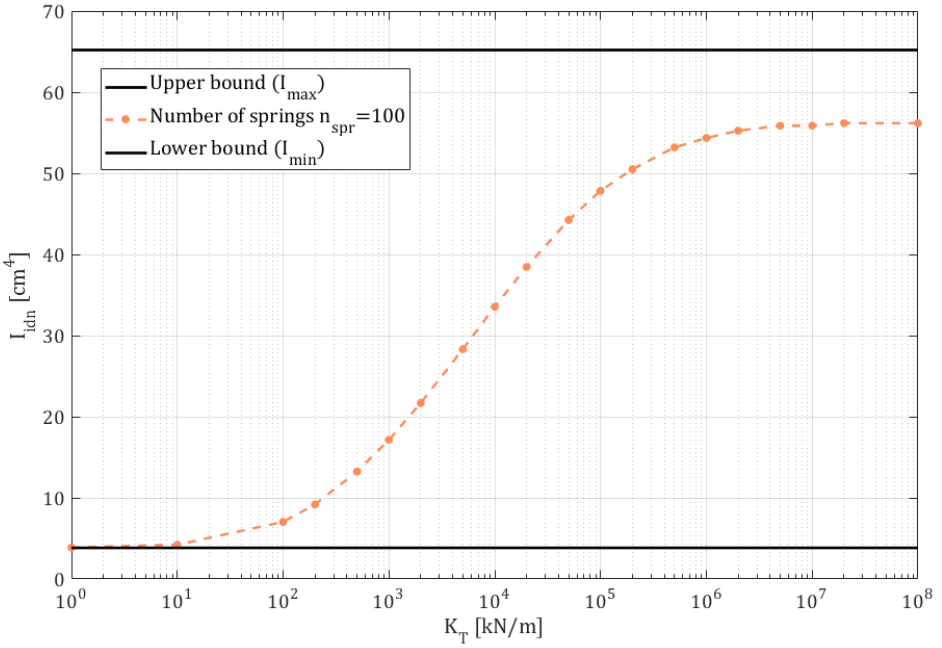

Figure 4.7: Effect of varying shear spring stiffness K_T on the identified second moment of area I_{idn}.

(a) Number of springs $n_{spr} = 100$ distributed over a length $L_{spr} = 1$m, or 100 springs/m. Semi-log plot for the horizontal axis of K_T

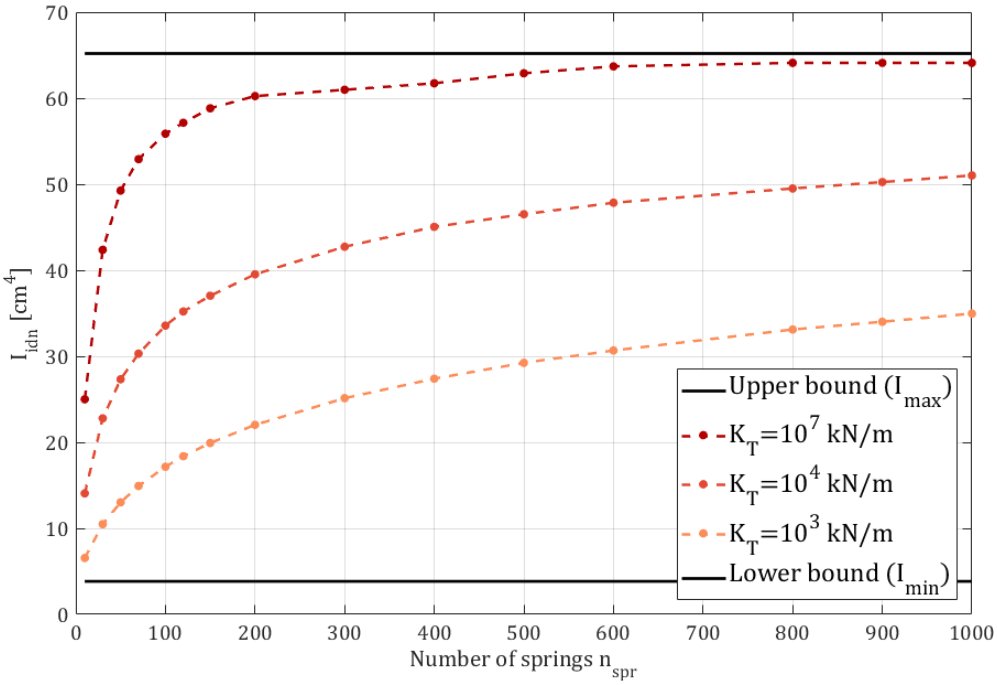

Figure 4.11: Effect of varying number of springs n_{spr} on the identified second moment of area I_{idn} for $K_T = 10^3, 10^4, 10^7(semi - rigid)$kN/m.

Increasing the number of springs per unit length is conceived as increasing contact points between the rods. The increase of K_T could be conceived as increasing the roughness between those contact points

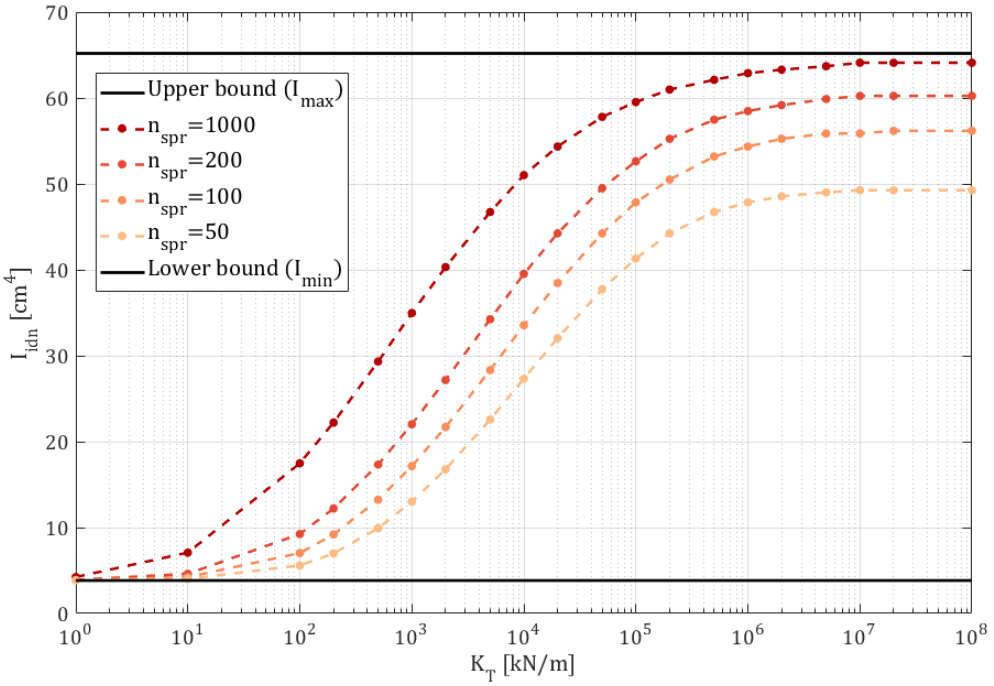

Figure 4.9: Effect of multiple numbers of springs n_{spr} [springs/m] on the identified second moment of area I_{idn}.

Semi-log plot for the horizontal axis of K_T

By a combined increase of the number of springs n_{spr} and their stiffness K_T the identified value of I_{idn} converges to but does not exceed the upper bound value of the second moment of area I_{max} of equation (4.1). This finding can also validate the concept of the numerical model. In basic terms, more contact points and more resistance to relative displacement result in convergence towards a full-contact but does not exceed it. The ability to control and quantify the bending stiffness between upper and lower bounds EI_{max} and EI_{min} using this method applies to most similar cases. Figure 4.13 summarizes the effect of using a number of very stiff shear springs n_{spr} on the identified second moment of area I_{idn}.

Here it is important to recapitulate equation (4.3) that deals with the second moment of area of rods around their own axis I_i, their individual cross sectional area A_i, each rods distance from its neutral axis to the bundle's neutral axis z_i and the contribution ratio c; previously described as the contribution ratio of a bundle of rods as whole to the overall second moment of area I ($c = 0$ means contact-less rods and $c = 1$ means rods in full contact). The equation goes as such:

$$I = \sum I_i + c \sum A_i \cdot z_i^2$$

If the aforementioned findings regarding I_{idn} are to be exploited to calculate c, and with the reasonable

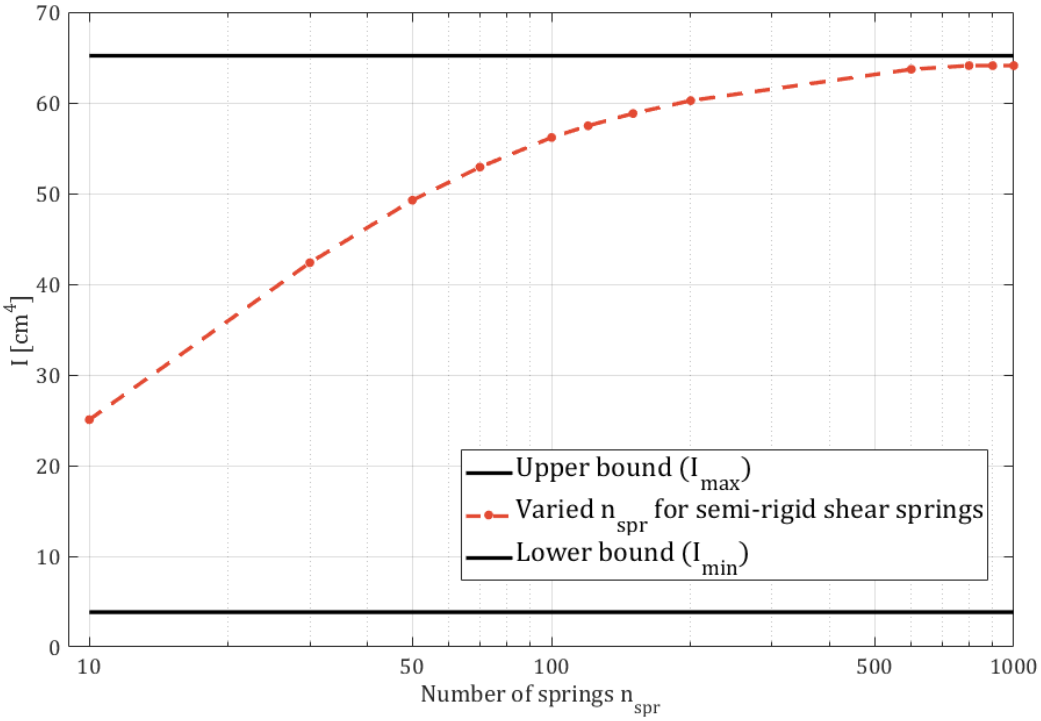

Figure 4.13: Maximum identified values of I_{idn} for varying number of semi-rigid springs ($K_T \geq 10^7$kN/m).

The number of springs n_{spr} can be conceived as the spring density or the number of springs per unit length [springs/m].

assumption of $I \approx I_{idn}$, c could be quantified as:

$$c = \frac{I_{idn} - \sum I_i}{\sum A_i \cdot z_i^2} \tag{4.8}$$

As an example, quantifying c by equation (4.8) from figure 4.13 would result in figure 4.15. The quantification of c for any case makes it allowable to assign the corresponding bending stiffness EI_{idn} to any cable by basic insertion of the corresponding second moment of area value. This will be the cornerstone of the next chapter. Table 4.3 shows the identified contribution ratio c obtained from each number of springs n_{spr}.

Table 4.3: Identified contribution ratio c for a number of springs n_{spr}.

n_{spr} [springs/m]	Contribution ratio c
30	0.628
50	0.740
100	0.853
200	0.919
500	0.962
1000	0.982

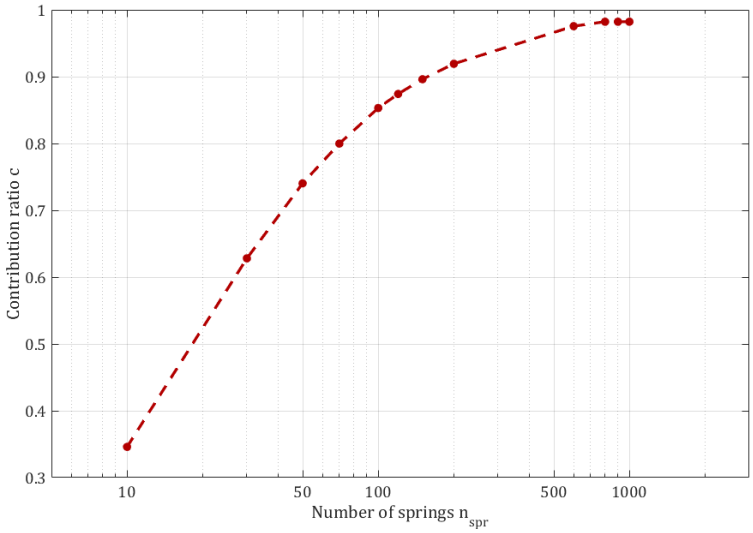

Figure 4.15: Identified contribution ratio c of equation (4.3) for multiple numbers of semi-rigid springs.

Number of springs n_{spr} can be conceived as the spring density, or the number of springs per unit length [springs/m].

4.3.3 Effect of Assigning Nonlinear Shear Springs

Stick/slip behaviour is utilized with the usage of elastic-perfectly plastic springs (depicted in figure 4.6). The springs provide resistance to the relative displacement utilized by the stiffness K_T until reaching their yield force F_T, then the displacement increases with no increase in force (since $K_T = 0$) hence the name 'perfectly plastic'. The behaviour of the identified second moment of area as a function of yield force F_T is that of a concave shape. I_{idn} would increase until converging to that value of elastic springs model. This is a consequence of none of the springs reaching its assigned yield force.

Commentary on the Definition of Yield Force to Shear Springs

Generally, the relative slip is a function of the force acting perpendicularly on the slip surface. Coulomb friction approximates the force causing the slip behaviour as such:

$$F_f > \mu F_n \tag{4.9}$$

where F_f is the force causing the slip, μ is the coefficient of friction, which is an empirical property of contacting materials that represent their surface friction, and F_n being the force perpendicular (or normal) to the surface [24]. In this section, F_f (namely the yield force) is assumed as a cohesion force F_T that yields the springs as mentioned in section 2.5.2. This assumption is decided upon here in this section for the lack of normal force on the springs as the model is subjected to pure bending moment generating zero longitudinal force on the springs. Chapter 6 discusses the friction coefficient μ and its effect on the behaviour of springs and the overall deformation.

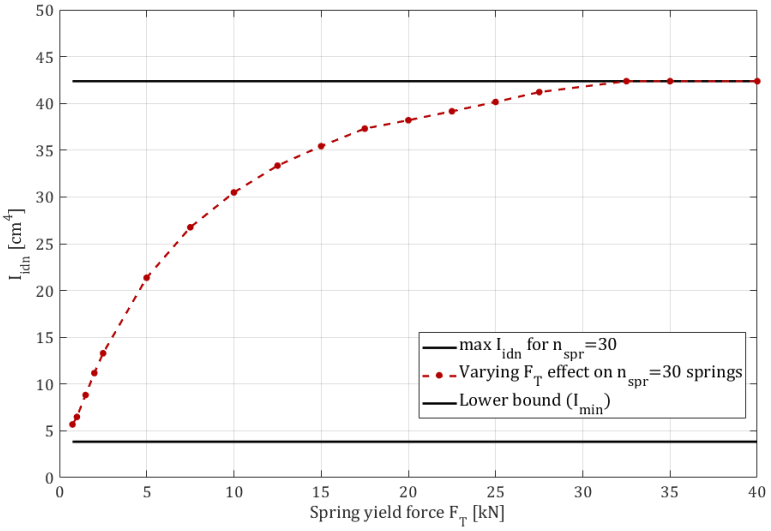

Figure 4.17: Effect of nonlinear springs on the identified second moment of area I_{idn}.

Upper bound value is obtained from figure 4.13 for a number of springs $n_spr = 30$ [springs/m]

The implication of assigning yield force for the springs in light of second moment of area is illustrated in figure 4.17. The figure illustrates assigning a a single yield force value F_T to all springs. This could reflect on the nonlinear springs behaviour in the case of this example (pure bending moment). But it can be the case, however, that assigning a frictional coefficient as in equation (4.9) on which the springs would result in deviation from merely assigning a value of yield force. The former is a more accurate description as the yield force vary according to the loading case.

Chapter 5

Implementing Transverse Spring Elements as Connections between Cable Rods on a Proposed Extradosed Bridge Geometry

5.1 Introduction

In chapter 4, the connection between modeled rods subjected to pure bending moment is described as a function of number of transverse (or shear) springs distributed over a unit length n_{spr} and the spring transverse stiffness K_T. The chapter proposed a description of bending stiffness behaviour in the region between friction-less contact and total contact between two modeled rods.

In this chapter, the same modelling technique is applied on a three parallel rod cable resting on the saddle geometry proposed in section 3.2. The three rods' centerlines are separated from each other with a distance equaling their assigned diameter D so they can be accounted as on top of each other. During the analysis, their spacing between each other (equaling their diameter D) is preserved using the axial component of the springs that are assigned with a very high stiffness K_P in their principle direction. The setup is illustrated in the schematic of figure 5.1. The saddle is also represented by radial compression-only longitudinal semi-rigid springs as mentioned in section 3.2.1.

This chapter investigates the validity of shear springs as connections between rods to verify their ability to represent the bending stiffness behaviour in a more realistic loading case. To methodologically reach this aim, the proposed model requires an anchor to another rigorous model to validate and compare the results. Validation efforts made on the previously described numerical model in section 3.3 showed satisfactory results with low error values when comparing the deformations of the numerical model to the analytical catenary solution (highest error value =0.23%). Since the validated numerical model meets the same geometry as required in this chapter, it will be used to compare the results and observe the changes occurring as a result of altering the parameters describing the three rod shear springs model. The model described in section 3.2 will be named the 'main' model throughout this chapter and the three rod shear springs model will be referred to as the TRS model.

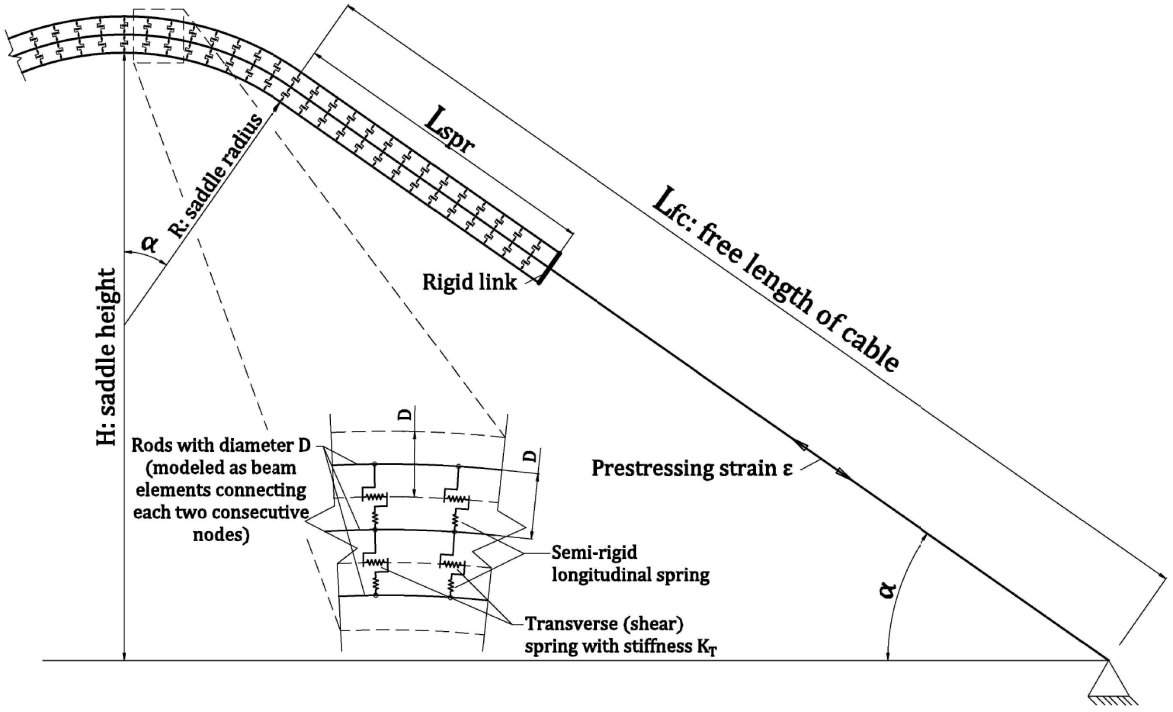

Figure 5.1: Schematic showing the modelling technique used in the three rod shear springs model (TRS).

Emphasis on: L_{spr}: Free length of rods connected with springs not resting on the saddle geometry, n_{spr}: number of springs per unit length [springs/m] and K_T: transverse stiffness of springs

The question here would be as such, how can the validated 'main' model, which is composed of one cable following a certain geometry, be compared to another one that is based on not one, nor two, but three rods connected using shear springs? To answer this question, it might be more precise to break it down into more specific inquiries and provide a careful answer to each as such:

- 'The two models have different cross sections, how would they be compared to each other?' The comparison will be made on the overall deformed shape based on the models' matching centerlines, since they follow the same geometry.
- 'The 'main' model is assigned with a diameter D and the other rods have separate Ds': D is assigned to the rods and based on their corresponding total area $A = \sum A_i$ the 'main' model is assigned with that cross-sectional area value i.e. the 'main' model has the same total area as the sum of three rods area, thereby providing the same axial stiffness $E_i A$.
- 'The 'main' model is validated using truss elements that have zero bending stiffness, here the model is to be assigned with beam elements instead!': Cables and tendons (especially short ones) being modeled with beam elements provide a more accurate description of cable behaviour as the bending stiffness effects are not neglected as with a usual truss elements model (see [25]

and [26]) and since the 'main' model is validated using truss elements with the catenary solution, assigning it with beam elements with a bending stiffness value will be compared to the three rod model with an equivalent bending stiffness value, meaning that the 'main' model will be used as an anchor to the validity of the three rod shear springs (TRS) model.

- 'The definition of the bending stiffness of the 'main' model to meet the corresponding value in TRS model is vaguely defined!': Equation (4.3), figure 4.15 and table 4.3 define the way the contribution ratio c is assigned to the second moment of area value I. So assigning a certain number of springs to the TRS model n_{spr} would correspond to assigning a c value to equation (4.8) and calculate the value of the identified second moment of area I_{idn}, which is then assigned to the 'main' model.

- 'The schematic of figure 5.1 shows the free length of rods L_{spr} and total free length of the cable L_{fc}, how can the member with length $L_{fc} - L_{spr}$ be defined?' Its cross-sectional area A will be defined as the sum of the rods cross sectional area $A = \sum A_i$ and its second moment of area value will be assigned according to equation (4.8) ($I = \sum I_i + c \cdot \sum A_i \cdot z_i^2$) where I_i is the second moment of area for an individual rod, c is dependent on the number of springs per unit length for semi-rigid shear springs, and z_i being the perpendicular distance to the rods neutral axis, which equals the rod diameter D.

- 'How the three rods with a free length of L_{spr} are connected with the remainder to the cable that of a length $L_{fc} - L_{spr}$' They are connected using a very stiff beam element that translates the loads via its substantial bending stiffness. It can be considered as a rigid link that is quasi-undeformable (see figure 5.1).

The TRS model is compared with 'main' model under various changing parameters; different free length of rods with connecting springs L_{spr}, multiple numbers of springs per unit length n_{spr}, low prestressing values represented as strain values ε, nonlinear behaviour of transverse springs utilized by frictional coefficients μ, and under various spring stiffness K_T. The analysis conducted is a third order nonlinear analysis to account for both spring nonlinearity (elastic-perfectly plastic springs) as well the geometric nonlinearity of big deformations. The used parameters that are assigned to the model are summarized in table 5.1.

The prestressing henceforth will be referred to as a ratio of ε_o. For example, a frequently used prestressing value in this chapter is $0.5 \cdot \varepsilon_o = 4.425‰$. The similarities between the 'main' model and the TRS model are visualized by plotting the deformed shapes from each model together along with their differential deformation (to visually account the differences). To quantify and measure the similarity between the two models, statistical operations are performed on the deformed shape for each solution such as the sum of deflections for each model as well as the differences between them (e.g. a low sum of differentials refers to a high correlation). This provides a vigorous quantification of the error between them since the notion of their deformation differences is a valid suspicion due to different model setups. The maximum value of the differential deformation is also quantified and mentioned in the plots.

Table 5.1: Parameters used in the numerical models.

Parameter	Symbol used	Value assigned [unit]
Rod diameter	D	100 [mm]
Saddle height	H	10 [m]
Inclination angle	α	35 [°]
Saddle Radius	R	8 [m]
Modulus of Elasticity	E_e	200 [GPa]
Ultimate stress	σ_u	1770 [MPa]
Reference prestressing strain	ε_o	$\frac{\sigma_u}{E_e} = 8.85$ [‰]
Free length of cable	L_{fc}	16.17 [m]
Free length of rods with connecting springs	L_{spr}	*varying* [m]
Number of springs per unit length	n_{spr}	*varying* [springs/m]
Shear springs stiffness	K_T	*varying* [kN/m]
Frictional coefficient	μ	*varying* [-]

5.2 Comparison of the Effects of the Different Parameters on the TRS Model

5.2.1 Comparison Methodology

As described, the three rod shear model (TRS) is governed by many factors that require comparison to the 'main' model of section 3.2. Firstly, the rods are extended out of the saddle with a length L_{spr}, that is presumed to have an effect on the overall deformed shape. Secondly, the rods are connected with shear springs, which have a quantity per unit length n_{spr} and stiffness K_T (could also be nonlinear) that would result in varying bending stiffness as aforementioned. And thirdly, the prestressing strain can vary, which makes the models highly worthy of studying under low prestressing values. The comparison is decided upon to be as such:

- An investigation on the effect of the extended length of rods with connecting springs L_{spr} and settling on a satisfying value that can adequately represent the other effects. Varying the length L_{spr} would vary the region under which the resulting bending moment from self-weight is applied and also affect the number of nodes, hence the total number of springs (it is not to be confused with the number of springs per unit length n_{spr}).
- A study on the effect of the number of springs per unit length n_{spr}. This effect has a direct relation to the overall second moment of area (i.e. the bending stiffness) described in the previous chapter. A corresponding second moment of area I value will be assigned to the main model based on the selected n_{spr} in the TRS model as shown in table 4.3.
- Examining the effects of varying the linear transverse stiffness K_T of springs on the deformations, which also have a direct effect on the bending stiffness as described in chapter 4.
- Varying the prestressing value would vary the effective modulus of elasticity E_i, especially for low values of prestressing, which would have a direct effect on the sagging of the cables. Therefore low prestressing values are studied and compared.

- A study on assigning the semi-rigid springs ($K_T \geq 10^7$ kN/m) with an elastic-perfectly plastic stiffness that is utilized using the frictional coefficient μ. The springs would show a perfectly plastic behaviour ($K_T = 0$) when the transverse force component F_T reaches a frictional coefficient μ times the principle component of spring force F_P (yielding occurs when $F_T \geq \mu \cdot F_P$)

5.2.2 TRS Model with Various Lengths of Connecting Springs

The effect of the free length has its effect on utilizing the transverse springs at the rotation regions (rotation here hints at a probable relative displacement). From a previous observation on the main model, and a priori knowledge of pinned end structures, it is known that the biggest of rotations occur roughly on the first third from each pinned end (for example in simply supported beam case), thus it is centrally relevant to acquire a sufficient length L_{spr} to represent those effects. A trade-off between extended lengths and the computational cost is required for the efficiency of the models since computational cost is directly affected by number of nodes, hence number of springs n_{spr}. Different lengths are studied and the results are shown from figure 5.3 to figure 5.9. Table 5.2 shows the details of both numerical models.

Table 5.2: Numerical model parameter of TRS model for different lengths of rods with connecting springs L_{spr}

L_{spr} [m]	Max. deflec. TRS [mm]	Max. deflec. main [m]	max. diff. [mm]	No. nodes (TRS)	Solution time [sec]	Gen. Time [sec]
4	22.05	23.47	1.59	3879	29	25
6	22.01	23.47	1.77	5065	31	27
8	21.73	23.47	2.18	6279	33	48
15	≈ 20	23.47	3.51	10423	41	59

Shear springs used: semi rigid springs. Number of springs per unit length for all above models $n_{spr} = 100$ *springs/m. Gen. time refers to the amount of time required to formulate and export the geometry. Residuals for all above models*≈ 0

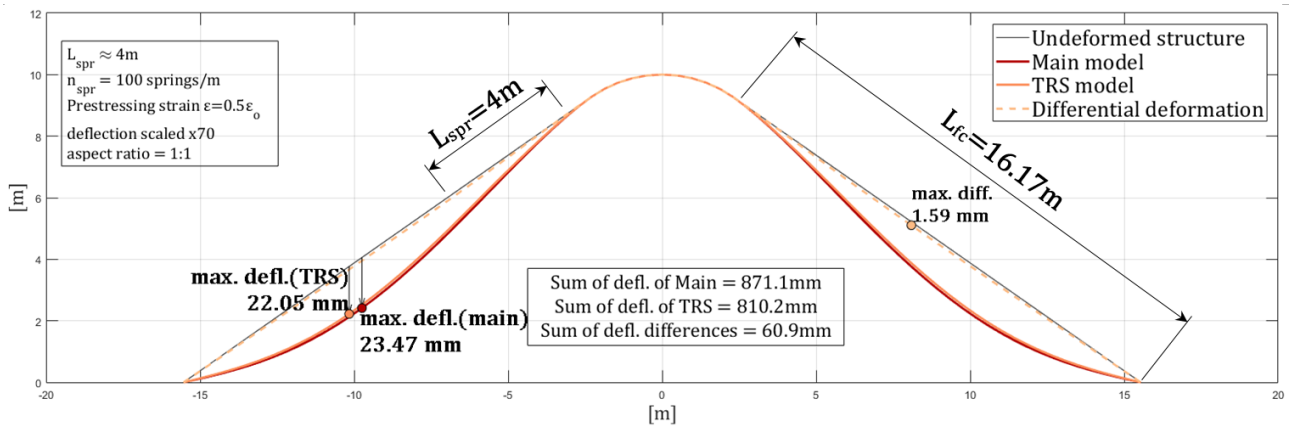

Figure 5.3: Comparison between the deformed shapes of TRS model and 'main' model for an extended length of connecting rods $L_{spr} = 4$m.

Number of springs assigned $n_{spr} = 100$ springs/m, $\varepsilon = 4.425‰$, $L_{spr} = 4$m approximates 0.25 of the total free length $L_{fc} = 16.17$m

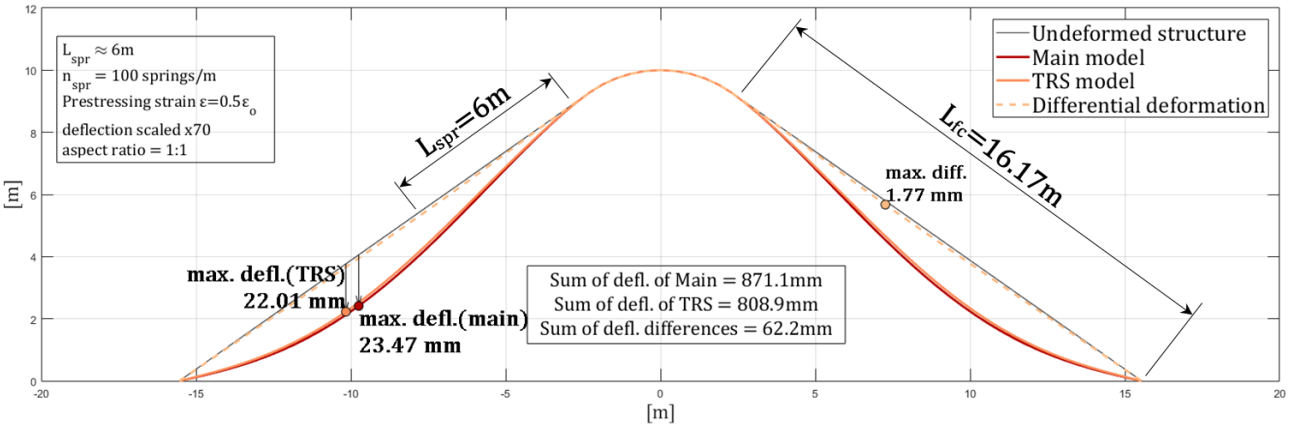

Figure 5.5: Comparison between the deformed shapes of TRS model and 'main' model for an extended length of connecting rods $L_{spr} = 6$m.

Number of springs assigned $n_{spr} = 100$ springs/m, $\varepsilon = 4.425‰$, $L_{spr} = 8$m approximates 0.375 of the total free length $L_{fc} = 16.17$m

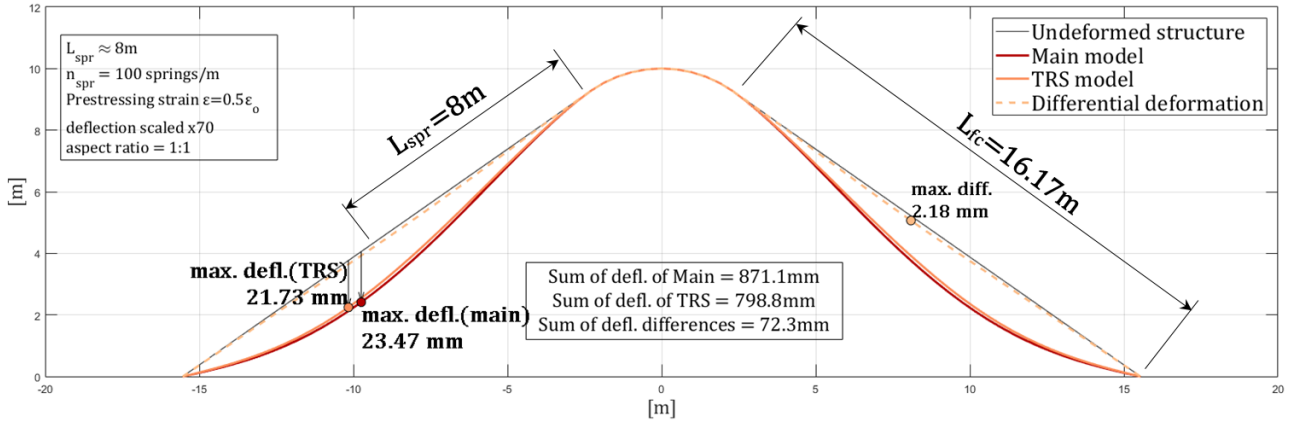

Figure 5.7: Comparison between the deformed shapes of TRS model and 'main' model for an extended length of connecting rods $L_{spr} = 8$m.

Number of springs assigned $n_{spr} = 100$ springs/m, $\varepsilon = 4.425‰$, $L_{spr} = 8$m approximates 0.5 of the total free length $L_{fc} = 16.17$m

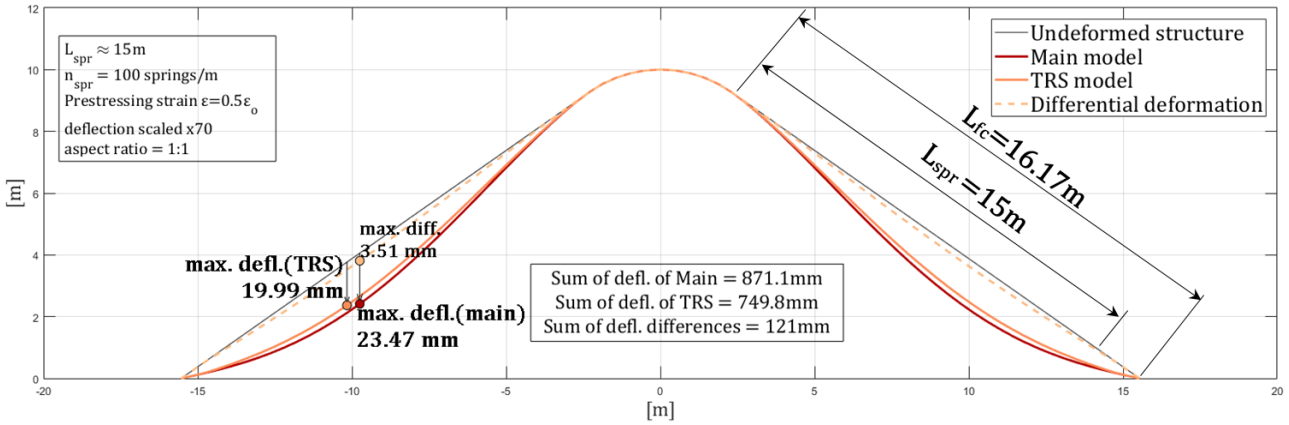

Figure 5.9: Comparison between the deformed shapes of TRS model and 'main' model for an extended length of connecting rods $L_{spr} = 15$m.

Number of springs assigned $n_{spr} = 100$ springs/m, $\varepsilon = 4.425‰$, $L_{spr} = 15$m approximates 0.93 of the total free length $L_{fc} = 16.17$m

The figures show high similarity in their deflected shapes and the general pattern would be that all of the TRS models proved to deflect slightly less than the 'main' model. This becomes clearer with increasing L_{spr} which refers to a higher overall stiffness. Error values are $6.9\%, 7\%, 8.2\%$ and 13.8% for $L_{spr} = 4, 8, 6$, and 15m respectively. The error is calculated by dividing the sum of differences between the models by the sum of the main model deflections. The error values indicate noticeable variation between the models as a result of the 'more stiff' TRS model, especially as the length on which the shear springs are distributed L_{spr} increases, and a probable uncertainty regarding the calculation of the c value of the proposed second moment of area I_{idn}. Still the error is not substantially high for $L_{spr} = 4$m, 6m and 8m. Therefore a value of $L_{spr} = 8$m is selected to conduct other investigations

of the TRS model since the length is almost half the total length of the free cable L_{fc}, thus would manifest the other properties of the TRS model in a clearer way. Even though results of $L_{spr} = 15$m showed high error values, it is nevertheless used to investigate the nonlinear behaviour of springs since it has the longest L_{spr}, hence the most overall number of springs out of the two other models.

5.2.3 TRS Model with Varying Number of Springs

After settling on a $L_{spr} = 8$m. The number of springs per unit length n_{spr} is studied for values of 100 and 200 springs/m. The latter showed lowest error values with error=5.48% but it is also highest in terms of computational costs (generation time and number of iterations). Thus the value of $n_{spr} = 100$ springs/m is settled upon for further comparisons as the error value remains 8.2%. The results are depicted in figure 5.11 and figure 5.13. Details about the analysis are described in table 5.3

Table 5.3: Numerical model parameter of TRS model for different number of springs per unit length n_{spr}

n_{spr} [springs/m]	Contribution ratio c	Max. deflec. TRS [mm]	Max. deflec. main [mm]	max. diff. [mm]	No. Nodes	Solution time [sec]	Gen. time [sec]
100	0.853	21.73	23.47	2.1	6283	40	36.8
200	0.919	21.95	20.89	1.39	12479	62	66.8

Number of nodes for $n_{spr} = 200$ springs/m is higher (almost twice as high as $n_{spr} = 100$ springs/m), thus it takes more solution time and more geometry generation time. Shear springs used: semi rigid springs. Gen. time refers to the amount of time required to formulate and export the geometry. Residuals for all above models≈ 0

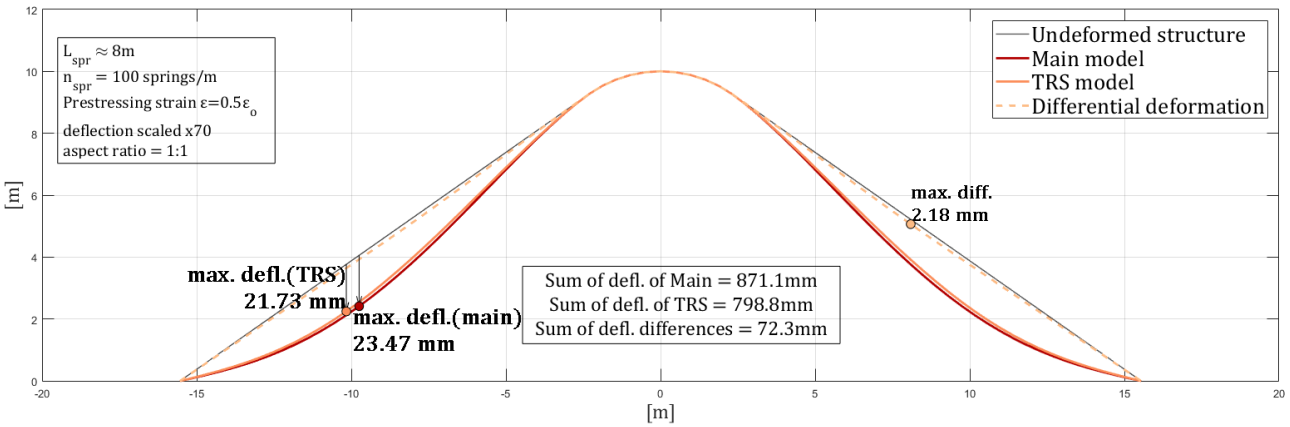

Figure 5.11: Comparison between the deformed shapes of the TRS model and the 'main' model for a number of springs $n_{spr} = 100$ springs/m.

$L_{spr} = 8$m with semi-rigid shear springs and $\varepsilon = 4.425‰$

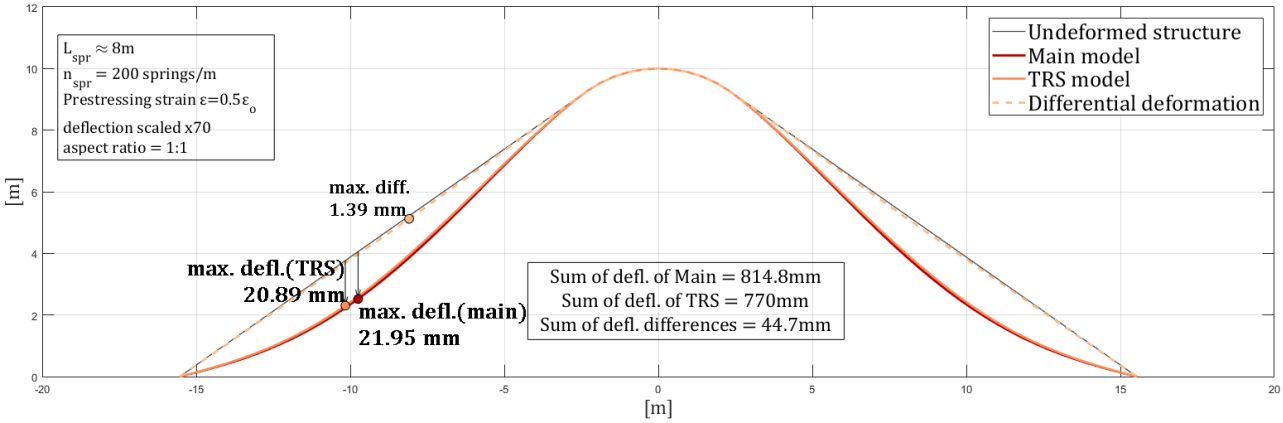

Figure 5.13: Comparison between the deformed shapes of the TRS model and the 'main' model for a number of springs $n_{spr} = 200$ springs/m.

$L_{spr} = 8$m with semi-rigid shear springs and $\varepsilon = 4.425‰$

5.2.4 TRS Model with Varying Transverse Spring Stiffness

With a L_{spr} value of 8m and n_{spr} of 100 springs/m, the effect of transverse stiffness of the springs K_T is studied to verify the choice of a very high stiffness value. During this study, the reason for the considerable discrepancy mentioned in **??** is discovered. The TRS model seems to be calibrated to the main model with $K_T = 10^5$kN/m, which provided an error of 0.47%. The exact reason is not well recognized, it is most probably to be a consequence of the uncertainty of the determination of the contribution factor c as it requires a more thorough study. From this section, it can be concluded that the higher the K_T value the higher the correlation to the main model since K_T represents a higher 'sticking' behaviour until a certain value, on which the TRS model calibrates itself. The TRS model for a higher K_T get more stiff and deflect less than the main model. The figures below (from figure 5.15 to figure 5.19) illustrate the description. Further details on the numerical model is outlined in table 5.4.

Table 5.4: Numerical model parameter of TRS model for different linear transverse spring stiffness K_T

K_T [kN/m]	Max. deflec. TRS [mm]	Max. deflec. main [mm]	max. diff. [mm]	No. Nodes	Solution time [sec]	Max. residual [kN]	Gene. time [sec]
0	81.98	23.47	- 61.1	6257	32	1.75	36.8
10^3	39.97	23.47	- 18.1	6257	25	1	36.8
10^5	23.19	23.47	0.525	6257	32	0.2	36.8
$\geq 10^7$	21.73	23.47	2.18	6257	26	0	36.8

For all models: $n_{spr} = 100$ springs/m, $L_{spr} = 8$m and $\varepsilon = 4.425‰$. *Gen. time refers to the amount of time required to formulate and export the geometry. Solution time refers to the time required to conduct the analysis with stated above residuals*

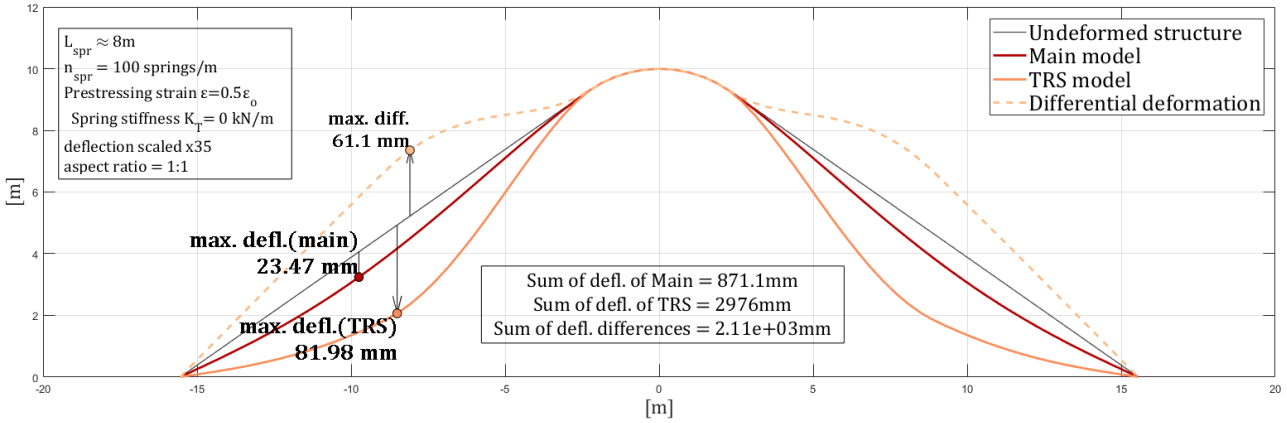

Figure 5.15: Comparison between the deformed shapes of the TRS model and the 'main' model for shear spring stiffness of $K_T = 0$.

$L_{spr} = 8\text{m}$, $n_{spr} = 100$ springs/m and $\varepsilon = 4.425‰$

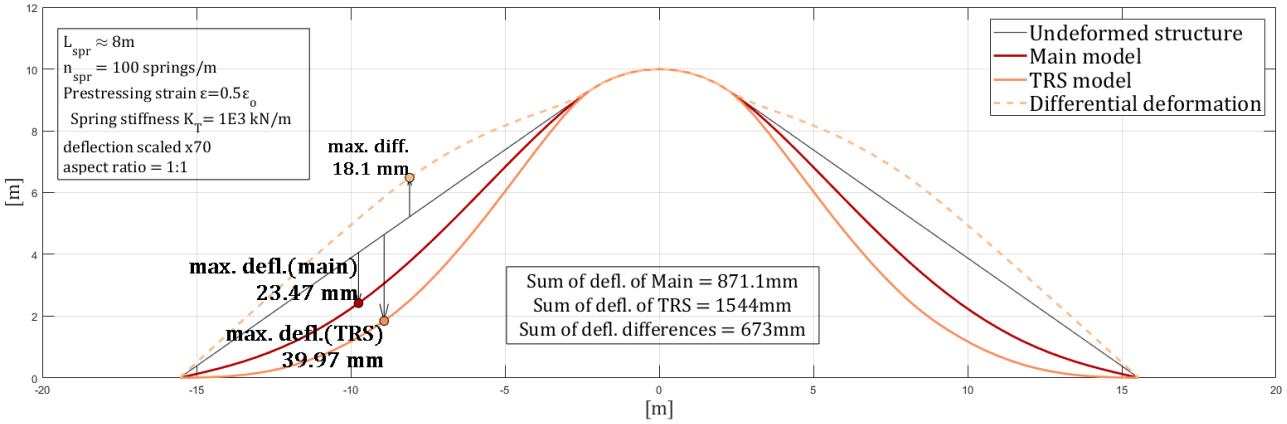

Figure 5.17: Comparison between the deformed shapes of the TRS model and the 'main' model for shear spring stiffness of $K_T = 10^3\text{kN/m}$.

$L_{spr} = 8\text{m}$, $n_{spr} = 100$ springs/m and $\varepsilon = 4.425‰$

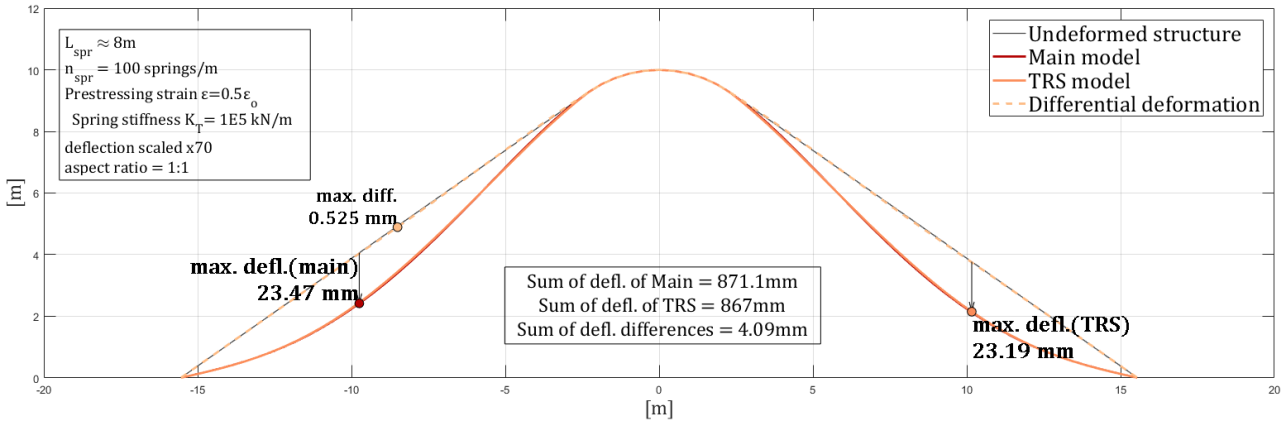

Figure 5.19: Comparison between the deformed shapes of the TRS model and the 'main' model for shear spring stiffness of $K_T = 10^5$kN/m.

$L_{spr} = 8$m, $n_{spr} = 100$ springs/m and $\varepsilon = 4.425‰$

5.2.5 TRS Model under Low Prestressing

The study of low prestressing values is essential to verify the model under high deformation as cables sag more when prestressing value is decreased. This occurs due to the lessened favorable secondary moment originating from prestressing force as well as lower effective modulus of elasticity E_i (mentioned in section 2.3.2). The modulus of elasticity is calculated as in Ernst equation (equation (2.6)) and assigned to both models. L_{spr} and n_{spr} are maintained to be 8m and 100 springs/m. The prestress value, as previously explained, is described as a percentage of ratio between the maximum stress value σ_u and the modulus of elasticity E_e defined as the strain value ε_o. The error value for all models showed a constant value of $\approx 8\%$ for all models, which is what is expected when all other properties and parameters are maintained constant. This provides an intuition that the TRS model is not affected by the prestressing parameters when compared to the main model.

Table 5.5: Model parameter of shear springs model for low prestressing levels

Prestressing strain $[\cdot\varepsilon_o]$	Max. deflec. TRS [mm]	Max. deflec. Main [mm]	max. diff. [mm]	E_i [GPa]	No. Nodes	Solution Time [sec]
0.02	30.34	32.65	2.93	142	6257	23
0.05	22.22	23.94	2.16	195	6257	21
0.1	21.73	23.43	2.12	200	6257	23

For all models $n_{spr} = 100$ springs/m, $L_{spr} = 8$m and $K_T \geq 10^7$kN/m. $\varepsilon_0 = 8.85‰$ *Geometry generation time*≈ 37*sec Solution. time refers to the time required to conduct the analysis with residuals*≈ 0

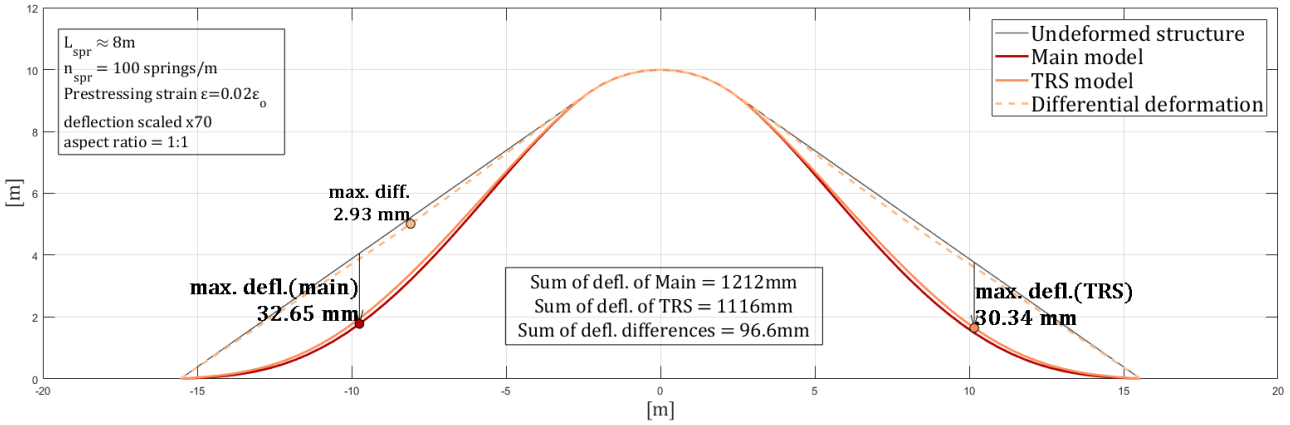

Figure 5.21: Comparison between the deformed shapes of the TRS and the main model for $\varepsilon = 0.02 \cdot \varepsilon_o$.

$L_{spr} = 8\text{m}$, $n_{spr} = 100$ springs/m, and $K_T \geq 10^7 \text{kN/m}$

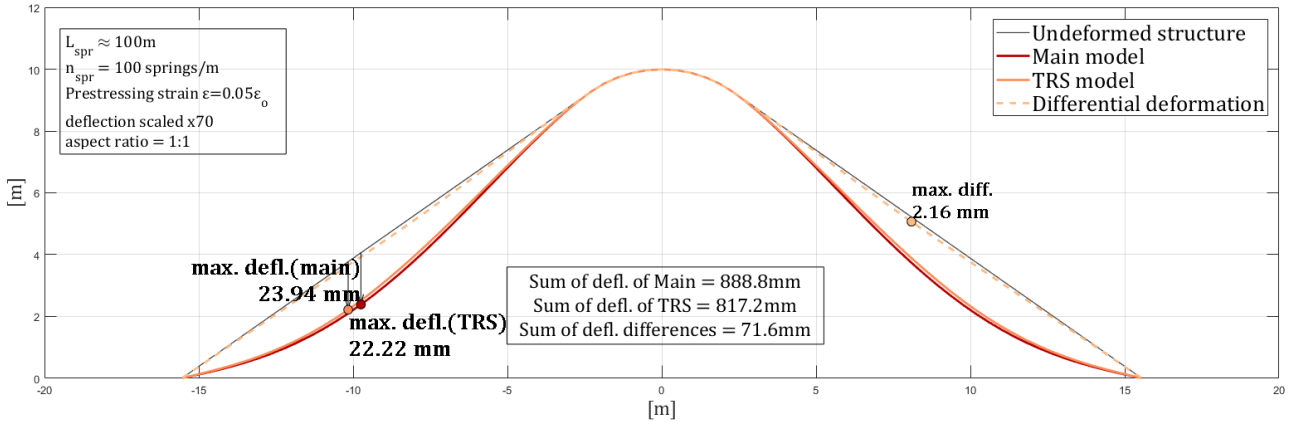

Figure 5.23: Comparison between the deformed shapes of the TRS and the main model for $\varepsilon = 0.05 \cdot \varepsilon_o$.

$L_{spr} = 8\text{m}$, $n_{spr} = 100$ springs/m, and $K_T \geq 10^7 \text{kN/m}$

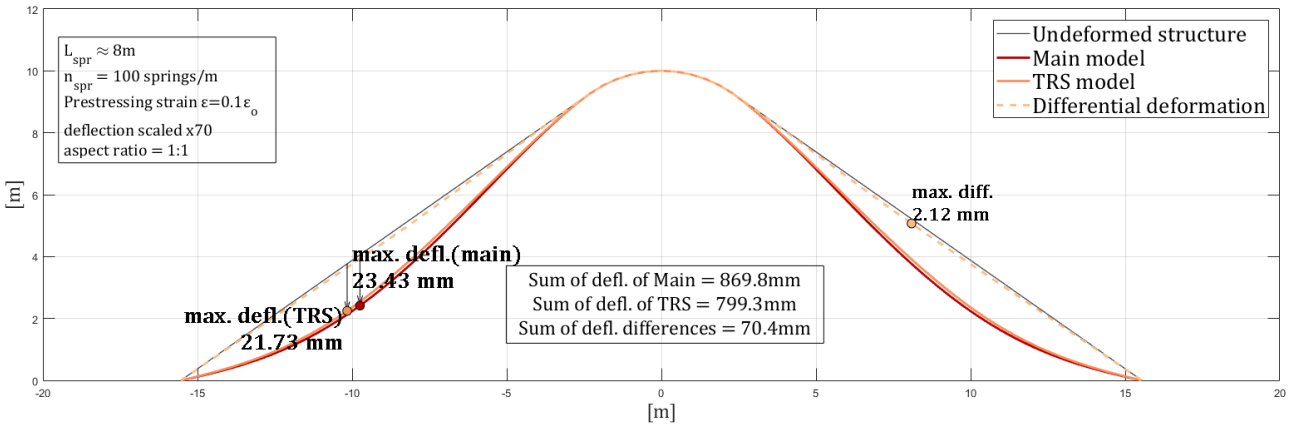

Figure 5.25: Comparison between the deformed shape of the TRS and the main model for for $\varepsilon = 0.1 \cdot \varepsilon_o$.

$L_{spr} = 8\text{m}$, $n_{spr} = 100$ springs/m, and $K_T \geq 10^7 \text{kN/m}$

5.2.6 Nonlinear Behaviour of TRS Model

As previously explained, the nonlinearity assigned to the transverse springs is a function of the longitudinal springs force. Transverse springs would 'perfectly yield' when the transverse force resisting the relative displacement between the rods F_T reaches the frictional coefficient μ times the longitudinal spring force F_P. The models are set up to investigate the effect of different frictional coefficients on the overall deformations along side different lengths of extended rods connected with springs L_{spr}. Since L_{spr} controls the amount of springs stretching along the total free length L_{fc}, the comparison between the different extended lengths ($L_{spr} = 8\text{m}$ and $L_{spr} = 15\text{m}$) is also relevant to understand the behaviour of the TRS model. Computational efforts for the case of nonlinear springs case are more substantial since the model accounts for material (or springs) nonlinearity as well as the cable's geometric nonlinearity. The details of the numerical parameters as shown in table 5.6.

Table 5.6: Numerical model parameter of TRS model for multiple frictional coefficient μ

μ	L_{spr} [m]	Max. deflec. TRS [mm]	Max. deflec. main [mm]	No. nodes	Solution time [sec]	No. iter.	Max. residual [kN]
N.A.	8	21.73	23.47	6257	26	12	0
N.A.	15	20	23.47	10435	116	258	0
0.40	8	26.15	23.47	6257	216	2058	4
0.40	15	24.9	23.47	10435	332	1843	4
0.20	8	32.22	23.47	6257	205	3422	4
0.20	15	31.92	23.47	10435	1503	4304	4
0.05	8	39.08	23.47	6257	226	2576	4
0.05	15	40.97	23.47	10435	408	2952	4

For all models $n_{spr} = 100$ springs/m and prestressing strain $= 4.425‰$.

Comparison between TRS Models with Different L_{spr} for Linear Shear Springs

Initially, and to grasp an understanding between the TRS models of $L_{spr} = 8$m and $L_{spr} = 15$m in linear springs case, the two models, assigned with the same number of springs per unit length n_{spr} and the same prestressing strain, are plotted together. The discrepancy between them is around 6%. This would help in understanding their behaviour in a nonlinear domain. Again, it is noticeable that TRS model with $L_{spr} = 15$m deforms slightly less than the other model. And as mentioned, slightly lowering the spring stiffness would decrease the discrepancy, the basis of lowering the stiffness are worthy of a further thorough examination. Figure 5.27 depicts the two models.

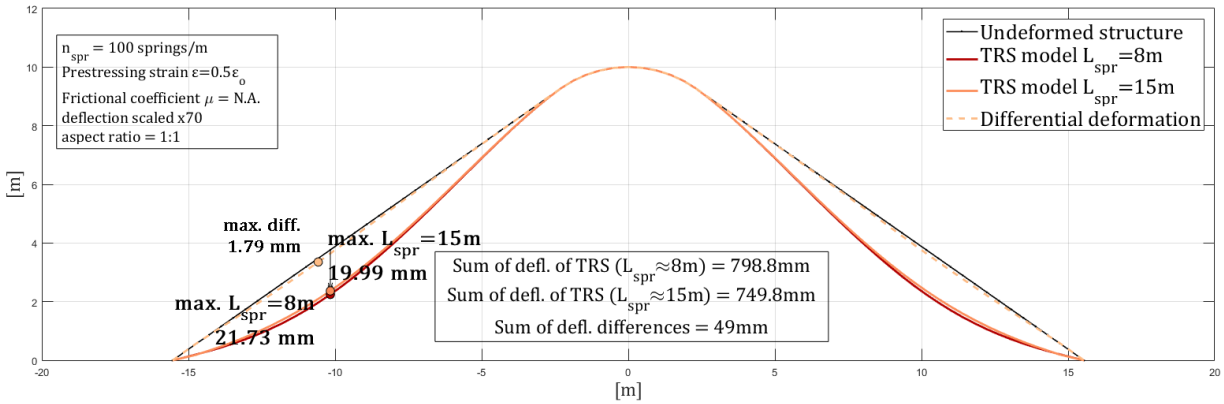

Figure 5.27: Comparison between the deformed shapes of TRS models with $L_{spr} = 8$ and 15m.

$n_{spr} = 100$ springs/m, $K_T \geq 10^7$kN/m and prestressing strain $= 4.425‰$

Comparison between TRS Models with Nonlinear Shear Springs

Assigning the springs with a nonlinearity feature allows the springs to imitate the stick/slip behaviour. The major advantage of the TRS model here is its ability to simulate a stick/slip behaviour between rods, a feature that the main model cannot simulate. Nevertheless, the plots include the main model to illustrate the change in the deformed shape and highlight the difference.

The lower the frictional coefficient μ the lower the force causing the slip thus the higher the deformations. This is noted in the figures below as the deformations increase when μ decreases. Although the models have different $L_{spr}s$ that affect the total number of springs and demonstrate discrepancies in linear springs case, it is noteworthy that the discrepancy between the two TRS models decreases when nonlinearity is triggered. This hints at a similar 'slip' behaviour between the two models. This slip behaviour is generally studied in this section with modest emphasis on what affects the slipping between rods in an actual manner. Further studies may be required to describe the nonlinear behaviour and to pursue verification with other experiments as the model setup is fairly flexible to adapt to other geometries. Nonetheless, the frictional coefficients μ are decided upon to be $\{0.4, 0.2, 0.05\}$. The results for $\mu = 0.4$ are shown from figure 5.29 to figure 5.33, for $\mu = 0.2$ from figure 5.35 to figure 5.39 and for $\mu = 0.05$ from figure 5.41 to figure 5.45.

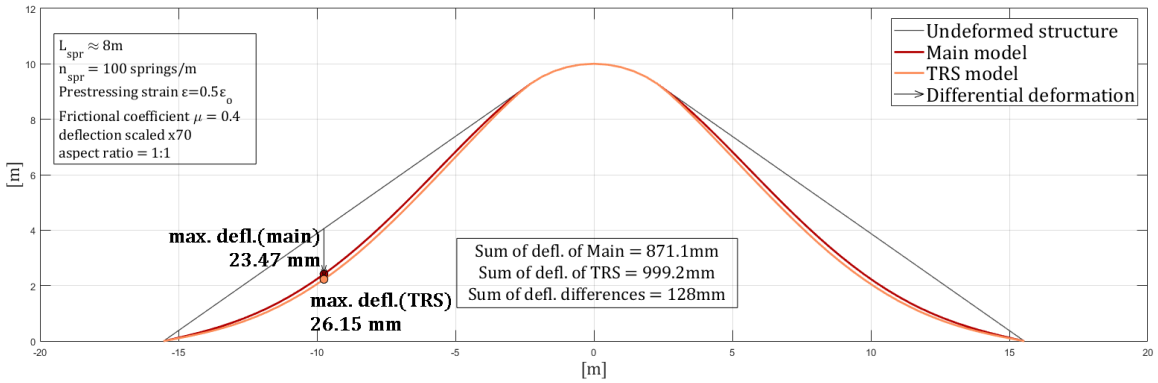

Figure 5.29: Comparison between the deformed shapes of TRS model with $L_{spr} = 8$m and the main model for $\mu = 0.4$.

$n_{spr} = 100$ springs/m, $K_T \geq 10^7$kN/m and $\varepsilon = 4.425‰$.

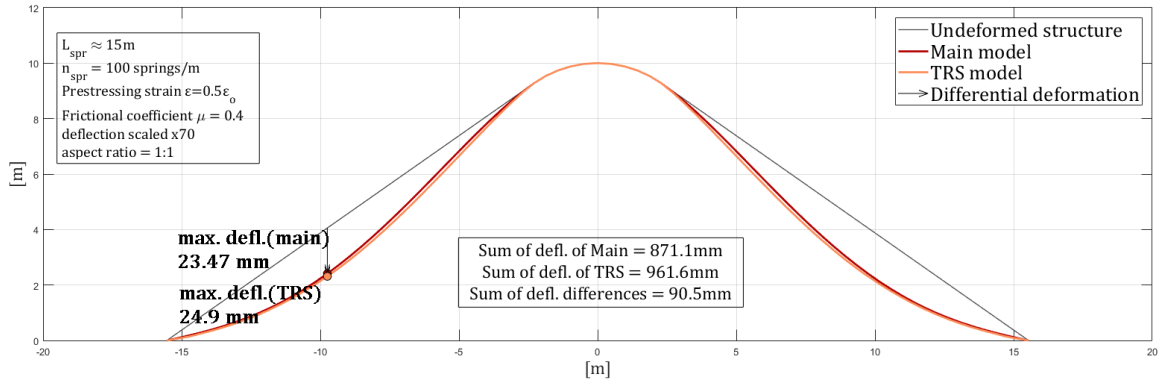

Figure 5.31: Comparison between the deformed shapes of TRS model with $L_{spr} = 15$m and the main model for $\mu = 0.4$.

$n_{spr} = 100$ springs/m, $K_T \geq 10^7$kN/m and $\varepsilon = 4.425‰$.

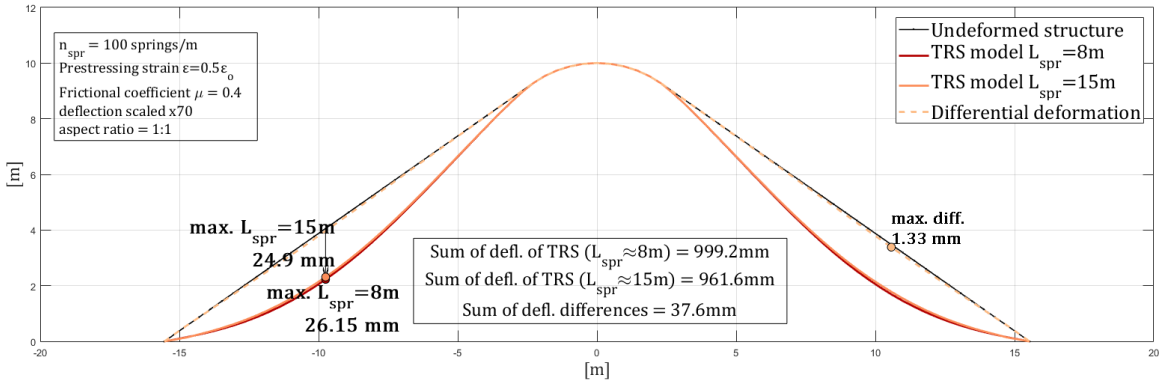

Figure 5.33: Comparison between the deformed shapes of TRS models with $L_{spr} = 8$ and 15m for $\mu = 0.4$.

$n_{spr} = 100$ springs/m, $K_T \geq 10^7$kN/m and $\varepsilon = 4.425‰$.

The discrepancy between the two TRS models ($L_{spr} = 8$m and $L_{spr} = 15$m) = 3.76% for $\mu = 0.4$ when comparing the sum of deflections of each TRS model.

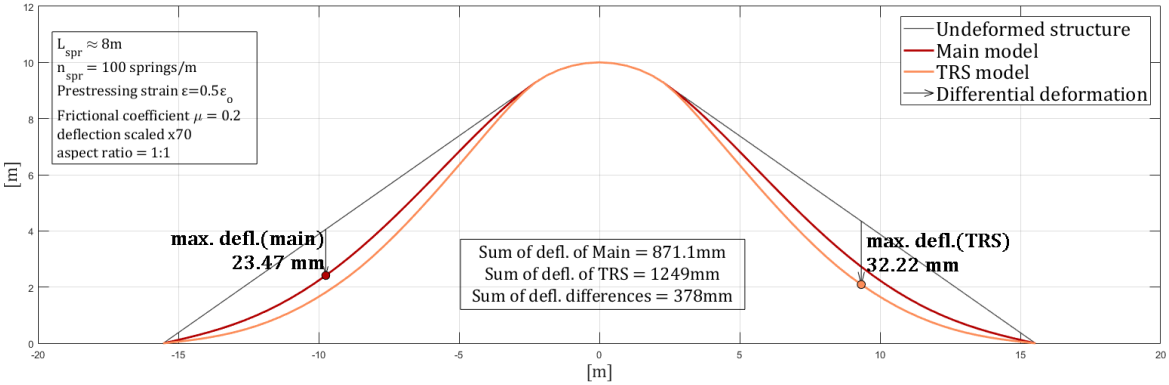

Figure 5.35: Comparison between the deformed shapes of TRS model with $L_{spr} = 8$m and the main model for $\mu = 0.2$.

$n_{spr} = 100$ springs/m, $K_T \geq 10^7$kN/m and $\varepsilon = 4.425‰$.

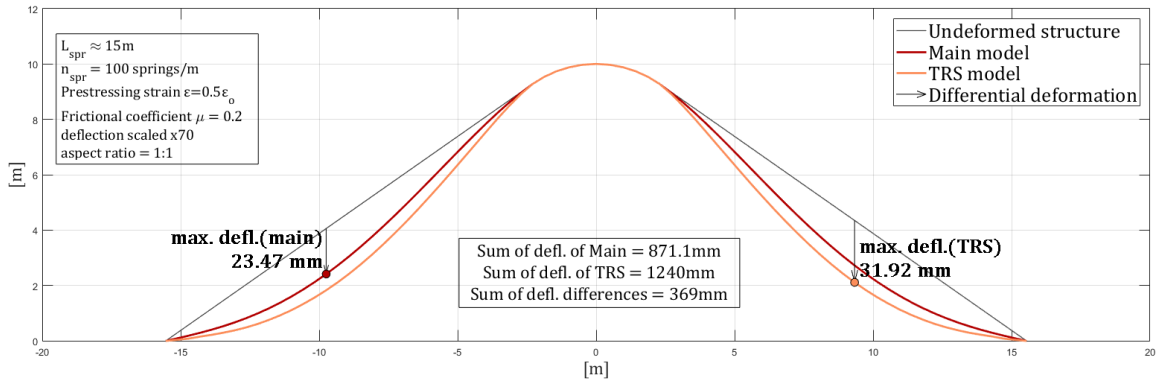

Figure 5.37: Comparison between the deformed shapes of TRS model with $L_{spr} = 15$m and the main model for $\mu = 0.2$.

$n_{spr} = 100$ springs/m, $K_T \geq 10^7$kN/m and $\varepsilon = 4.425‰$.

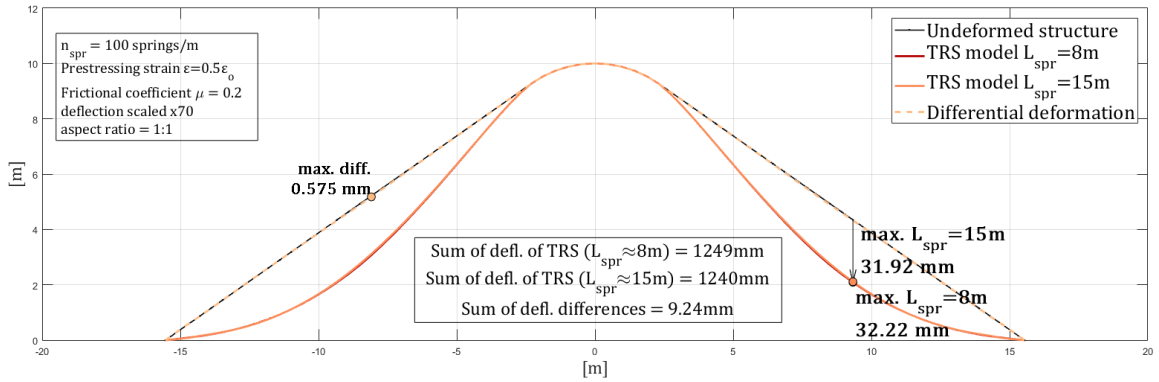

Figure 5.39: Comparison between the deformed shapes of TRS models with $L_{spr} = 8$ and 15m for $\mu = 0.2$.

$n_{spr} = 100$ springs/m, $K_T \geq 10^7$kN/m and $\varepsilon = 4.425‰$

An almost identical deformed shape for $\mu = 0.2$ between the two TRS models ($L_{spr} = 8$m and $L_{spr} = 15$m) with discrepancy = 0.74% when comparing the sum of deflections of each TRS model.

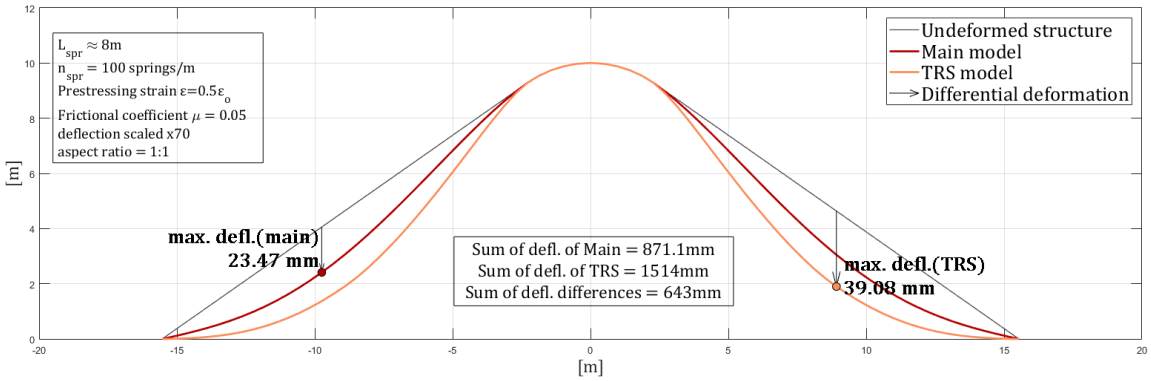

Figure 5.41: Comparison between the deformed shapes of TRS model with $L_{spr} = 8$m and the main model for $\mu = 0.05$.

$n_{spr} = 100$ springs/m, $K_T \geq 10^7$kN/m and $\varepsilon = 4.425‰$.

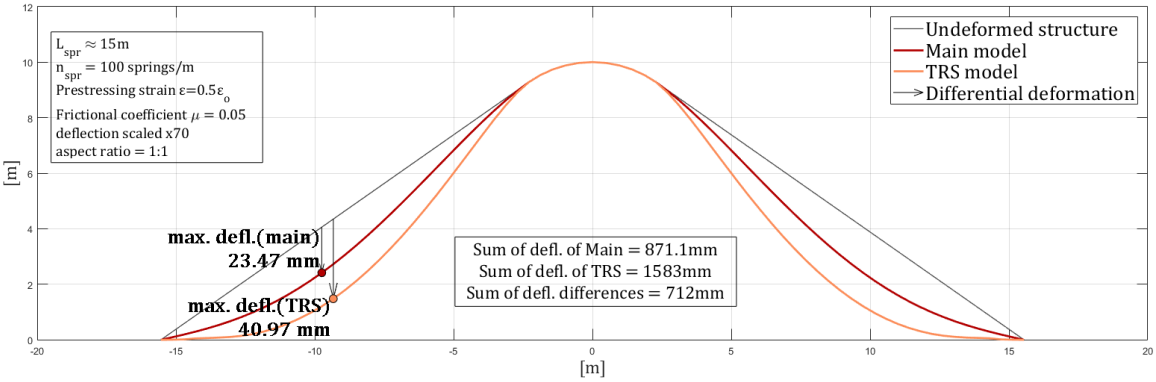

Figure 5.43: Comparison between the deformed shapes of TRS model with $L_{spr} = 15$m and the main model for $\mu = 0.05$.

$n_{spr} = 100$ springs/m, $K_T \geq 10^7$kN/m and $\varepsilon = 4.425‰$.

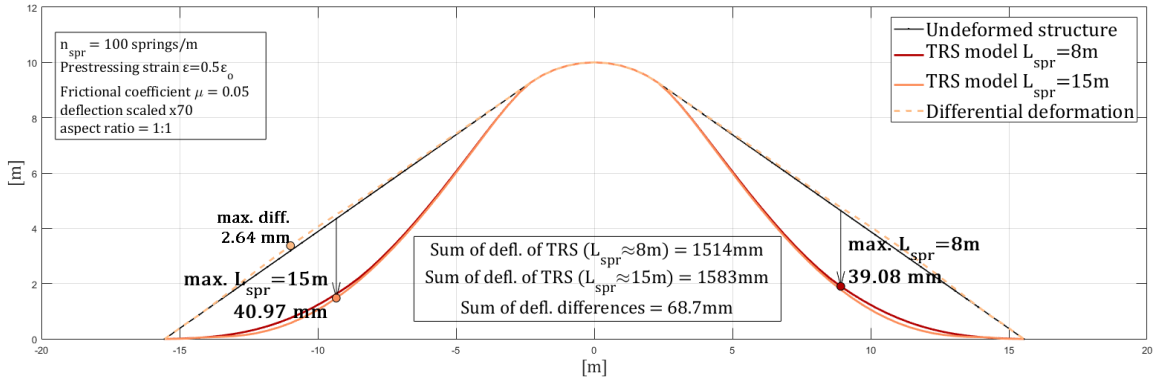

Figure 5.45: Comparison between the deformed shapes of TRS models with $L_{spr} = 8$ and 15m for $\mu = 0.05$.

$$n_{spr} = 100 \text{ springs/m},\ K_T \geq 10^7 \text{kN/m and } \varepsilon = 4.425‰$$

The discrepancy between the two TRS models ($L_{spr} = 8$m and $L_{spr} = 15$m) = 4.54% for $\mu = 0.05$ when comparing the sum of deflections of each TRS model.

5.2.7 Comparison Based on Dynamic Properties

To grasp a further understanding of the behaviour of the TRS model, the dynamic properties are studied. Nonlinear modal analysis (accounting the change in geometry sagging due to self-weight) is conducted and compared to the main model counterpart. The low order modes (from first to fifth) are mainly governed by the prestressing value (namely tension forces) while the bending stiffness, which is most relevant in this context, can significantly effect the results of higher modes, especially in the case of short and stiff cables [12] (and further explained in section 2.4.2). The first 14 modes are obtained from both models and the results show a roughly constant error over all modes. This is a twofold indication; firstly that the bending stiffness effects are sufficiently represented in the TRS model, and secondly, the low error values are consistent with the discrepancy obtained from the nonlinear static analysis. Modal analysis results are listed in table 5.7 and table 5.8 and depicted in figure 5.47 and figure 5.49 for $n_{spr} = 100$ springs/m and $n_{spr} = 200$ springs/m.

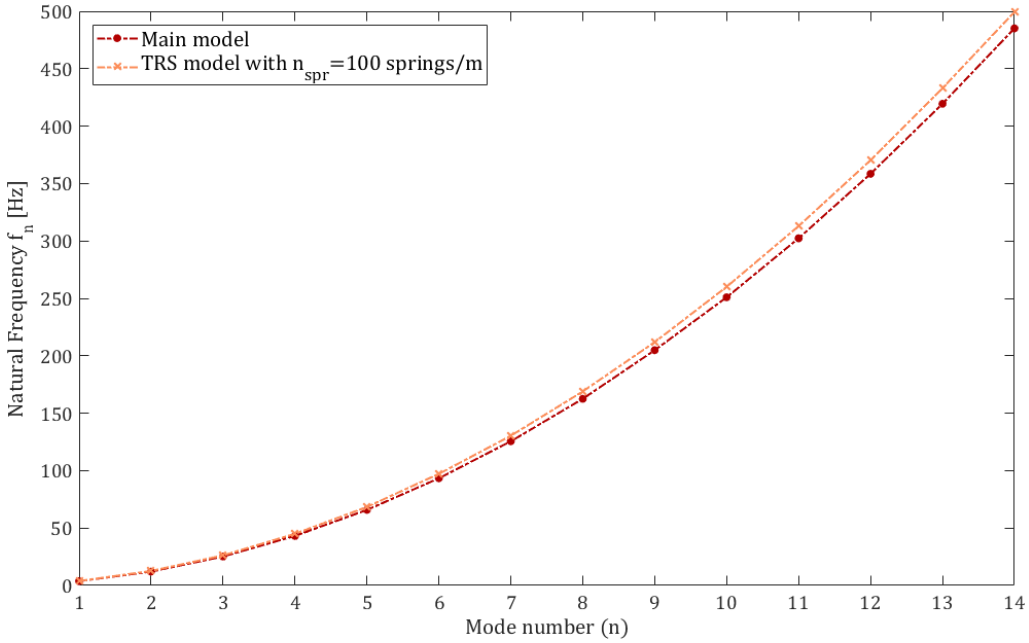

Figure 5.47: Modal analysis results comparing the TRS model with $n_{spr} = 100$ [springs/m] and the main model with a corresponding c value that identifies the second moment of area I_{idn} as in table 4.3

$$L_{spr} = 8\text{m},\ K_T \geq 10^7\text{kN/m},\ \varepsilon = 4.425‰,\ c = 0.853$$

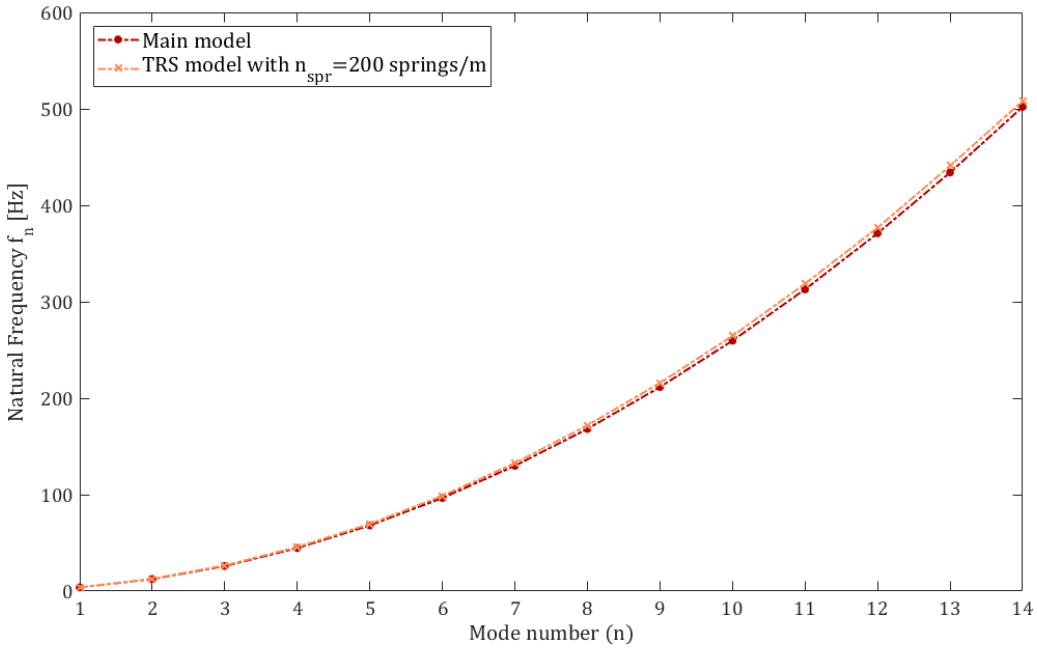

Figure 5.49: Modal analysis results comparing the TRS model with $n_{spr} = 200$ [springs/m] and the main model with a corresponding c value that identifies the second moment of area I_{idn} as in table 4.3.

$$L_{spr} = 8\text{m},\ K_T \geq 10^7\text{kN/m},\ \varepsilon = 4.425‰,\ c = 0.919$$

Table 5.7: Modal analysis of main model and TRS model for $n_{spr} = 100$ [springs/m], $L_{spr} = 8$m and prestressing strain $= 0.5\varepsilon_o$.

Vibrating mode	Natural frequencies of main model [Hz]	Natural frequencies of TRS model [Hz]	Error
1	3.75	3.87	3.42%
2	12.08	12.65	4.74%
3	25.21	26.20	3.94%
4	43.11	45.01	4.40%
5	65.79	68.36	3.90%
6	93.32	97.18	4.14%
7	125.53	130.35	3.84%
8	162.54	168.96	3.95%
9	204.89	211.93	3.43%
10	250.96	260.07	3.63%
11	302.32	312.96	3.52%
12	358.49	370.32	3.30%
13	419.48	433.04	3.23%
14	485.12	499.42	2.95%

Table 5.8: Modal analysis of main model and TRS model for $n_{spr} = 200$ [springs/m], $L_{spr} = 8$m and prestressing strain $= 0.5\varepsilon_o$.

Modal number	Main M. natural frequencies [Hz]	Shear spr. M. natural frequencies [Hz]	Error
1	3.87	3.95	2.07%
2	12.50	12.85	2.83%
3	26.08	26.71	2.42%
4	44.61	45.76	2.59%
5	68.08	69.67	2.33%
6	96.56	98.84	2.36%
7	129.90	132.78	2.22%
8	168.19	171.88	2.19%
9	211.58	215.90	2.04%
10	259.69	264.59	1.88%
11	312.84	318.70	1.87%
12	370.97	376.76	1.56%
13	434.04	440.94	1.59%
14	502.01	508.14	1.22%

Chapter 6

Summary and outline

6.1 Summary

Chapter 3 presented a parameterized numerical model of a cable element following an extradosed bridge geometry. The numerical model was validated with the catenary analytical solution and further investigations on the effects of a saddle deviator were conducted. The saddle deviator positively affects the cable stiffness by suppressing the deformations near the pylon. This suppression is a resultant of the geometric configuration of the saddle. Figure 6.1 compares the sagging of cables with and without saddle anchorage.

The longer the saddle radius the higher the effects of geometry on the cable stiffness. The geometry effect leads to shortening of the sagging length of the cable which also in turn leads to a higher effective modulus of elasticity, hence the lessened sagging.

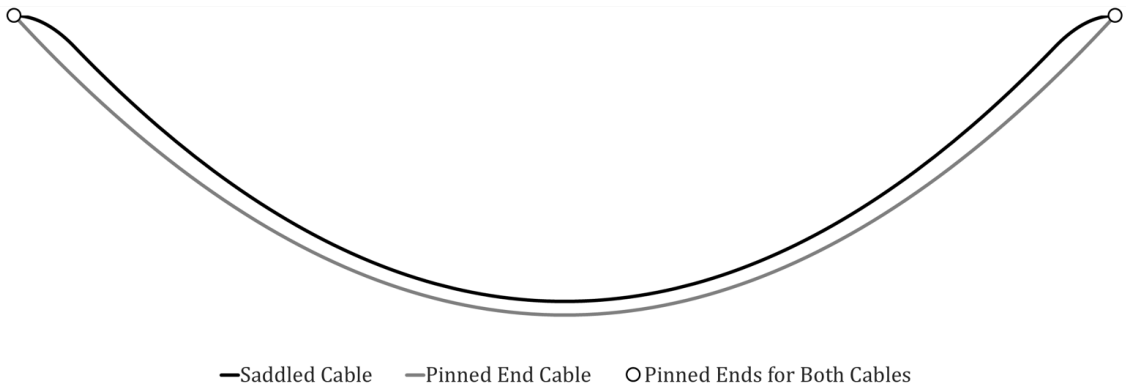

Figure 6.1: Schematic showing the geometric effect of a saddle geometry

The numerical model was further studied for the effects of equal prestressing forces on both sub-structure (i.e. deck) ends of the cable. The distribution of the stresses along the proposed saddle configuration of the numerical model showed a good correlation with the analytical solution for the

radial pressure. This was further developed by acquiring the vertical component of the radial pressure to obtain the total vertical force acting on the pylon.

The sag of the cable was studied using truss elements as well as beam elements with multiple bending stiffness values. The addition of bending stiffness effects to the cable showed a clear reduction of sagging. This highlights the effects of bending stiffness in stay-cable analysis as it is clearly manifested in short cables such as extradosed bridge stay cables.

Dynamic properties were also investigated by conducting a nonlinear modal analysis. The numerical models with beam elements showed a clear divergence of identified natural frequencies from the model with truss elements. Modeling with beam elements changes the natural frequencies nonlinearly and depending on the value of EI the results can be altered starting from the fifth vibration mode.

Chapter 4 presented a numerical approach to identify exact values of bending stiffness using shear springs as transverse connections between rods. The concept is based on utilizing the parallel axis theorem of calculating the second moment of area value to include partial contact between rods. This is done by controlling the number and the stiffness of the shear springs. The numerical model was validated using the upper and lower bounds of the parallel axis theorem. Moreover, a method was suggested to account the findings of the local model on other global models using quantified ratios of second moment of area.

In Chapter 5 the numerical method used to identify the bending stiffness was applied on a numerical model following the extradosed bridge cable geometry and was compared to a global model that was assigned with the quantified ratios of second moment of area. The geometry of the two models was identical and thus the comparison was possible. Even though the refined numerical model required considerable computational space, it correlated well with the global model statically and showed low discrepancies in the dynamic properties. However, there are some uncertain aspects regarding the quantification method used in chapter 3. Moreover, experimental testing are needed to validate the suggested method. Nevertheless, the method provided consistent results and the effect of stick/slip behaviour between rods was simulated using nonlinear transverse springs.

6.2 Outline

Numerical models developed in this thesis provided rigorous results, suggested below are aspects that could be further studied:

- Accounting for a differential pretensioning of the cable on the proposed geometry. The differential pretensioning causes lateral forces on the saddle as well as secondary moments due to a corresponding eccentricity of the vertical force. The radial springs representing the saddle might be assigned with a transverse stiffness to resist the differential pretensioning.
- Quantifying the frictional effects of different cable spacers quantitatively to be applied using shear springs model.
- Experimental identification of bending stiffness using short parallel wire/strand cables to further study the shear springs numerical model.

Appendix A

The Catenary Solution

The analytical solution for the catenary problem is well explained by [6] and further developed by [14] as follows, where $\sin\alpha = \frac{dy}{dx}$, $\cos\alpha = \frac{dx}{ds}$, $\tan\alpha = \frac{dy}{dx}$:

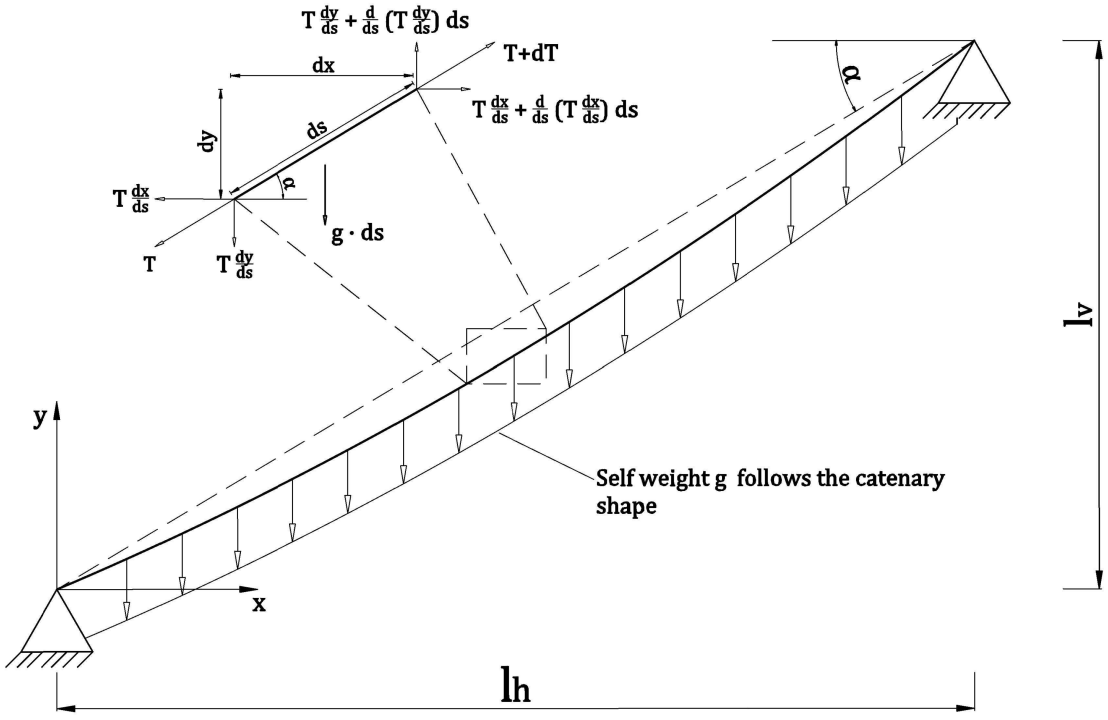

Figure A.1: Equilibrium of an infinitesimal element of a zero flexural stiffness member under its self weight and pinned at its ends. *Figure inspired by [6]*

The infinitsimal element infers that vertical equilibrium:

$$\frac{d}{ds}(T\frac{dy}{ds}) = g \tag{A.1}$$

where T is the prestressing force in kN and g being the weight per unit length in kN/m. Horizontal equilibrium implies

$$\frac{d}{ds}(T\frac{dx}{ds}) = 0 \tag{A.2}$$

Substituting $T = H\frac{ds}{dx}$ (where $H = T\frac{dx}{ds}$ as the horizontal tension component) and a subsequent multiplication by $\frac{ds}{dx}$ into equation A.1 give

$$H\frac{d^2y}{dx^2} = g\frac{ds}{dx} \tag{A.3}$$

Using the Pythagorean equation of $(ds)^2 = (dx)^2 + (dy)^2$ in equation A.3 gives

$$H\frac{d^2y}{dx^2} = g\sqrt{1 + \left(\frac{dy}{dx}\right)^2} \tag{A.4}$$

to simplify, $a = \frac{dy}{dx}$ is introduced into equation A.4 such that $\frac{da}{dx} = \frac{g}{H}\sqrt{1+a^2}$, which gives:

$$\frac{da}{\sqrt{1+a^2}} = \frac{g}{H}dx \tag{A.5}$$

By integrating both sides we get at:

$$\ln\left(a + \sqrt{1+a^2 2}\right) = \frac{g}{H}x + K_1 \tag{A.6}$$

Substitution of $b = \frac{w}{H}x + k_1$ gives

$$a + \sqrt{1+a^2} = e^b \Rightarrow a = \frac{e^b - e^{-b}}{2} = \sinh b \tag{A.7}$$

thereby reaches to

$$\frac{dy}{dx} = \sinh\frac{g}{H}x + K_1 \tag{A.8}$$

Integrating this expression solves the differential equation analytically leaving the two integration constants K_1 and K_2, which are then solved by evaluating the boundary conditions at $x = 0, y = 0$ and $x = l_h, y = l_v$ (L_c being the chord length between the two supports). This solution was obtained by [14]

$$y(x) = \frac{H}{g}\cosh(\frac{g}{H}x + K_1) + K_2 \tag{A.9}$$

$$K_1 = \sinh^{-1}(\frac{gl_v}{2H\sinh\frac{gL_c}{2H}}) - \frac{gL_c}{2H} \tag{A.10}$$

$$K_2 = -\frac{H}{g}\cosh(K_1) \tag{A.11}$$

Appendix B

Scripts of modeling an extradosed bridge cable

B.1 Geometry formulation using MATLAB

Below is the full script used to formulate the geometry of the parameterized extradosed bridge cable. The results are extracted in a set of text files that are then included in software SOFiSTik.

```
%% Input Parameters
WireDia=0.1; % Cable Diameter in [m]
Ee=2e8;       % E modulus of steel in [kN/m^2]
alpha=35;    % Inclination Angle, unit: [Degrees]
H=20;        % Peak Height of Saddle, unit: [m]
R=4;         % Radius of Saddle, unit: [m]
pre=6950;    % Prestressing force in [kN]
nsad=25;     % Number of elements required at saddle
ncab=60;     % Number of elements required at rest of cable
%Second moment of area [cm^4]
Iy= pi*WireDia^4/64*1e8; % of a solid section
Perc=1;      % Precentage of cable to be considered from the other side
             % Default is 1 to account for 100% of the cable
NMode=10; %number of modes required from modal analysis

%% Other Used Parameters
area=pi*WireDia^2/4;
gamma=78.5;       %unit Weight of steel
MassUnit=area*gamma*100;
stress=pre/area;
alpha=deg2rad(alpha);
Lfc=(H-R*(1-cos(alpha)))/sin(alpha); % Free length of cable
```

```
Lsad=nsad*2*R*sin(alpha/(2*nsad));  % Total length of Saddle (
   perimeter)
lh=Lfc*cos(alpha);                  %Horizontal inclination of Lfc

% Effective modulus of elasticity in [MPa]
Ei=(Ee/(1+((gamma*lh)^2*Ee/(12*stress^3))))*1e-3;

% To make sure user input is correct
Perc=1-Perc;
if Perc>1.0 || Perc<0
   Perc=0.5;
   warning('Inserted Percentage of Cable to be Cut is not accepted');
   A=['New Percentage is set to ',num2str(Perc)];
   disp(A);
end

nremain=ncab-round(Perc*ncab);

%Utilization of symmetry of the geometry
%Positive coordinates only in nodecorpos
nodecorpos=zeros(nsad+ncab+1,3);
%nodecorpos(:,1) are the node numbers
%nodecorpos(:,2) are the x coordinate of nodes
%nodecorpos(:,3) are the z coordinate of nodes

%Semi-rigid radial springs respresenting the saddle
springincpos=zeros(nsad+1,3);
%springincpos=zeros(:,1); Saddle nodal number to which the
%spring is assigned to
%springincpos=zeros(:,2) spring inclination dx
%springincpos=zeros(:,3) spring inclination dz

%% Saddle nodes and spring inclinations
% At Saddle:
for i=0:nsad
    nodecorpos(i+1,1)=nremain+nsad+1+i;
    nodecorpos(i+1,2)=R*sin((alpha)*i/nsad);
    nodecorpos(i+1,3)=H-R+R*cos((alpha)*i/nsad);
    springincpos(i+1,1)=nodecorpos(i+1,1);
    springincpos(i+1,2)=-sin((alpha)*i/nsad);
    springincpos(i+1,3)=-cos((alpha)*i/nsad);
end
n=nsad+1;
% Remainder of straight cable nodes
```

```
for i=1:ncab
    nodecorpos(i+n,1)=nremain+nsad*2+1+i;
    nodecorpos(i+n,2)=R*sin(alpha)+(Lfc)/ncab*i*cos(alpha);
    nodecorpos(i+n,3)=H-R*(1-cos(alpha))-(Lfc/ncab*i*sin(alpha));
end
%%
%Forming a new vector set to obtain the total geometry
%in nodecor vector set
n=nremain+nsad*2+ncab+1;
nodecor=zeros(n,3);

n=nremain+nsad;
for i=1:n
    nodecor(i,1)=nodecorpos(end-ncab+nremain,1)-...
                    (nremain+nsad*2+nremain-(i-1));
    nodecor(i,2)=-nodecorpos(end-ncab+nremain-(i-1),2);
    nodecor(i,3)=nodecorpos(end-ncab+nremain-(i-1),3);
end
n=ncab+nsad;
nodecor(end-n:end,:)=nodecorpos(:,:);

%Like wise, springs are formed in the negative side of the x axis
springinc=zeros(nsad*2+1,3);

for i=0:nsad-1
    springinc(i+1,1)=springincpos(end-i,1)-(nsad-i)*2;
    springinc(i+1,2)=-springincpos(end-i,2);
    springinc(i+1,3)=springincpos(end-i,3);
end
springinc(nsad+1:nsad*2+1,:)=springincpos(1:nsad+1,:);


%% Nodal Mass as a Ratio of Unit Mass
% addition of nodal mass to each node

nodemass=zeros(nremain+nsad*2+ncab+1,1);
nodemass(1,1)=nodecor(1,1);
nodemass(1,2)=Lfc/(2*ncab)*MassUnit;
nodemass(end,1)=nodecor(end,1);
nodemass(end,2)=Lfc/(2*ncab)*MassUnit;

for i=2:nremain
    nodemass(i,1)=nodecor(i,1);
```

```
    nodemass(i,2)=Lfc/ncab*MassUnit;     % At Cable (Negative X
       Direction)
end

for i=nremain+2:nremain+nsad*2
    nodemass(i,1)=nodecor(i,1);
    nodemass(i,2)=Lsad/(nsad)*MassUnit;

end

for i=1:ncab-1
    nodemass(end-i,1)=nodecor(end-i,1);  % At Cable (Positive X
       Direction)
    nodemass(end-i,2)=Lfc/ncab*MassUnit;
end

nodemass(nremain+1,1)=nodecor(nremain+1,1);
nodemass(nremain+1,2)=(Lsad/nsad+Lfc/ncab)/2*MassUnit;
nodemass(nremain+nsad*2+1,1)=nodecor(nremain+nsad*2+1,1);
nodemass(nremain+nsad*2+1,2)=(Lsad/nsad+Lfc/ncab)/2*MassUnit;

%% Exporting of Text Files of Parameters
% To be imported in SOFiSTiK

Input=fopen('Input.txt','w');
Nodes = fopen('Nodes.txt','w');
Springs = fopen('Springs.txt','w');
EndsFixed = fopen('EndsFixed.txt','w');
EndsHinged = fopen('EndsHinged.txt','w');
Element = fopen('Element.txt','w');
Prestress = fopen('Prestress.txt','w');
NodalMass=fopen('NodalMass.txt','w');

input= fopen('INPUT.txt','w');
fprintf(input,'#DEFINE area=%f\r\n',area*1e6);
fprintf(input,'#DEFINE pre=%f\r\n',pre);
fprintf(input,'#DEFINE Emodulus=%f\r\n',Ei);
fprintf(input,'#DEFINE Iy=%f\r\n',Iy);
fprintf(input,'#DEFINE NMODE=%d\r\n',NMode);
fclose(input);
%% Nodes Export
for i=1:length(nodecor(:,1))
    fprintf(Nodes,'NODE NO %d X %f[m] Y %f[m]\r\n',...
        nodecor(i,1),nodecor(i,2),nodecor(i,3));
```

```
end
%% Saddle Radial Springs Export
for i=1:length(springinc(:,1))
    fprintf(Springs,'SPRI NO %d NA %d DX %f DY %f CP #KONS\r\n',...
        springinc(i,1),springinc(i,1),springinc(i,2),springinc(i,3));
end
%% Elements Export, Truss of Beam Elements
for i=1:nremain+nsad*2+ncab
    fprintf(Element,'TRUS NO %d NA %d NE %d NCS 1\r\n',...
        nodecor(i,1),nodecor(i,1),nodecor(i+1,1));
%     fprintf(Beam,'BEAM NO %d NA %d NE %d NCS 1\r\n',...
%         nodecor(i,1),nodecor(i,1),nodecor(i+1,1));
end

for i=1:nremain+nsad*2+ncab+1
    fprintf(NodalMass,'MASS NO %d %f[kg]\r\n',...
        nodemass(i,1),nodemass(i,2));
end
% Truss Elements or beam elements
fprintf(Prestress,'TRUS FROM %d to %d INC 1 TYPE VX $(pre)\r\n',...
    nodecor(1,1),nodecor(nremain+nsad,1));
fprintf(Prestress,'TRUS FROM %d to %d INC 1 TYPE VX $(pre)\r\n',...
    nodecor(nremain+nsad+1,1),nodecor(end-1,1));
% fprintf(Prestress,'BEAM FROM %d to %d INC 1 TYPE PNX $(pre)\r\n',...
%       nodecor(1,1),nodecor(nremain+nsad,1));
% fprintf(Prestress,'BEAM FROM %d to %d INC 1 TYPE PNX $(pre)\r\n',...
%   nodecor(nremain+nsad+1,1),nodecor(end-1,1));

fprintf(EndsFixed,'NODE %d FIX F\r\n',nodecor(1,1));
fprintf(EndsFixed,'NODE %d FIX F',nodecor(end,1));
fprintf(EndsHinged,'NODE %d FIX PP\r\n',nodecor(1,1));
fprintf(EndsHinged,'NODE %d FIX PP',nodecor(end,1));

fclose(Nodes);
fclose(Springs);
fclose(NodalMass);
fclose(EndsFixed);
fclose(EndsHinged);
fclose(Prestress);
fclose(Element);

%% Plotting to obtain the final geometry
% plot(nodecor(:,2),nodecor(:,3),'bo');
% for i=1:length(nodecor(:,1))
```

```
%      h=int2str(nodecor(i,1));
%      text(nodecor(i,2),nodecor(i,3),h);
% end
```

B.2 Solving using SOFiSTiK

The script below describes the solving procedure and the commands used in the software SOFiSTiK.

Numerical_Model.dat

```
$ Nonlinear cable analysis - Guido Morgenthal
$ Modified by Tajammal Abbas
$ Costumized by Abdulmagid Bendalla

#INCLUDE Input.txt

+PROG AQUA urs:1
HEAD MATERIAL AND CROSS SECTIONS
ECHO FULL FULL
$ code
NORM DIN EN1992-2004
$ cable material

STEE NO 1 Type Y ES $Emodulus GAM 0  $ FY=1520 FT=1770

$ cross sectional properties
SVAL NO 1 MNO 1 A $area[mm2] $ IY $Iy[cm4]
END

+PROG SOFIMSHA urs:2
HEAD GEOMETRY OF CABLE
SYST 2D GDIV 1000 GDIR NEGY

$ Restraints
$ #INCLUDE EndsFixed.txt                              $ CHANGE FIX FOR SENSITIVITY    PP F
 #INCLUDE EndsHinged.txt

LET#KONS=1e20
#INCLUDE Nodes.txt
#INCLUDE Springs.txt
#INCLUDE Element.txt
#INCLUDE NodalMass.txt
END

+PROG SOFILOAD urs:3
HEAD SELF WEIGHT AND PRE-STRESS
LC NO 1000 DLY -1.0                          $ self weight cosideration
#INCLUDE Prestress.txt
END
```

```
+PROG ASE urs:12
HEAD NONLINEAR PRIMARY LC ANALYSIS
CTRL ITER4 V4 5
CTRL WARN 636                   $ To Eliminate a system constraint related to Spring K value
                                $ maximum allowed is  1E6
SYST PROB TH3 ITER 50000 FMAX 1.1
LC NO 1000
END

+PROG ASE urs:4
HEAD NONLINEAR MODAL ANALYSIS
SYST PROB TH3 PLC 1000 ITER 1000
CTRL ITER V3 1
CTRL WARN 636
EIGE NEIG $NMODE LC 1
END
```

B.3 TRS model

The TRS model is a continuation of the main model described at the beginning of the appendix. Below is the code used to define the geometry, the nodes and utilization of the symmetry. The output is exported in text file using the same technique as in appendix B.1.

```
%% Input Parameters: Geometry
alpha=35;    % Inclination Angle, unit: [Degrees]
H=10;        % Peak Height of Saddle, unit: [m]
R=4;         % Radius of Saddle, unit: [m]
ncab=24;     % Number of elements required at free cable
nspr=100;    % Number of shear springs per unit length
Lspr=8;
zi=0.1;     % Spacing between wires
Perc=1;    % Precentage of cable to be considered from the other side

%% Other Used Parameters
alpha=deg2rad(alpha);
Lfc=(H-R*(1-cos(alpha)))/sin(alpha);
Ri=R-zi;
Hi=H-zi;
%%
% The spring densities shall be the same at the saddle and at the free
    length Lspr
%% Iteration 1
```

```
% an arbitrary choice of a large number of saddle elements to
   calculate the length Lsad
nsad=randi([100 200],1,1);
Lsad=nsad*2*Ri*sin(alpha/(2*nsad));  % Total length of Saddle bottom
   wire
nsen=round(nsad*Lspr/Lsad);          % Total number of spring at Lspr
%Recalculation of Lspr to adapt to the new total number of springs
   distributed along Lspr
Lspr=Lsad*nsen/nsad;

%Iteration 2
nsad=round(nspr*Lsad);
Lsad=nsad*2*Ri*sin(alpha/(2*nsad));  % Total length of Saddle bottom
   wire
nsen=round(nsad*Lspr/Lsad);
Lspr=Lsad*nsen/nsad;
% Check if cable precentage to be considered is within [0,100%] of
   cable
% length
Perc=1-Perc;
if Perc>1.0 || Perc<0
   Perc=0.5;
   warning('Inserted Percentage of Cable to be Cut is not accepted');
   A=['New Percentage is set to ',num2str(Perc)];
   disp(A);
end

%%
nremain=ncab-round(Perc*ncab);
nodecorpos=zeros((nsad+1)*3+nsen*3+ncab,3);
springincpos=zeros(nsad+1,4);
% Node numbering system begins from first node of the free cable in
   the negative side going on to the positive. It rewinds at each rod
   until all rods are compeleted then it finishes with the remaining
   nodes of Lfc beginning at the top of the saddle (x=0) at the bottom
    wire
for i=0:nsad
    %n: number of the first node in the positive direction
    n=(nremain)+nsen+(nsad+1);
    nodecorpos(i+1,1)=n+i;
    nodecorpos(i+1,2)=Ri*sin((alpha)*i/nsad);
    nodecorpos(i+1,3)=Hi-Ri+Ri*cos((alpha)*i/nsad);
    springincpos(i+1,2)=sin((alpha)*i/nsad);
    springincpos(i+1,3)=cos((alpha)*i/nsad);
```

```
    springincpos(i+1,1)=nodecorpos(i+1,1);
end
%n: number of the first node after the saddle is determined in the
   positive x %direction
n=nsad+1;
for i=1:nsen
    nodecorpos(i+n,1)=((nremain)+nsen+nsad)+nsad+1+i;
    nodecorpos(i+n,2)=Ri*sin(alpha)+Lspr/nsen*i*cos(alpha);
    nodecorpos(i+n,3)=Hi-Ri*(1-cos(alpha))-Lspr/nsen*i*sin(alpha);
end
%% Second rod geometry, basic shifting of first rod by corrisponding x
   ,y
for i=0:nsad
    n=nsad+1+nsen+1;
    nodecorpos(i+n,1)=(nremain)+(nsen+nsad+1)*2+nsad+nsen+i;
    nodecorpos(i+n,2)=nodecorpos(i+1,2)+zi*sin(alpha/nsad*i);
    nodecorpos(i+n,3)=nodecorpos(i+1,3)+zi*cos(alpha/nsad*i);
end

for i=1:nsen
    n=nsad+1+nsen+1+nsad;
    nn=nsad+1;
    nodecorpos(i+n,1)=(nremain)+(nsen+nsad+1)*2+nsad+nsen+nsad+i;
    nodecorpos(i+n,2)=nodecorpos(i+nn,2)+zi*sin(alpha);
    nodecorpos(i+n,3)=nodecorpos(i+nn,3)+zi*cos(alpha);
end
%% Third rod geometry, basic shifting of first rod by corresponding x,
   y
for i=0:nsad
    n=(nsad+1+nsen)*2+1;
    nodecorpos(i+n,1)=(nremain)+(nsen+nsad+1+nsad+nsen)*2+(nsen+nsad)
       +1+i;
    nodecorpos(i+n,2)=nodecorpos(i+1,2)+2*zi*sin(alpha/nsad*i);
    nodecorpos(i+n,3)=nodecorpos(i+1,3)+2*zi*cos(alpha/nsad*i);
end
n=(nsad+1+nsen)*2+nsad+1;
nn=nsad+1;
for i=1:nsen
    nodecorpos(i+n,1)=(nremain)+(nsen+nsad+1+nsad+nsen)*2+(nsen+nsad+
       nsad+1)+i;
    nodecorpos(i+n,2)=nodecorpos(i+nn,2)+2*zi*sin(alpha);
    nodecorpos(i+n,3)=nodecorpos(i+nn,3)+2*zi*cos(alpha);
end
```

```
n=(nsad+1+nsen)*3;
% Remainder of straight cable nodes Lfc
for i=1:ncab
    nodecorpos(i+n,1)=nremain+(nsen+nsad+nsad+1+nsen)*3+i;
    nn=(nsad+1+nsen)*2;
    nodecorpos(i+n,2)=nodecorpos(nn,2)+(Lfc-Lspr)/ncab*i*cos(alpha);
    nodecorpos(i+n,3)=abs(nodecorpos(nn,3)-(Lfc-Lspr)/ncab*i*sin(alpha
       ));
end
%% -----Utilization of Geometrical Symmetry------
n=(nremain)+(nsad+nsen+1)*3+(nsad+nsen)*3+(ncab);
nodecor=zeros(n,3);
springinc=zeros(nsad*2+1,4);
n=nremain;

for i=1:n
    nodecor(i,1)=nodecorpos(end-ncab+nremain,1)-((nremain-1)+...
        (nsen+nsad+1)*3+(nsad+nsen)*3+nremain-(i-1));
    nodecor(i,2)=-nodecorpos(end-ncab+nremain-(i-1),2);
    nodecor(i,3)=nodecorpos(end-ncab+nremain-(i-1),3);
end

for i=1:nsad
    springinc(i,1)=nremain+nsen+i;
    springinc(i,2)=-springincpos(end-(i-1),2);
    springinc(i,3)=springincpos(end-(i-1),3);
    springinc(i,4)=springincpos(end-(i-1),4);
end
springinc(nsad+1:end,:)=springincpos(:,:);

n=nsad+nsen; % Total number of a rod's nodes form beginning of rod
   till the node before saddle top
for i=1:n
    nodecor(n+(nremain)-i+1,1)=nodecorpos(i+1,1)-(i)*2;
    nodecor(n+(nremain)-i+1,2)=-nodecorpos(i+1,2);
    nodecor(n+(nremain)-i+1,3)=nodecorpos(i+1,3);
    nodecor((n)*3+1+(nremain)-i+1,1)=nodecorpos(i+(nsad+nsen+1)+1,1)-(
       i)*2;
    nodecor((n)*3+1+(nremain)-i+1,2)=-1*nodecorpos(i+(nsad+nsen+1)
       +1,2);
    nodecor((n)*3+1+(nremain)-i+1,3)=nodecorpos(i+(nsad+nsen+1)+1,3);
    nodecor((n)*5+2+(nremain)-i+1,1)=nodecorpos(i+(nsad+nsen+1)*2+1,1)
       -(i)*2;
```

```
    nodecor((n)*5+2+(nremain)-i+1,2)=-1*nodecorpos(i+(nsad+nsen+1)
       *2+1,2);
    nodecor((n)*5+2+(nremain)-i+1,3)=nodecorpos(i+(nsad+nsen+1)*2+1,3)
       ;
end

n=(1+nsad+nsen); % Total number of a rod's nodes from saddle top till
   its end
for i=0:n-1
    nodecor(n+(nremain)+i,1)=nodecorpos(i+1,1);
    nodecor(n+(nremain)+i,2)=nodecorpos(i+1,2);
    nodecor(n+(nremain)+i,3)=nodecorpos(i+1,3);
    nodecor(n*3-1+(nremain)+i,1)=nodecorpos(i+1+n,1);
    nodecor(n*3-1+(nremain)+i,2)=nodecorpos(i+1+n,2);
    nodecor(n*3-1+(nremain)+i,3)=nodecorpos(i+1+n,3);
    nodecor(n*5-2+(nremain)+i,1)=nodecorpos(i+1+n*2,1);
    nodecor(n*5-2+(nremain)+i,2)=nodecorpos(i+1+n*2,2);
    nodecor(n*5-2+(nremain)+i,3)=nodecorpos(i+1+n*2,3);
end

n=(nsad+nsen+1)*3;
for i=1:ncab
    nodecor((nremain)+(nsad+nsen)*6+3+i,1)=nodecorpos(n+i,1);
    nodecor((nremain)+(nsad+nsen)*6+3+i,2)=nodecorpos(n+i,2);
    nodecor((nremain)+(nsad+nsen)*6+3+i,3)=nodecorpos(n+i,3);
end

 %% -------Nodal Mass calculation-------
 % Mass calculation as ratios of the lengths
nodemass=zeros(nremain+1+nsen*6+ncab+1,2); % first column is node
   number, second column is the mass ratio from the mass per unit
   length of the rods

nodemass(1,1)=nodecor(1,1);
nodemass(1,2)=(Lfc-Lspr)/(2*ncab);
nodemass(end,1)=nodecor(end,1);
nodemass(end,2)=(Lfc-Lspr)/(2*ncab);
n=nremain+(nsen*2+nsad*2+1)+1;
nodemass(nremain+1,1)=nodecor(n,1);
nodemass(nremain+1,2)=((Lfc-Lspr)/ncab+Lspr/nsen)/2;
n=nremain+1+nsen*6+1;
m=nremain+(nsen*2+nsad*2+1)*2;
nodemass(n,1)=nodecor(m,1);
nodemass(n,2)=((Lfc-Lspr)/ncab+Lspr/nsen)/2;
```

```
n=nremain+1;
for i=1:nsen
    nodemass(n+i,1)=nodecor(n+i,1);
    nodemass(n+i,2)=Lspr/(3*nsen);
    nodemass(n+nsen+i,1)=nodecor(nremain+nsen+nsad*2+i,1);
    nodemass(n+nsen+i,2)=Lspr/(3*nsen);
    nodemass(n+nsen*2+i,1)=nodecor(nremain+(nsen*2+nsad*2+1)+1+i,1);
    nodemass(n+nsen*2+i,2)=Lspr/(3*nsen);
    nodemass(n+nsen*3+i,1)=nodecor(nremain+(nsen*2+nsad*2+1)+(nsen+
       nsad*2)+i,1);
    nodemass(n+nsen*3+i,2)=Lspr/(3*nsen);
    nodemass(n+nsen*4+i,1)=nodecor(nremain+(nsen*2+nsad*2+1)*2+1+i,1);
    nodemass(n+nsen*4+i,2)=Lspr/(3*nsen);
    nodemass(n+nsen*5+i,1)=nodecor(nremain+(nsen*2+nsad*2+1)*2+(nsen+
       nsad*2)+i,1);
    nodemass(n+nsen*5+i,2)=Lspr/(3*nsen);
end

for i=2:nremain
    nodemass(i,1)=nodecor(i,1);
    nodemass(i,2)=(Lfc-Lspr)/ncab;
end

for i=1:ncab-1
    nodemass(end-i,1)=nodecor(end-i,1);
    nodemass(end-i,2)=(Lfc-Lspr)/ncab;
end

%% ------Exporting of Text Files of Parameters------

Nodes = fopen('Nodes.txt','w');
Springs = fopen('Springs.txt','w');
InterWireSprings=fopen('InterWireSprings.txt','w');
EndsFixed = fopen('EndsFixed.txt','w');
EndsHinged = fopen('EndsHinged.txt','w');
Beams = fopen('Beams.txt','w');
BeamPrestress = fopen('BeamPrestress.txt','w');
NodalMass=fopen('NodalMass.txt','w');
NodeLink=fopen('NodeLink.txt','w');

for i=1:nodecor(end,1)
   fprintf(Nodes,'NODE NO %d X %f[m] Y %f[m]\r\n',...
   nodecor(i,1),nodecor(i,2),nodecor(i,3));
```

```
end
%% ------Radial Springs representing the saddle------
%Distributing the springs and their properties on the saddle node
for i=1:(nsad)*2+1
    fprintf(Springs,'SPRI NO %d NA %d DX %f DY %f CP #KONS\r\n',...
    springinc(i,1),springinc(i,1),springinc(i,2),springinc(i,3));
end

%------Shear Springs connecting the rods--------
m=(nremain);%Second to last node of free rod at negative side
mn=(nremain)+(nsen*2+nsad*2+1);%Last Node of bottom wire number
n=(nremain)+(nsen*2+nsad*2+1)*2;%Last Node of mid wire number
for i=2:nsen*2+(nsad)*2
%     fprintf(InterWireSprings,'SPRI NO %d NA %d NE %d CP #KP CT #KT
   MUE #MUE\r\n',...
nodecor(i+mn,1),nodecor(i+m,1),nodecor(i+mn,1));
    fprintf(InterWireSprings,'SPRI NO %d NA %d NE %d CP #KP CT #KT\r\n
       ',...
    nodecor(i+mn,1),nodecor(i+m,1),nodecor(i+mn,1));
end
fprintf(InterWireSprings,'\r\n');
for i=2:nsen*2+(nsad)*2
    fprintf(InterWireSprings,'SPRI NO %d NA %d NE %d CP #KP CT #KT\r\n
       ',...
    nodecor(i+n,1),nodecor(i+mn,1),nodecor(i+n,1));
end
%------Rods Export--------
for i=1:(nremain-1) % Left side (negative) of straight cable
    fprintf(Beams,'BEAM NO %d NA %d NE %d NCS 2\r\n',...
    nodecor(i,1),nodecor(i,1),nodecor(i+1,1));
end
fprintf(Beams,'\r\n');

 % --------Bottom rod--------
n=(nremain); %Second to last node of free rod at negative side
for i=1:(nsen*2+nsad*2)
    fprintf(Beams,'BEAM NO %d NA %d NE %d NCS 1\r\n',...
    (i+n,1),nodecor(i+n,1),nodecor(i+n+1,1));
end
fprintf(Beams,'\r\n');

 % --------Mid Wire at Saddle--------
n=(nremain)+(nsen*2+nsad*2+1);%Last Node of bottom wire number
for i=1:(nsen*2+nsad*2) % Mid Wire at Saddle
```

```
    fprintf(Beams,'BEAM NO %d NA %d NE %d NCS 1\r\n',...
    nodecor(i+n,1),nodecor(i+n,1),nodecor(i+n+1,1));
end
fprintf(Beams,'\r\n');

 % --------Upper Wire at Saddle--------
n=(nremain)+(nsen*2+nsad*2+1)*2;%Last Node of mid wire number
for i=1:(nsen*2+nsad*2)
      fprintf(Beams,'BEAM NO %d NA %d NE %d NCS 1\r\n',...
      nodecor(i+n,1),nodecor(i+n,1),nodecor(i+n+1,1));
end
fprintf(Beams,'\r\n');

n=nremain+(nsen*2+nsad*2+1)+1;
fprintf(Beams,'BEAM NO %d NA %d NE %d NCS 2\r\n',...
nodecor(nremain,1),nodecor(nremain,1),nodecor(n,1));

n=nremain+(nsen*2+nsad*2+1)*2; %Last Node of mid wire number
m=nremain+(nsen*2+nsad*2+1)*3+1;%First Node of free rods
fprintf(Beams,'BEAM NO %d NA %d NE %d NCS 2\r\n',...
nodecor(n,1),nodecor(n,1),nodecor(m,1));
fprintf(Beams,'\r\n');

n=(nremain)+(nsen*2+nsad*2+1)*3;%First Node of free rods
for i=1:(ncab-1) % Right side (Positive) of straight cable
    fprintf(Beams,'BEAM NO %d NA %d NE %d NCS 2\r\n',...
    nodecor(i+n,1),nodecor(i+n,1),nodecor(i+n+1,1));
end

for i=1:length(nodemass(:,1))
    fprintf(NodalMass,'MASS NO %d %f*$(MassUnit)[kg]\r\n',nodemass(i
       ,1),nodemass(i,2));
end

fprintf(EndsFixed,'NODE %d FIX F\r\n',nodecor(1,1));
fprintf(EndsFixed,'NODE %d FIX F',nodecor(end,1));
fprintf(EndsHinged,'NODE %d FIX PP\r\n',nodecor(1,1));
fprintf(EndsHinged,'NODE %d FIX PP',nodecor(end,1));

%% Connecting rods at ends to the rigid link
n=nremain+1; %First Node of bottom wire
m=(nremain)+(nsen*2+nsad*2+1)+1; %First Node of Mid rod number
%Element number (NO) is chosen as the last node's number (arbitrary
   choice)
```

```
fprintf(NodeLink,'BEAM NO %d NA %d NE %d NCS 3\r\n',...
nodecor(end,1)+1,nodecor(n,1),nodecor(m,1));

n=(nremain)+(nsen*2+nsad*2+1)+1; %First Node of Mid rod number
m=(nremain)+(nsen*2+nsad*2+1)*2+1;%First Node of Upper rod number
fprintf(NodeLink,'BEAM NO %d NA %d NE %d NCS 3\r\n',...
nodecor(end,1)+2,nodecor(n,1),nodecor(m,1));

n=nremain+(nsen*2+nsad*2+1); %Last Node of bottom rod number
m=nremain+(nsen*2+nsad*2+1)*2; %Last Node of mid rod number
fprintf(NodeLink,'BEAM NO %d NA %d NE %d NCS 3\r\n',...
nodecor(n,1),nodecor(n,1),nodecor(m,1));

n=nremain+(nsen*2+nsad*2+1)*2;  %Last Node of mid rod number
m=nremain+(nsen*2+nsad*2+1)*3;  %Last Node of upper rod number
fprintf(NodeLink,'BEAM NO %d NA %d NE %d NCS 3\r\n',...
nodecor(m,1),nodecor(n,1),nodecor(m,1));

n=nremain-1;
fprintf(BeamPrestress,'BEAM FROM %d to %d INC 1 TYPE EX $(pre)\r\n',
   ...
nodecor(1,1),nodecor(n,1)); %connecting the free rod to mid wire node

n=nremain;
fprintf(BeamPrestress,'BEAM FROM %d TYPE EX $(pre)\r\n',...
nodecor(n,1));

fprintf(BeamPrestress,'BEAM FROM %d to %d INC 1 TYPE EX $(pre2)\r\n',
   ...
nodecor(n,1),nodecor(end-1,1));

n=nremain+(nsen*2+nsad*2+1)*2;
fprintf(BeamPrestress,'BEAM FROM %d TYPE EX $(pre2)\r\n',...
nodecor(n,1));

fclose(Nodes);
fclose(Springs);
fclose(NodalMass);
fclose(EndsFixed);
fclose(EndsHinged);
fclose(BeamPrestress);
fclose(Beams);
fclose(NodeLink);
fclose(InterWireSprings);
```

Similarly, the text files serve as an input to the SOFiSTik FE solver, which is set as such

```
$ Nonlinear cable analysis - Guido Morgenthal
$ Modified by Tajammal Abbas
$ Costumized by Abdulmagid Bendalla

$ MODEL INPUT PARAMETERS
#DEFINE alpha=35                          $ cable angle [deg]
#DEFINE Emodulus=2e5   $ elastic modulus [N/mm2] (to be calculated for low prestressing)
#DEFINE gamma=0                          $ unit weight [kN/m2]  $78.5
#DEFINE WireDia=100      $ Wire Diameter [mm]
#DEFINE Area=(3.1415*$(WireDia)**2/4) $ in [mm2]
#DEFINE Iy=(3.1415*$(WireDia)**4/64)  $ for each of the three rod in [mm4]
#DEFINE C=0.853  $ Contribution ratio
$ Second moment of area for the rod in [mm^4]
#DEFINE Iy1=(3*$(Iy)+2*$(C)*$(Area)*$(WireDia)**2)
#DEFINE MassUnit=(3*($(Area)*1e-6)*7850) $ Mass per unit length [kg/m]
#DEFINE FT=1770                           $ Sigma_u [N/mm^2]
#DEFINE pre=0.5*$(FT)/$(Emodulus)         $ prestressing strain
#DEFINE pre2=0.5*$(FT)/$(Emodulus)
$ Model properties
#DEFINE LCprimary=1000                   $ Primary load cases (1)
#DEFINE LCeigenvalue=1                   $ Eigenvalue analysis load cases (101,...,901)
#DEFINE NMODE=35

+PROG AQUA urs:1
HEAD MATERIAL AND CROSS SECTIONS
ECHO FULL FULL
$ code
NORM DIN EN1992-2004
$ cable material
STEE NO 1 TYPE Y ES $(Emodulus) GAM $(gamma)  $ FY=1520 FT=1770


$Cross Sectional Values
$#INCLUDE INPUT.txt
SVAL NO 1 MNO 1 A $(Area)[mm2] IY $(Iy)[mm4] $The three rods
SVAL NO 2 MNO 1 A (3*$(Area))[mm2] IY ($(Iy1))[mm4] $the remainder of the cable
SVAL NO 3 MNO 1 A $(Area)[mm2] IY 100*$(Iy1)[mm4] $the rigid link
END

+PROG SOFIMSHA urs:2
HEAD GEOMETRY OF CABLE
SYST 2D GDIV 1000 GDIR NEGY

$ Restraints
$ #INCLUDE EndsFixed.txt           $ CHANGE FIX FOR SENSITIVITY    PP F
#INCLUDE EndsHinged.txt
```

```
LET#KONS=1e20
#INCLUDE Nodes.txt
#INCLUDE Springs.txt
#INCLUDE Beams.txt
#INCLUDE NodeLink.txt
$ Beam, Cable or Truss Elements
#INCLUDE NodalMass.txt
$ shear spring properties
LET#KP=1e10
LET#KT=1e9
LET#FRIC=0.4
#INCLUDE InterWireSprings.txt
END

+PROG SOFILOAD urs:3
HEAD SELF WEIGHT AND PRE-STRESS
LC NO $(LCprimary) DLY -1.0         $ self weight cosideration
#INCLUDE BeamPrestress.txt
END

+PROG ASE urs:12
HEAD NONLINEAR PRIMARY LC ANALYSIS
$CTRL ITER 3 V2 1
CTRL ITER V4 10
$CTRL SPRI 0
CTRL WARN 636
SYST PROB TH3 ITER 10000 FMAX 0.9 TOL -4
LC NO $(LCprimary)
$ECHO FULL EXTR
END

$+PROG ASE urs:4
$HEAD NONLINEAR MODAL ANALYSIS
$SYST PROB TH3 PLC $(LCprimary) ITER 1000 TOL -0.1
$CTRL ITER V4 10
$CTRL WARN 636
$EIGE NEIG $(NMODE) LC $(LCeigenvalue)
$END
```

Bibliography

[1] Guido Morgenthal. *Lecture notes for: Lifelines engineering*. Bauhaus-Universität Weimar, Winter semester 2018.

[2] Mohammed Metwally. Nonlinear numerical analysis of stay cable vibrations. *Bauhaus-Universität Weimar*, 2012.

[3] Holger Svensson. *Cable-stayed bridges: 40 years of experience worldwide*. John Wiley & Sons, 2013.

[4] SOFiSTiK AG. *ASE: General Static Analysis of Finite Element Struc-tures*. SOFiSTiK AG, Oberschleissheim, Germany.

[5] SOFiSTiK AG. *SOFiMSHA: Import and Export of Finite Elements and Beam Structures*. SOFiSTiK AG, Oberschleissheim, Germany.

[6] DANIEL Papini. On shape control of cables under vertical static loads. *M. S. thesis, Lund University, Lund*, 2010.

[7] El Araby El Shenawy. Form finding for cable-stayed and extradosed bridges. 2013.

[8] Konstantinos Kris Mermigas. *Behaviour and design of extradosed bridges*. PhD thesis, 2008.

[9] Guido Morgenthal and Yasutsugu Yamasaki. Behaviour of very long cable-stayed bridges during erection. In *Proceedings of the Institution of Civil Engineers-Bridge Engineering*, volume 163, pages 213–224. Citeseer, 2010.

[10] Elsa Caetano. On the identification of cable force from vibration measurements. In *IABSE-IASS Symposium, London*, 2011.

[11] Guido Morgenthal, Sebastian Rau, Jakob Taraben, and Tajammal Abbas. Determination of stay-cable forces using highly mobile vibration measurement devices. *Journal of Bridge Engineering*, 23(2):04017136, 2017.

[12] A Bellino, L Garibaldi, A Fasana, and S Marchesiello. Tension estimation of cables with different boundary conditions by means of the added mass technique. In *International Conference of Surveilance*, volume 6, pages 25–26, 2011.

[13] Arturo Montoya, Haim Waisman, and Raimondo Betti. A simplified contact-friction methodology for modeling wire breaks in parallel wire strands. *Computers & Structures*, 100:39–53, 2012.

[14] S Kumarasena, NP Jones, P Irwin, and P Taylor. Wind induced vibration of stay cables: Fhwa-hrt-05-083. *Washington, DC: US Department of Transportation, Federal Highway Administration*, 2007.

[15] JH Ernst. Der e-modul von seilen unter berucksichtigung des durchhanges. *Der bauingenieur*, 40(2):52–55, 1965.

[16] James Hopwood Jeans. *Science & music*. Courier Corporation, 1968.

[17] H Max Irvine and Ti K Caughey. The linear theory of free vibrations of a suspended cable. *Proceedings of the Royal Society of London. A. Mathematical and Physical Sciences*, 341(1626):299–315, 1974.

[18] Reseachgate: Czeslaw Kazimierz Szymczak. What is geometrical nonliearity? https://www.researchgate.net/post/What_is_Geomertical_Nonlinearity, 2014. [Online; accessed 8-August-2019].

[19] IABSE Working Commission 3. *Extradosed Bridges, State-of-the-Art Report*. IABSE.

[20] Peter Wolfe. Asymptotic analysis of a rod with small bending stiffness. *Quarterly of applied mathematics*, 49(1):53–65, 1991.

[21] Tatjana Grigorjeva and Zenonas Kamaitis. Numerical analysis of the effects of the bending stiffness of the cable and the mass of structural members on free vibrations of suspension bridges. *Journal of Civil Engineering and Management*, 21(7):948–957, 2015.

[22] Arthur Erich Haas. *Introduction to theoretical physics*, volume 2. Constable Limited, 1925.

[23] Richard Feynman. *The character of physical law*. MIT press, 2017.

[24] Ruina Andy and Pratap Rudra. Introduction to statics and dynamics, e-publishing inc, 2010.

[25] Baby Cristina. Experimental and numerical determination of tension forces of external tendons. *Bauhaus-Universität Weimar*, 2018.

[26] Eduardo AW de Menezes, Rogério J Marczak, and Sandro C Amico. Numerical modeling of helical cables using beam elements. 2018.